ABSTRACT

Title of Document: RAPID LITHOGRAPHY: PHOTOPOLYMERIZATION CHARACTERIZATIONS AND INITIATION KINETICS

Michael Paul Stocker, Doctor of Philosophy, 2012

Directed By: Professor John T. Fourkas
Department of Chemistry and Biochemistry

In order to improve upon the resolution of photolithography, a technique that is used to produce features for today's micro and nanodevices, techniques must move beyond e-beam and deep-UV sources. Multiphoton absorption polymerization (MAP) uses near-infrared light for the creation of complex, three-dimensional features on the sub-100 nm scale. The resolution of MAP can be enhanced further using a two-beam technique called resolution augmentation through photo-induced deactivation (RAPID) to the reach feature sizes as small as 40 nm.

The mechanism and kinetics of photo-induced deactivation are not well understood. To better understand these processes, studies of different photoinitiators have been performed. We find that some photoinitiators are so efficient at deactivation that they are capable of undergoing self-deactivation by addition of another photon from the excitation source. This phenomenon is manifested in a

polymerization trend in which feature size has a proportional velocity (PROVE) dependence, the opposite of the conventional velocity dependence. We also demonstrate that the velocity dependence can also be tuned between PROVE and conventional dependences.

Kinetic models have been formulated to account for the observed deactivation. By reconciling experimental data for some sample photoinitiators with the kinetic model through the use of simulations, kinetic rate constants are determined. The self-deactivation efficiency of each photoinitiator was determined. The lifetimes of intermediates in the radical photopolymerization process were also determined. The kinetic rate constants associated with photoinitiators should allow for the customization of photoinitiators for specific applications and make RAPID a more efficient process capable of reaching resolution on the level of 30 nm and below.

RAPID LITHOGRAPHY: PHOTOPOLYMERIZATION CHARACTERIZATIONS AND INITIATION KINETICS

By

Michael Paul Stocker

Dissertation submitted to the Faculty of the Graduate School of the
University of Maryland, College Park, in partial fulfillment
of the requirements for the degree of
Doctor of Philosophy
2012

Advisory Committee:
Professor John T. Fourkas, Chair
Professor Christopher Davis
Professor Bryan Eichhorn
Professor Sang Bok Lee
Professor YuHuang Wang

Dedication

This work is dedicated my father, James Stocker, and my grandfathers, David Ludington and Harold Stocker, who have been sources of encouragement and inspiration to me to devote my life to exploring God's creation and to being a true man of God.

Acknowledgements

I would like to thank my Lord and Savior, Jesus Christ, through whose strength I needed to get through some of the more difficult periods of getting to this point. It is never easy to have faith in God in a world that seems to take joy in mocking it but He has provided for me in a multitude of blessings I can never repay.

I would also like to thank my wife, Lenea, who has always encouraged me since we met at orientation here our first year (even if she doesn't remember first meeting me). I love that we can have discussions about both chemistry and life while others might roll their eyes and daydream about happier topics. I stand in awe of her talent for teaching and can only hope to be half as good at what I do in the future as she is with conveying the minutia of chemistry to her students.

I thank my family and friends, especially my parents, grandparents and my brothers for always supporting me even when I was playing the prototypical role as middle child. Thanks to my sisters-in-law for being the sisters I didn't have growing up and making my brothers normal… I mean better people.

I feel fortunate to have been able to be under the guidance of Prof. John Fourkas here at the University of Maryland. His constant excitement and encouragement over the research being performed in his group and his breadth of knowledge were always source of inspiration.

I would also like to acknowledge all of the members of the Fourkas group that I had the privilege to work with over the years, especially Dr. Linjie Li, Dr. George Kumi, Dr. Rafael Gattass, and Dr. Farah Dawood.

Dr. Linjie Li was the giant on whose shoulder's I stood as he would probably say about those who came before him. Linjie knew so much about all of the research being preformed. I was fortunate enough to have two years under his tutelage and soak up as much knowledge as I could about MAP and his baby project, RAPID.

Dr. George Kumi and Dr. Rafael Gattass had the answers to everything I could possibly ask. Each helped me a great deal in learning to program in LabVIEW and all things pertaining to optics of which I had no knowledge before joining the group. They were both always good for a laugh when work became stressful.

Dr. Farah Dawood provided me with an ear through which I could bounce off ideas. She graciously agreed to edit my dissertation and she has treated me as a peer while still offering guidance on work and life leading up to and after getting a PhD.

TABLE OF CONTENTS

LIST OF TABLES

LIST OF FIGURES

Chapter 1: Microfabrication and Nanofabrication

1.1 Introduction

The technology that drives today's electronics industry is based to a large extent on the ability to create electronic components that are in the 30 nanometer size regime. This need to miniaturize processors further and to integrate them into smaller areas is a driving force for improving microscopic patterning techniques. The desire for continued progress in miniaturization extends to other realms of nanotechnology as well, including mechanical, chemical and biological sensing for lab-on-a-chip applications. When the device gets smaller, the physical amount of and cost of materials required is lesser. Additionally, by increasing the number of sensors in a device, the number of multiplexed processes can be increased as well, resulting in better resolution and a more thorough analysis of data.

One of the primary tools employed to drive technology into the nanoscale regime is photolithography, a process in which micro and nanofabrication techniques are used to manufacture devices. By selectively exposing regions of a photoresist (i.e., a medium that is chemically or physically susceptible to light), desired features can be realized. These features can be functional themselves, but are also often used as sacrificial layers for further lithographic steps such as material deposition or etching. In light of the current demand for smaller devices, the goal of researchers in the field of lithography is

to pattern the smallest features possible in a photoresist. However, there are four fundamental components of photolithography that need to be addressed in order for new techniques to be viable for the mass production of nano-sized electronic components: feature size, feature complexity, cost-effectiveness, and fabrication time. Therefore, a balance must be struck in order to produce cheaper, faster, and more powerful devices to satisfy consumer needs.

In order to satisfy the current requirement of patterning nanoscale features, many techniques have been developed such as e-beam lithograph and deep UV photolithography. However, these methods require expensive equipment and energy sources that cost millions of dollars.[1] Additionally, the techniques are limited to performing two-dimensional (2D) patterning. Multiple steps are required to make complex three-dimensional (3D) features, increasing the time and the total cost.

As a result of this high cost, more attention has be given to other means of photo-activating a resist, namely in the range of the UV, visible and near-IR regions of the electromagnetic spectrum.[2-7] The energy sources required to produce light in these regions is orders of magnitude less expensive than those required for deep UV. However, each spectra region is limited in resolution. The Abbe criterion states that the resolution, or diffraction limit, R, of light passing through a lens is

$$R = \frac{\lambda}{2n\sin\theta} = \frac{\lambda}{2\mathrm{NA}}, \tag{1.1}$$

where λ is the excitation wavelength, n is the index of refraction of the medium, and θ is the half-angle of the maximum cone of light passing through a lens. If the lens is a microscope objective, commonly used to focus a laser source onto a sample, $n\sin\theta$ is defined by the numerical aperture, NA, of the objective. Equation 1.1 shows that

resolution is directly proportional to the wavelength and inversely proportional to the numerical aperture of the objective. In order to decrease the feature sizes to be comparable to that of high-photon-energy sources, other methods of exciting the photoresist are currently being investigated.

Photoresists typically contain a number of components including photosensitive molecules and susceptible monomers, oligomers, or polymers, depending on the mechanism of the chemistry induced by photoexcitation. Generally, each photosensitive molecule is excited with a single photon to initiate a reaction, resulting in either polymerization or the destruction of polymer bonds. The induced reaction serves to change the solubility of an exposed region, thereby rendering one area more subject to removal in a development step. If the exposed region is the area removed upon development, the photoresist is a positive-tone resist. If the exposed region is the only area remaining after development, the photoresist called negative-tone.

1.2 Multiphoton Absorption Polymerization (MAP)

As a result of the linear nature of single-photon excitation, most single photon photolithographic systems are limited to creating structures in two dimensions. It has been shown that if two or more lower-energy photons are used to excite the photosensitive molecule, photolithography can be extended to the creation of 3D patterns.

1.2.1 Theory of Multiphoton Absorption

The concept of simultaneously absorbing two or more photons (Figure 1.1)was first proposed by Maria Göppert-Mayer in her doctoral thesis in 1931.[8] It was not until

1961, however, that this prediction was realized,[9] with the advent of the laser and the capability to produce the intense source of photons necessary for two-photon excitation. The process is analogous to single-photon absorption (Figure 1.1a), in which a transition occurs from the ground electronic state, S_0, to the first excited electronic state, S_1. With MPA, two or more photons of lower energy are simultaneously absorbed causing the transition (Figures 1.1b-d) from S_0 to S_1 or a higher singlet state. To combine the photons to access the total energy necessary for excitation, a virtual state is involved between the ground and excited states.

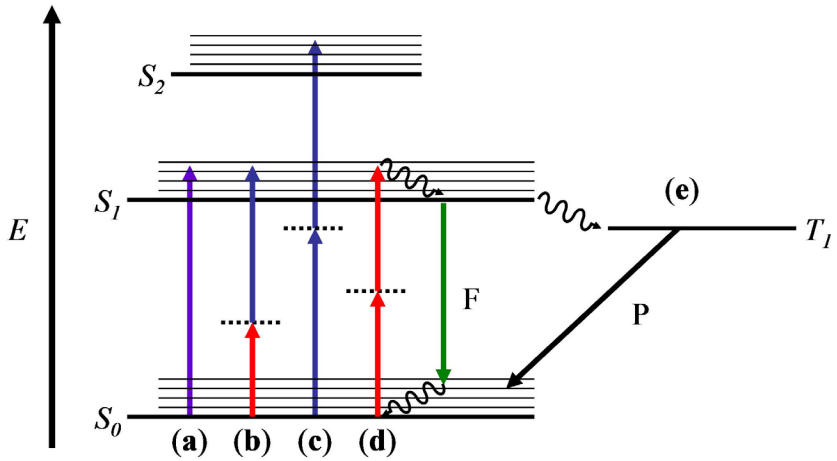

Figure 1.1. Jablonski diagram for (a) single-photon absorption and (a-d) two-photon absorption: (b) non-degenerate; (c) degenerate excitation to S_2, (d) degenerate excitation to S_1. Dotted lines represents virtual states for two-photon absorption. Upon excitation, molecules can fluoresce, F, or undergo intersystem crossing to the triplet state, T_1. In the triplet state, phosphorescence, P, can lead back to the ground state, S_0. Radical production for multiphoton absorption polymerization (MAP) occurs in the triplet state (e).

There are both non-degenerate and degenerate pathways for MPA. Non-degenerate MPA occurs when two different wavelength of light are combined (Figure 1.1b). When the excitation source is the combination of two photons of equal energy, the process is termed degenerate two-photon absorption (TPA). Degenerate TPA is the most

common implementation of MPA. The two photons can either excite to the first excited state (Figure 1.1d) or to a higher excited state (Figure 1.1c).

For TPA, the probability of absorption scales proportionally with the square of the source intensity. In order to improve the probability of TPA without requiring a large intensity of continuous-wave (CW) laser power, pulsed lasers have been employed as they deliver dense packets of energy in pulses with durations on the femtosecond to picosecond timescale. Additionally, when passed through a high-*NA* objective, the laser beam can be focused to a tight focal region, as shown by the fluorescence of a rhodamine solution in Figure 1.2. The transverse integral of the intensity squared shows that the region of highest intensity is located in the focal volume for MPA, unlike the uniform transverse integrated intensity of a single-photon source focused through a medium. As a result, with the correct laser intensity, TPA can occur only in the focal region of the laser beam. The active 3D volume within that focal region of MPA is termed a voxel.

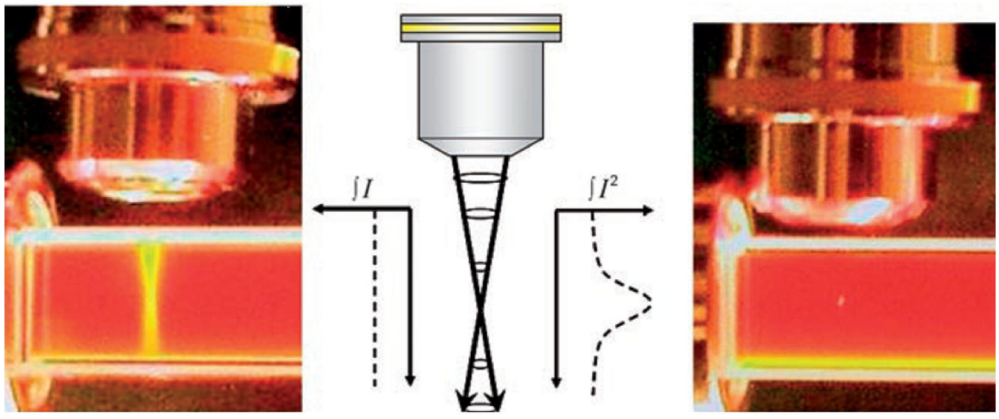

Figure 1.2. Fluorescence from a solution of Rhodamine B. Excitation from a single-photon source (left) results in fluorescence throughout the exposure area with an equal intensity distribution. Two-photon excitation (right) results in only a small volume of fluorescence at the focal region. The excitation is located mostly in the focal region (evident by the integrated intensity profile) because of the non-linear optical process. (Adapted from ref 4.)

The primary application of MPA, and one that predates MAP, is in fluorescence microscopy. In this application, the voxel is used to excite small areas within a fluorescent material. After absorption, vibrational relaxation occurs, followed by fluorescence. The sample is moved in two or three dimensions relative to the focal region, resulting in a high-resolution image. Another advantage of MPA is its ability to penetrate into materials. Much like exciting only a small region in the center of a rhodamine solution (Figure 1.2), a scan of the laser beam can produce a 2D fluorescence image. Successive scans in a fluorescent sample of different penetration depths with MPA can result in a 3D image[10] (Figure 1.3).

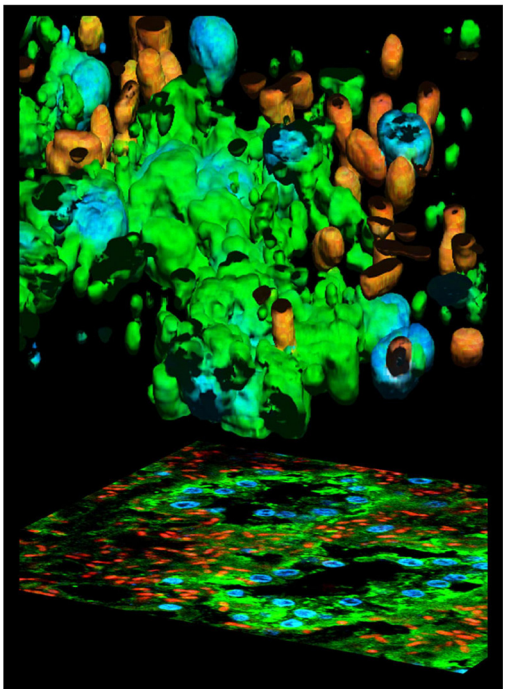

Figure 1.3. 3D and 2D fluorescence projections of a marine sponge, *Chondrilla nucula*, obtained from sequential two-photon fluorescence scans pentetrating sample (adapted from ref 10).

MAP and multiphoton fluorescence microscopy are similar in that vibrational relaxation is followed by either initiation of polymerization or emission of fluorescence. In the case of radical MAP, this mechanism involves intersystem crossing to the triplet

state (Figure 1.1e) inducing radical polymerization. In MAP, photopolymerization is localized to the focal region, with a short exposure yielding a physical voxel of polymerized material. The source can also penetrate the surface of the photoresist while still maintaining localized excitation. Moving the photoresist relative to the focal region (or vice versa) allows for the polymerization, or fabrication, of arbitrary, 3D structures.

1.2.2 Mechanisms of MAP

There are two widely-used polymerization mechanisms for MAP: cationic and radical. Cationic polymerization utilizes the formation of a strong Brønsted acid upon absorption of a photon by a photoacid generator (PAG). In the presence of epoxides or vinyl ether monomers, the PAG acts as a catalyst for crosslinking.[11] The advantages of using cationic polymerization are evident in the applications of the epoxide-based photoresist SU-8 (Figure 1.4a). SU-8 is a negative-tone photoresist that typically incorporates triphenylsulfonium salt (Figure 1.4b) as the PAG. Each SU-8 monomer has eight epoxide groups capable of crosslinking. Due to its high viscosity, SU-8 can be used for the formation of very complex 3D structures using multiphoton absorption. The high viscosity of SU-8 also allows for the creation of structures with very high aspect ratios (> 50:1). The resolution of MAP, along with the freedom to fabricate high-aspect-ratio structures makes SU-8 an attractive photoresist. The most common applications for SU-8 in MAP are the fabrication of complex microfluidic channels[12-14] and photonic devices, [15-18] as shown in Figures 1.4c-e. Some of the disadvantages associated with fabrication in SU-8 are the long time periods and large amounts of material required for fabrication and

processing. In addition, numerous processing steps are required, including spin coating the resist onto the substrate, multiple baking steps, and solvent development.

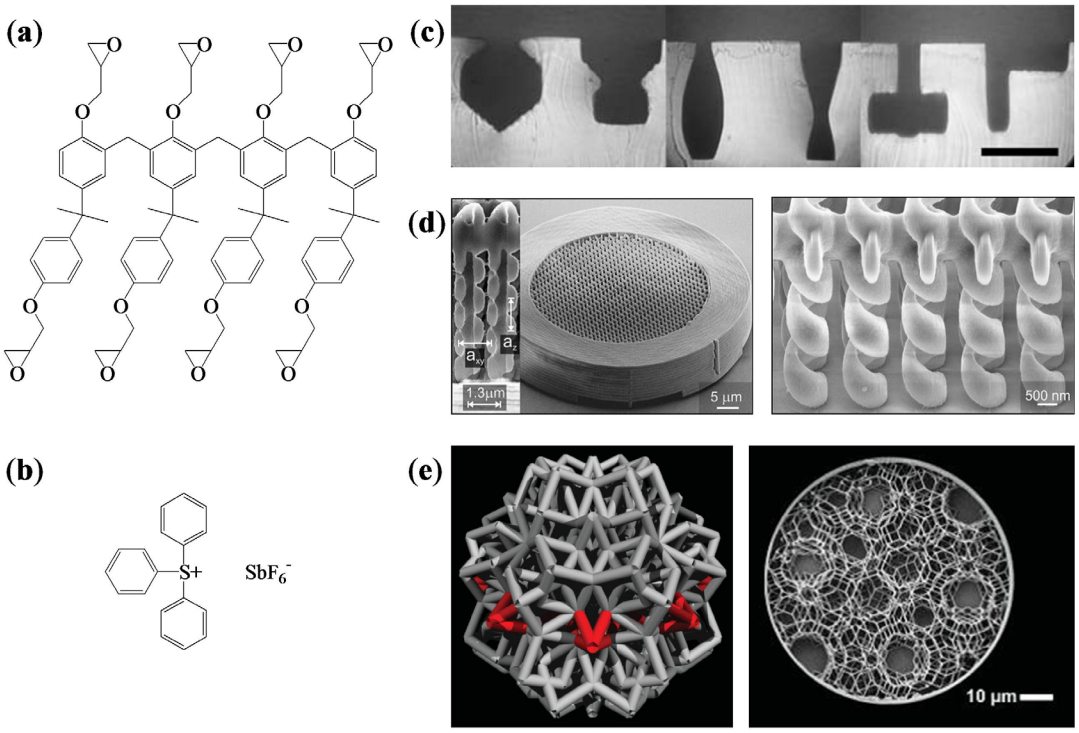

Figure 1.4. SU-8 is an epoxy-based monomer (a) used in cationic polymerization. A common photoacid generator is triphenylsulfonium hexafluoroantimonate (b). Using SU-8 and MAP allows for the fabrication of structures such as complex microfluidic channels (c, optical image of cross-section with scale bar of 100 μm; adapted from ref 13) molded from an SU-8 master structure (c) and complex photonic devices such as spiral photonic crystals (d, SEM images of device; adapted from ref 18) and rhombicuboctahedral photonic quasicrystals (e; left, model of eight-fold symmetry; right, SEM image of eight-fold symmetric quasicrystal; adapted from ref 16).

The other, and more common polymerization mechanism commonly employed in MAP is radical polymerization, as shown here schematically[7,11]:

Initiation

$$PI \xrightarrow{h\nu} PI^{*} \longrightarrow R\bullet \qquad (1.3a)$$

$$PS \xrightarrow{h\nu} PS^{*} \xrightarrow{I} I^{*} \longrightarrow R\bullet \qquad (1.3b)$$

Propagation

$$R\bullet + M \longrightarrow RM\bullet \xrightarrow{M} RMM\bullet \ldots \longrightarrow RM_{n}\bullet \qquad (1.4)$$

Inhibition

$$RM_{n}\bullet + Z \longrightarrow RM_{n} + Z\bullet \qquad (1.5a)$$

$$RM_{n}\bullet + Z \longrightarrow RM_{n}Z\bullet \qquad (1.5b)$$

Termination

$$RM_n\bullet + RM_m\bullet \longrightarrow RM_{m+n}R \quad (1.6a)$$

$$RM_n\bullet + RM_m\bullet \longrightarrow RM_n + RM_m \quad (1.6b)$$

In most applications, the excitation of the photosensitive molecule, called a photoinitiator, *PI*, directly produces a radical, *R*• (Eq. 1.3a). In some applications, however, the photosensitive molecule, *PS*, can become excited and transfer that energy to a coinitiator, *I*, which in turn forms a radical (Eq. 1.3b). The coinitiator is not normally photoactive at the excitation wavelength.

With the production of radicals, a chain reaction is initiated (Eq. 1.4) in a solution of monomers and/or oligomers, *M*, many of which have multiple active sites capable of crosslinking. Polymerization continues until terminated by the cross-reaction of propagating radicals (Eqs. 1.6). Additionally, a radical inhibitor, *Z*, can be added to the photoresist to reduce the number of propagation steps. The inhibitor can terminate the chain reaction by consuming the radical without producing another radical capable of continuing polymerization (Eqs. 1.5). These processes occur until all the inhibitor molecules.[11] The multiple steps involved in the radical polymerization process make it a viable option for customizing the photoresist towards specific applications.

The final step in MAP is the development of the sample in solvent rinses. Most MAP resists are negative-tone, i.e. the crosslinking of the monomers reduces their solubility. When exposed to solvent during the development step, the remaining uncrosslinked monomers are washed away leaving only the free standing polymerized structures. This situation is in contrast to a positive-tone photoresist where the areas that are exposed are washed away during development. This method is typically the reverse mechanism of polymerization, i.e. the absorption of light causes polymer bonds to break

making those areas more soluble during development. An example of a positive-tone photoresist is poly(methyl methacrylate) (PMMA; Figure 1.5).

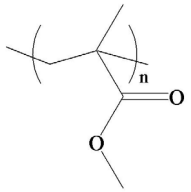

Figure 1.5. Structure of poly(methyl methacrylate) (PMMA), a commonly used positive-tone photoresist.

In order for radical polymerization to be initiated with MPA, it is assumed that a threshold concentration of radicals must be reached. Satisfying this condition requires a high enough intensity from the excitation source or a high enough concentration of photoinitiator. As a result, the radical threshold can limit the efficiency of photoactivation.

Even though MAP is capable of fabricating complex 3D structures, its limitations are most often the feature resolution and the fabrication time. MAP is a serial process by which the laser focal region must be moved relative to the photoresist (or vice versa); therefore, the required time for the overall process can be long due to the increased freedom of movement.

1.2.3 Measuring Feature Sizes

As with any lithographic technique, the measurement of feature size is an integral part of the entire process. There are numerous methods for fabricating photopolymerized structures in which the feature size can be measured. The main goal is to isolate a feature within a certain volume for measurement. Because feature size is dependent upon

exposure conditions as well as the environment, fabrication techniques that can deliver reproducible results are desired.

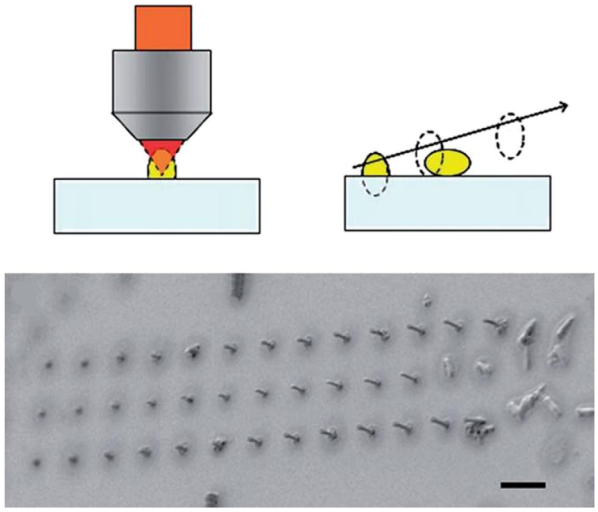

Figure 1.6. Ascending scan (or voxel study) method for determining feature size. Short exposures with the focal region of the laser are performed at increasing depths within the bulk (z-direction) photoresist until voxels fall over. In this manner, the height (axial dimension) and width (transverse dimension) are revealed using SEM. The scale bar for the SEM image is 10 μm. (Adapted from ref 4.)

The most commonly employed method for measuring feature size in MAP is the ascending scan method or voxel study[4,7] depicted in Figure 1.6. In this method, a single voxel is formed within the photoresist by a brief exposure to the laser beam. Voxels are then reproduced under the same exposure conditions at varying depths within the photoresist relative to the substrate. As the depth into the photoresist is increased, the voxel is held in position by its attachment to the functionalized substrate. At a given depth within the photoresist, the aspect ratio of the voxel becomes too large while being weakly attached to the substrate. As a result, the voxel falls over onto the substrate revealing both its axial dimension and the transverse dimension. If a voxel is formed too deep into the photoresist, it floats away upon sample development as it is not tethered to the substrate. The change in voxel morphology due to the variation of exposure

conditions is usually the impetus for a voxel study. When studying the effects of exposure duration, the typical trend observed is that the feature size decreases at shorter exposure times. This trend generally holds true until the formation of sufficient radicals can no longer take place.

Another technique for measuring feature size is through the fabrication of solid lines. This method can be implemented in numerous ways. The most straightforward method is to fabricate lines directly onto the substrate, as shown in Figure 1.7a. This implementation, however, limits measurements to the transverse dimension and still suffers from the asymmetry of feature size relative to depth. A technique that can overcome these shortcomings is the suspended bridge method[7] shown in Figures 1.7b-h. Here, support structures are created in the photoresist, followed by perpendicular lines across the supports. The perpendicular line is not attached to the surface so relative measurements of the axial dimension can be made by tilting the sample during the imaging process. The downside to this method is the potentially long fabrication times of support structures and the determination of appropriate spacing for the supports. Since the fabricated structure consists of a soft polymeric material, features can be subject to sagging and other distortions that can result in inaccurate measurements.

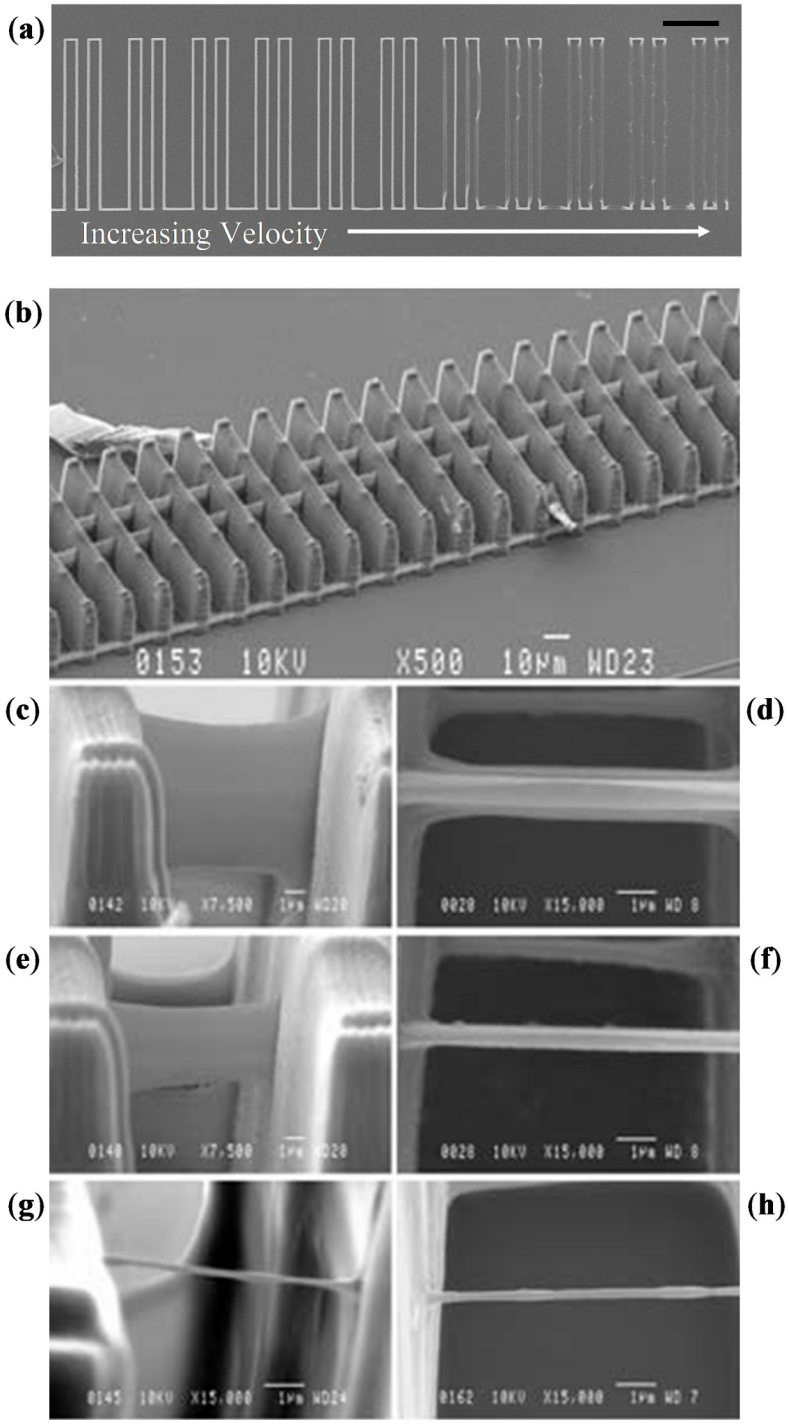

Figure 1.7. Direct fabrication of lines on a substrate (a). The scale bar is 10 µm. The suspended bridge method for determining feature sizes of lines is depicted in b-h. Tilted view of the top of the structure (c). Side view (c,e,g) and each respective top view (d,f,h) images of lines fabricated with different parameters. The lines in (c,d) and (e,f) were fabricated at the same exposure intensity but higher velocity, respectively. The lines in (e,f) and (g,h) were fabricated at the same velocity but decreasing exposure intensity, respectively. (b-h adapted from ref 7.)

1.2.4 Applications of MAP

Many studies that involve radical polymerization with MPA use photoresists that contain acrylic monomers. Here, a radical homolytically cleaves the double bond on the acrylate terminal group. Multiple acrylate groups on a single monomer allow for efficient crosslinking. Uses for acrylic microstructures include waveguides[4,19] (Figures 1.8a,b) and cantilevers[4,20] (Figure 1.8c). Acrylic microstructures fabricated via MAP have been utilized in biology, e.g. in the creation of microfeatures upon which cells can move and interact for the purpose of controlling their directionality[21-23] (Figure 1.8d). Acrylic microstructures have also been used as tissue scaffolds.[24,25]

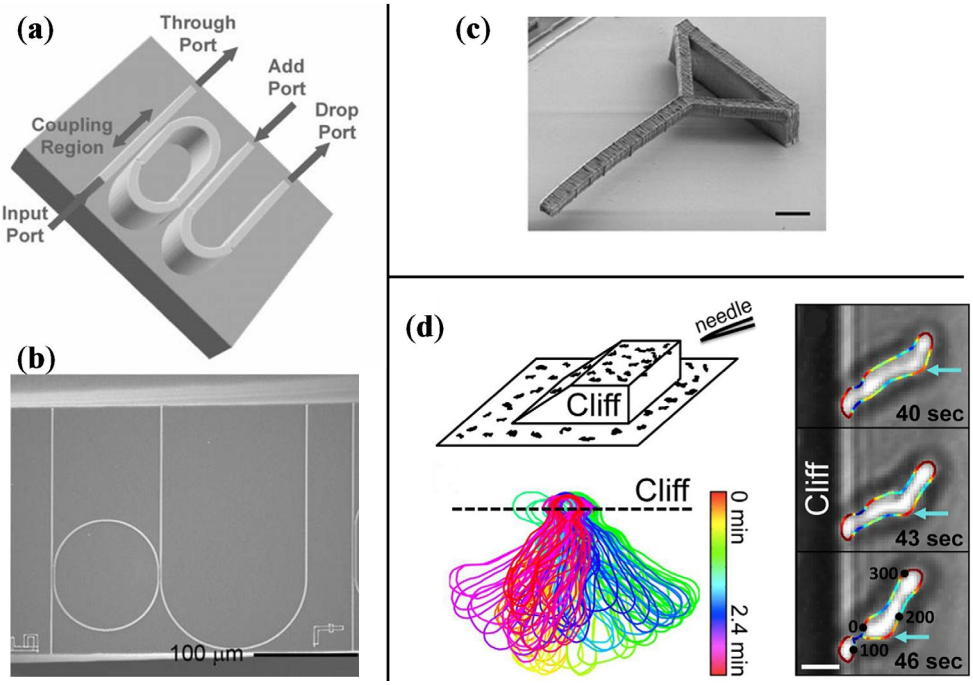

Figure 1.8. Examples of applications of MAP. A microring resonator, a waveguiding structure, shown schematically in (a) and in the SEM (b) couples light from the input port to the drop port (adapted from ref 19); An SEM image of cantilever is shown with a scale bar of 10 µm (c; adapted from ref 4). A ramp and cliff structure (d) is used to observe how the amoeba, *Dictyostelium discoideum*, interacts with its environment (adapted from ref 21).

Since the majority of work in MAP has been limited to neat photoresists or photoresists with an organic solvent, direct applications of MAP as final devices have been fairly limited. Therefore, much attention has been paid to applying MAP toward photo-crosslinking other materials especially more biocompatible (i.e., non-toxic) materials capable of use with animal cells. Proteins such as bovine serum albumin[26-29] (BSA) and collagen[30] are the most commonly used biomolecules along with fibrinogen,[28] biotinylated BSA,[29] and avidin.[29] Shear *et al.* have used BSA with methylene blue (Figure 1.9a) to create "lobster traps" for isolating bacteria (Figure 1.10).[26] Hybrid gelatin-acrylate materials have also been employed for culturing cells.[31] Other biocompatible photosensitizers include rose bengal[28,32] (Figure 1.9b) and flavin adenine dinucleotide (FAD; Figure 1.9c)[33] and have been used to crosslink BSA and collagen using MPA.

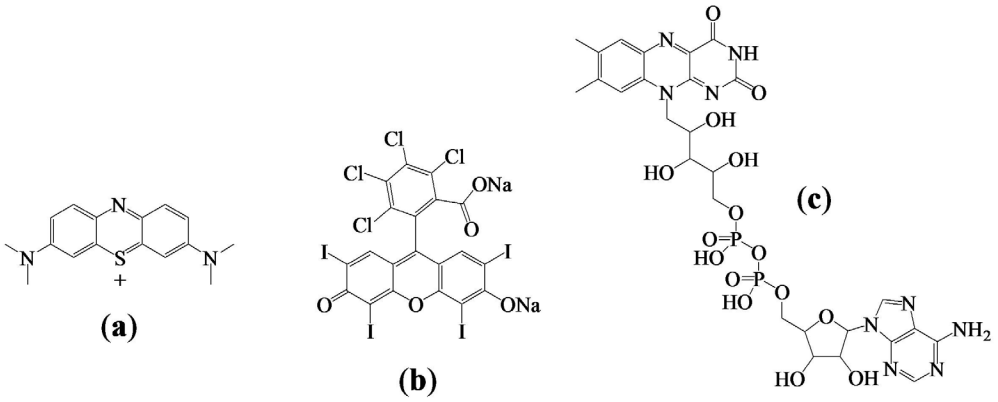

Figure 1.9. Biocompatible photoinitiators used with MAP of proteins: (a) methylene blue, (b) rose bengal, and (c) flavin adenine dinucleotide.

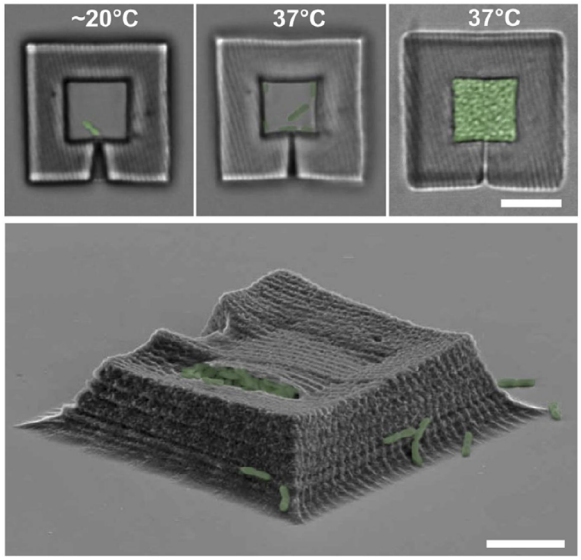

Figure 1.10. "Lobster" trap for monitoring bacteria growth. The top differential interference contrast (DIC) images (scale bar equals 10 µm) illustrate how heating device from 20 °C to 37 °C closes the entrance, trapping a single bacterium allowing it to produce a colony. The bottom SEM image shows a 3D view of the trap with a scale bar of 5 µm. Bacteria are shown in green (false color). (Adapted from ref 26.)

The surfaces of acrylic microstructures fabricated via MAP can also be altered by using a variety of surface chemistry techniques, thus leading to surface functionalization. For example, surfaces can be modified to have terminal amines that can be used for biological applications[34] (Figure 1.11, bottom) or as the foundation for further functionalization. Further functionalization can be achieved by applying Michael addition to any unreacted acrylate groups on the surface of polymerized microstructures. Also, if a methacrylate resin is used for polymerization, the presence of the methyl group inhibits amination, allowing for the possibility of selective functionalization of acrylic polymers in a microstructure containing both acrylic and methacrylic polymers.

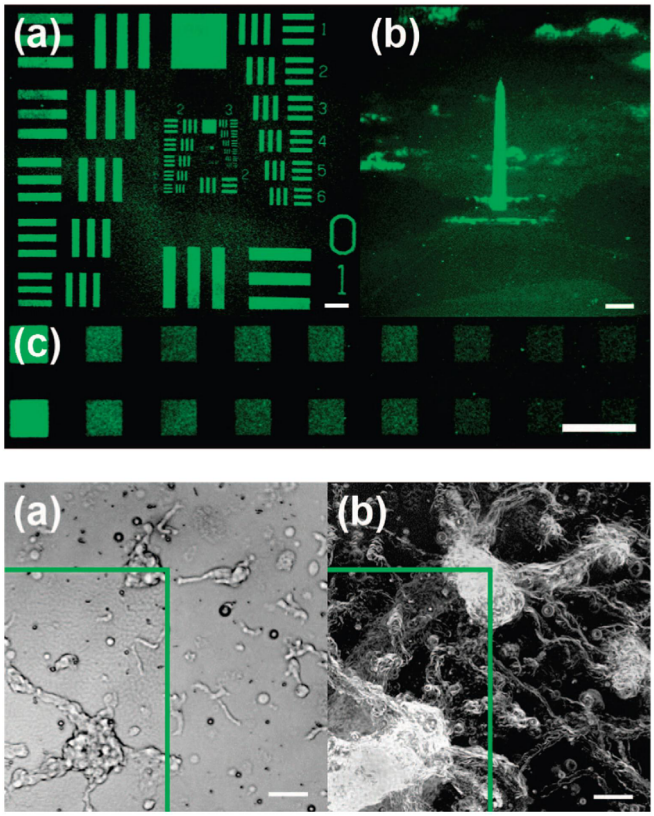

Figure 1.11. Amine-functionalized polymer areas. The top images (a-c) show dansyl chloride attached to the amine groups leading to increased fluorescence of the polymerized areas. The intensity of fluorescence is dependent upon the degree of crosslinking, as shown using a gray-scale mask (top, c). The scale bars for the top images are 1 mm. The bottom panel shows time-lapse images (a, midway through cell aggregation; b, time-averaged) of cells aggregating to surfaces coated with amines. The areas bounded by the green lines are of higher amine density at the surface. The scale bar for the bottom images are 50 µm. (Adapted from ref 34.)

The presence of the amines on the surface of polymerized microstructures allows for further functionalization such as treating the structure with dansyl chloride, which in turn renders the functionalized area fluorescent[34] (Figure 1.11, top). Microstructures and nanostructures that are fabricated using a photolithography step are primarily employed as circuit components, and therefore it would be advantageous to metallize them, especially in a selective manner. It has been shown[4,35] that a palladium-catalyzed electroless-deposition method can be applied to deposit copper on an amine

functionalized acrylate surface (Figure 1.12). Silver can also be deposited using $SnCl_2$ as a catalyst.[36,37]

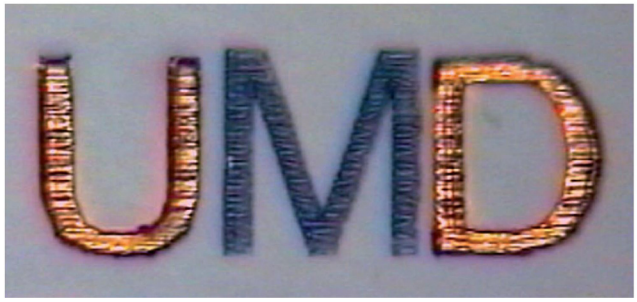

Figure 1.12. Selective functionalization with copper using acrylic and methacrylic polymers. The "U" and "D" were fabricated using an acrylic resin while the "M" was fabricated using a methacrylic resin. Only the acrylic resin structures could be functionalized with amines, the prerequisite to electroless deposition of copper. (Adapted from ref 4.)

Microstructures fabricated using MAP are also widely used as master structures for molding microfluidic channels. Molding allows for the 3D structures to be reproduced as a negative for structure replication. The most commonly used polymer for molding is polydimethylsiloxane (PDMS; Figure 1.13), because of its relative inertness to most solvents[38] and biological media. The molds are filled with photoresist and adhered to a substrate. Because of the transparency of PDMS, the photoresist can be exposed and polymerized with a single-photon process. The mold can then be removed and reused to create multiple copies of the same master structure fabricated via MAP.

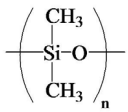

Figure 1.13. Polydimethylsiloxane (PDMS) is a commonly used polymer for creating microfluidic channels and molds based on MAP master structures.

For microfluidics, the fabricated 3D channels can be imbedded within PDMS or at the surface. More complex 3D structures require the use of a novel membrane

method[4,39,40] to create closed-loop structures, as depicted in Figure 1.14. After removal from the master, the thin PDMS walls molded from the membrane can be bonded together. The PDMS can then be bonded to a substrate such as glass or silicon for a completed device.

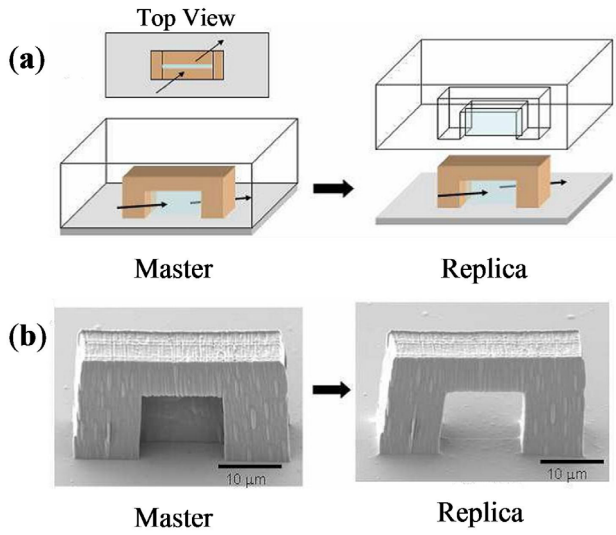

Figure 1.14. Molding of closed-loop structures shown schematically (a) and in SEM images (b). A membrane is fabricated on the master (left) created with MAP. Molding with PDMS and producing a replica results in structure having a closed loop. (Adapted from ref 39.)

1.3 Resolution Augmentation through Photo-Induced Deactivation (RAPID)

It would be highly advantageous if the UV, visible and near-IR regions of the electromagnetic spectrum could achieve features smaller than those theoretically allowed by the Abbe criterion (Eq. 1.1). In order to overcome the limitations of conventional approaches to photolithography, novel methods are required to change the chemistry and/or photophysics involved in the interaction of light with the photoresist.[41] Scott *et al.* incorporated a two-beam method[6] in which the photoinitiator could be excited with one beam at 473 nm to initiate single-photon polymerization. They employed a second beam

at 364 nm that could activate a photosensitive molecule that inhibits the photoinitiator from inducing polymerization. Selective positioning of the inhibition source relative to the polymerization initiation source reduced the feature sizes to a minimum of 64 nm full-width at half maximum (FWHM) or a value of ~λ/7.3 (where λ is the wavelength of the excitation source).

Andrew *et al.* used a related two-beam technique[2] along with a novel chemical switch. The photoresist was activated by a single photon process with a 325 nm laser source. A film of photochromic molecules was placed on top of the photoresist. When a 633 nm source was applied to the film, the film became opaque to the 325 nm polymerization source. Again, by selectively positioning the 633 nm source relative to the 325 nm source, the effective area of exposure was limited to a small spot. With this method, features as small as 36 nm were polymerized, a resolution of ~λ/9.

The realization of smaller feature sizes using MAP came in the form of resolution augmentation through photo-induced deactivation (RAPID),[5] the inspiration for which came from stimulated emission depletion (STED) microscopy, a technique used to augment resolution in fluorescence microscopy.[42-45] In STED, photoexcitation takes place from the ground state to the first excited state followed by vibrational relaxation. At some point between vibrational relaxation and the radiative process of fluorescence emission, stimulated emission to the ground state is induced with the addition of a second, pulsed laser source at a longer wavelength. The result is a reduced population undergoing fluorescence emission. The active fluorescent area of analysis is correspondingly reduced. Overlapping of the beams either axially or in the transverse

dimension results in sub-diffraction limited microscopy with resolution unobtainable by optics alone.

STED was thought to be applicable to MAP in that the concept of preventing intersystem crossing would result in the formation of fewer radicals. With a threshold radical concentration required to initiate polymerization, depletion of only a relatively small population of excited molecules could completely turn off polymerization. In the first application of STED to MAP, a pulsed 800 nm beam was used to induce two-photon absorption and a second pulsed 800 nm laser was synchronized to apply a STED beam. Because most radical initiators undergo intersystem crossing after ~100 ps,[46] the pulses for the STED beam were stretched to ~50 ps[47] to allow for vibrational relaxation to occur.

A key requirement in STED is that the molecule could not absorb the additional photon to get excited to an even higher excited state. Intersystem crossing occurs at a faster rate from higher excited states, making polymerization more efficient. Typical radical photoinitiators have smaller oscillator strengths between the ground and first excited states than the fluorescent molecules used in STED and so are not suitable for this application. To satisfy the requirements of STED, additional photoinitiating radical producers were sought that had a high oscillator strength between the ground and first excited states.[48] Additionally, a molecule with a low fluorescence quantum yield was sought based on the idea that a non-radiative process might lead to radical formation instead of fluorescence.

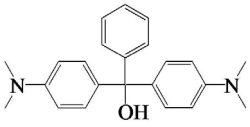

Figure 1.15. The photoinitiator used in the first RAPID studies, malachite green carbinol base (MGCB).

It was discovered that malachite green carbinol base (MGCB; Figure 1.15) could act as photoinitiator that was capable of photoinduced inhibition of polymerization (Figure 1.16). To ensure that STED was, in fact, the cause for the inhibition, the timing between pulses of initiation (200 fs) and depletion (50 ps) was varied. It was found that for delays as long as 13 ns (longer than a reasonable fluorescence lifetime), the efficiency of depletion did not change (Figure 1.16, bottom left). This observation implies that an unknown intermediate species is capable of deactivation upon addition of another photon. Thus, a mechanism other that stimulated emission is responsible for deactivation. As a result, the process was termed "resolution augmentation through photo-induced deactivation," or RAPID lithography.

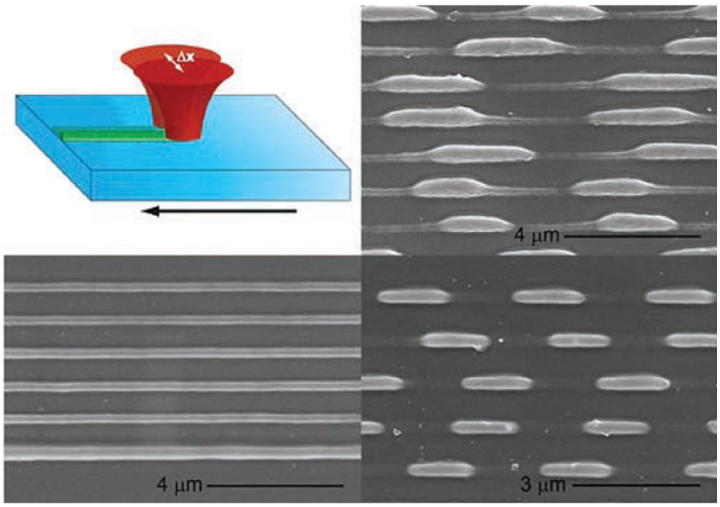

Figure 1.16. Schematic diagram (top, left) of overlapping excitation and deactivation beams used in RAPID. If the beams are directly overlapping (top, right) using a 50-ps pulsed deactivation beam, fabrication can be partially inhibited. Changing the delay between the pulses of the excitation beam (200 fs) and the deactivation beam has no affect of feature size (bottom, left). The bottom-most line has no deactivation applied, the lines above it having varying delay times. These data illustrate that stimulated emission depletion is not the mechanism involved with RAPID. Changing the deactivation beam to continuous wave (CW) still causes an inhibition of polymerization (bottom, right). (Adapted from ref 5.)

Based upon the observations that the delay time between pulses did not affect deactivation, a continuous-wave (CW) deactivation beam was tested and it was found

that deactivation still occurred (Figure 1.16 bottom right). This result indicated that synchronized beams were not necessary and that a less expensive CW deactivation source could be employed. This discovery also opened up the possibility of carrying out RAPID using single-photon processes. A CW source could be used for single-photon photoinitiation, while a second, longer wavelength, CW source could deactivate the molecules.

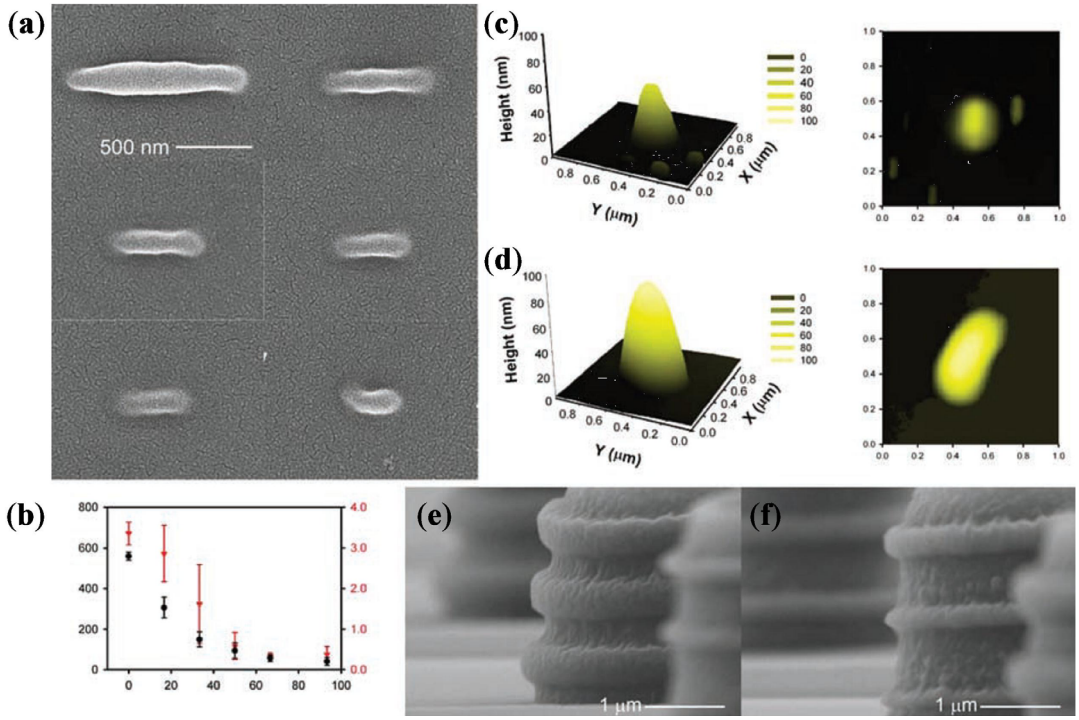

Figure 1.17. The axial feature size scale inversely with the deactivation intensity in RAPID, as seen in SEM images (a) and graphically (b). The smallest axial feature possible with RAPID was 40 nm as measured by AFM (c). Without deactivation, the minimum axial feature size was 80 nm (d). Fabricating towers with RAPID (f) illustrates the axial resolution enhancement over conventional MAP (e). (Adapted from ref 5.)

After close refinement of the optical design, a voxel study revealed that features as small as 40 nm in the axial dimension and 80 nm in the transverse dimension (an aspect ratio of 0.5) could be obtained using RAPID (Figure 1.17c). This result translates to a maximum value of $\lambda/20$ and the highest resolution yet seen for an 800 nm source.

Feature sizes were also found to be relatively tunable, depending upon the intensity of the deactivation beam (Figures 1.17a,b). Other methods employing similar, two beam systems, as described previously have both used shorter wavelengths and more complicated resist setups[2] or photoresist mixtures[6] to achieve comparable feature sizes.

1.4 Thesis Outline

The motivation for the work presented here is the further development of RAPID to reach higher resolutions with an 800 nm source. The results discussed here are aimed at advancing the search for maximum resolution augmentation. Through a better understanding of the mechanism of deactivation as well as the associated efficiency of the molecule undergoing deactivation, higher resolution can be achieved. The focus of the work presented (described by methods in Chapter 2) is on deactivation, including the realization of a class of photoinitiators that can undergo self-deactivation (Chapter 3). This concept, combined with the ability to induce deactivation using RAPID, are then used to develop a refined kinetic model for the mechanism of deactivation that is reconciled with experimental measurements (Chapter 4). A brief overview of results for a single-photon RAPID process will be discussed (Chapter 5) and finally concluding remarks as well as future work will be discussed in Chapter 6.

References:

(1) Senturia, S. D., *Microsystem Design*. Kluwer Academic Publishers: 2001.

(2) Andrew, T. L.; Tsai, H.-Y.; Menon, R., Confining Light to Deep Subwavelength Dimensions to Enable Optical Nanopatterning. *Science* **2009,** 324, (5929), 917-921.

(3) Fourkas, J. T., Nanoscale Photolithography with Visible Light. *Journal of Physical Chemistry Letters* **2010,** 1, (8), 1221-1227.

(4) LaFratta, C. N.; Fourkas, J. T.; Baldacchini, T.; Farrer, R. A., Multiphoton fabrication. *Angewandte Chemie-International Edition* **2007,** 46, (33), 6238-6258.

(5) Li, L.; Gattass, R. R.; Gershgoren, E.; Hwang, H.; Fourkas, J. T., Achieving lambda/20 Resolution by One-Color Initiation and Deactivation of Polymerization. *Science* **2009,** 324, (5929), 910-913.

(6) Scott, T. F.; Kowalski, B. A.; Sullivan, A. C.; Bowman, C. N.; McLeod, R. R., Two-Color Single-Photon Photoinitiation and Photoinhibition for Subdiffraction Photolithography. *Science* **2009,** 324, (5929), 913-917.

(7) Sun, H.-B.; Kawata, S., Two-Photon Photopolymerization and 3D Lithographic Microfabrication. *Advances in Polymer Science* **2004,** 170, 169-273.

(8) Göppert-Mayer, M., Über Elementarakte mit zwei Quantensprüngen. *Annalen der Physik* **1931,** 401, (3), 273-294.

(9) Kaiser, W.; Garrett, C. G. B., Two-Photon Excitation in CaF_2:Eu^{2+}. *Physical Review Letters* **1961,** 7, (6), 229-231.

(10) Diaspro, A.; Bianchini, P.; Vicidomini, G.; Faretta, M.; Ramoino, P.; Usai, C., Multi-photon excitation microscopy. *BioMedical Engineering OnLine* **2006,** 5, 36-1-14.

(11) Odian, G. G., *Principles of polymerization*. Wiley: 1991.

(12) Kuebler, S. M.; Braun, K. L.; Zhou, W. H.; Cammack, J. K.; Yu, T. Y.; Ober, C. K.; Marder, S. R.; Perry, J. W., Design and application of high-sensitivity two-photon initiators for three-dimensional microfabrication. *Journal of Photochemistry and Photobiology A - Chemistry* **2003,** 158, (2-3), 163-170.

(13) Kumi, G.; Yanez, C. O.; Belfield, K. D.; Fourkas, J. T., High-speed multiphoton absorption polymerization: fabrication of microfluidic channels with arbitrary cross-sections and high aspect ratios. *Lab on a Chip* **2010,** 10, (8), 1057-1060.

(14) Zhou, W. H.; Kuebler, S. M.; Braun, K. L.; Yu, T. Y.; Cammack, J. K.; Ober, C. K.; Perry, J. W.; Marder, S. R., An efficient two-photon-generated photoacid applied to positive-tone 3D microfabrication. *Science* **2002,** 296, (5570), 1106-1109.

(15) von Freymann, G.; Ledermann, A.; Thiel, M.; Staude, I.; Essig, S.; Busch, K.; Wegener, M., Three-Dimensional Nanostructures for Photonics. *Advanced Functional Materials* **2010,** 20, (7), 1038-1052.

(16) Ledermann, A.; Wegener, M.; von Freymann, G., Rhombicuboctahedral Three-Dimensional Photonic Quasicrystals. *Advanced Materials* **2010,** 22, (21), 2363-2366.

(17) Soukoulis, C. M.; Wegener, M., Past achievements and future challenges in the development of three-dimensional photonic metamaterials. *Nature Photonics* **2011,** 5, (9), 523-530.

(18) Thiel, M.; Decker, M.; Deubel, M.; Wegener, M.; Linden, S.; von Freymann, G., Polarization stop bands in chiral polymeric three-dimensional photonic crystals. *Advanced Materials* **2007,** 19, (2), 207-210.

(19) Li, L.; Gershgoren, E.; Kumi, G.; Chen, W. Y.; Ho, P. T.; Herman, W. N.; Fourkas, J. T., High-Performance Microring Resonators Fabricated with Multiphoton Absorption Polymerization. *Advanced Materials* **2008,** 20, (19), 3668-3671.

(20) Bayindir, Z.; Sun, Y.; Naughton, M. J.; LaFratta, C. N.; Baldacchini, T.; Fourkas, J. T.; Stewart, J.; Saleh, B. E. A.; Teich, M. C., Polymer microcantilevers fabricated via multiphoton absorption polymerization. *Applied Physics Letters* **2005,** 86, (6), 064105-3.

(21) Driscoll, M. K.; McCann, C.; Kopace, R.; Homan, T.; Fourkas, J. T.; Parent, C.; Losert, W., Cell Shape Dynamics: From Waves to Migration. *PLoS Computional Biology* **2012,** 8, (3), e1002392.

(22) Driscoll, M. K.; Fourkas, J. T.; Losert, W., Local and global measures of shape dynamics. *Physical Biology* **2011,** 8, (5), 055001-1-9.

(23) Driscoll, M. K.; Kopace, R.; Li, L.; McCann, C.; Watts, J.; Fourkas, J. T.; Losert, W., The adventures of Dicty, the Dictyostelium cell. *Chaos: An Interdisciplinary Journal of Nonlinear Science* **2009,** 19, (4), 041110-1.

(24) Weiß, T.; Hildebrand, G.; Schade, R.; Liefeith, K., Two-Photon polymerization for microfabrication of three-dimensional scaffolds for tissue engineering application. *Engineering in Life Sciences* **2009,** 9, (5), 384-390.

(25) Weiß, T.; Schade, R.; Laube, T.; Berg, A.; Hildebrand, G.; Wyrwa, R.; Schnabelrauch, M.; Liefeith, K., Two-Photon Polymerization of Biocompatible Photopolymers for Microstructured 3D Biointerfaces. *Advanced Engineering Materials* **2011,** 13, (9), B264-B273.

(26) Connell, J. L. W., Aimee K.; Parsek, Matthew R.; Ellington, Andrew D.; Whiteley, Marvin; Shear, Jason B., Probing Prokaryotic Social Behaviors with Bacterial "Lobster Traps". *mBio* **2010,** 1, e00202-00210.

(27) Dawood, F. Q., Sijia; Li, Linjie; Lin, Emily; Fourkas, John T., Simultaneous Microscale Manipulation, Immobilization, and Fabrication in Aqueous Media. *Chemical Science* **2012,** in review.

(28) Pitts, J. D.; Campagnola, P. J.; Epling, G. A.; Goodman, S. L., Submicron multiphoton free-form fabrication of proteins and polymers: Studies of reaction efficiencies and applications in sustained release. *Macromolecules* **2000,** 33, (5), 1514-1523.

(29) Turunen, S.; Kapyla, E.; Terzaki, K.; Viitanen, J.; Fotakis, C.; Kellomaki, M.; Farsari, M., Pico- and femtosecond laser-induced crosslinking of protein microstructures: evaluation of processability and bioactivity. *Biofabrication* **2011,** 3, (4).

(30) Pitts, J. D.; Howell, A. R.; Taboada, R.; Banerjee, I.; Wang, J.; Goodman, S. L.; Campagnola, P. J., New photoactivators for multiphoton excited three-

dimensional submicron cross-linking of proteins: Bovine serum albumin and type 1 collagen. *Photochemistry and Photobiology* **2002,** 76, (2), 135-144.

(31) Engelhardt, S.; Hoch, E.; Borchers, K.; Meyer, W.; Kruger, H.; Tovar, G. E. M.; Gillner, A., Fabrication of 2D protein microstructures and 3D polymer-protein hybrid microstructures by two-photon polymerization. *Biofabrication* **2011,** 3, (2), 025003.

(32) Campagnola, P. J.; Delguidice, D. M.; Epling, G. A.; Hoffacker, K. D.; Howell, A. R.; Pitts, J. D.; Goodman, S. L., 3-dimensional submicron polymerization of acrylamide by multiphoton excitation of xanthene dyes. *Macromolecules* **2000,** 33, (5), 1511-1513.

(33) Hill, R. T.; Lyon, J. L.; Allen, R.; Stevenson, K. J.; Shear, J. B., Microfabrication of three-dimensional bioelectronic architectures. *Journal of the American Chemical Society* **2005,** 127, (30), 10707-10711.

(34) Li, L.; Driscoll, M.; Kumi, G.; Hernandez, R.; Gaskell, K. J.; Losert, W.; Fourkas, J. T., Binary and Gray-Scale Patterning of Chemical Functionality on Polymer Films. *Journal of the American Chemical Society* **2008,** 130, (41), 13512-13513.

(35) Farrer, R. A.; LaFratta, C. N.; Li, L.; Praino, J.; Naughton, M. J.; Saleh, B. E. A.; Teich, M. C.; Fourkas, J. T., Selective Functionalization of 3-D Polymer Microstructures. *Journal of the American Chemical Society* **2006,** 128, (6), 1796-1797.

(36) Formanek, F.; Takeyasu, N.; Tanaka, T.; Chiyoda, K.; Ishikawa, A.; Kawata, S., Selective electroless plating to fabricate complex three-dimensional metallic micro/nanostructures. *Applied Physics Letters* **2006,** 88, (8).

(37) Formanek, F.; Takeyasu, N.; Tanaka, T.; Chiyoda, K.; Ishikawa, A.; Kawata, S., Three-dimensional fabrication of metallic nanostructures over large areas by two-photon polymerization. *Optics Express* **2006,** 14, (2), 800-809.

(38) Lee, J. N.; Park, C.; Whitesides, G. M., Solvent Compatibility of Poly(dimethylsiloxane)-Based Microfluidic Devices. *Analytical Chemistry* **2003,** 75, (23), 6544-6554.

(39) LaFratta, C. N. Multiphoton Absorption Polymerization: Issues and Solutions. Ph.D. Dissertation, University of Maryland, College Park, MD, 2006.

(40) LaFratta, C. N.; Li, L.; Fourkas, J. T., Soft-lithographic replication of 3D microstructures with closed loops. *Proceedings of the National Academy of Sciences of the United States of America* **2006,** 103, (23), 8589-8594.

(41) Fischer, J.; von Freymann, G.; Wegener, M., The Materials Challenge in Diffraction-Unlimited Direct-Laser-Writing Optical Lithography. *Advanced Materials* **2010,** 22, (32), 3578-3582.

(42) Hell, S. W., Improvement of Lateral Resolution in Far-Field Fluorescence Light-Microscopy by Using 2-Photon Excitation with Offset Beams. *Optics Communications* **1994,** 106, (1-3), 19-24.

(43) Hell, S. W., Far-field optical nanoscopy. *Science* **2007,** 316, (5828), 1153-1158.

(44) Hell, S. W., Microscopy and its focal switch. *Nature Methods* **2009,** 6, (1), 24-32.

(45) Hell, S. W.; Wichmann, J., Breaking the Diffraction Resolution Limit by Stimulated-Emission - Stimulated-Emission-Depletion Fluorescence Microscopy. *Optics Letters* **1994,** 19, (11), 780-782.

(46) Colley, C. S.; Grills, D. C.; Besley, N. A.; Jockusch, S.; Matousek, P.; Parker, A. W.; Towrie, M.; Turro, N. J.; Gill, P. M. W.; George, M. W., Probing the reactivity of photoinitiators for free radical polymerization: Time-resolved infrared spectroscopic study of benzoyl radicals. *Journal of the American Chemical Society* **2002,** 124, (50), 14952-14958.

(47) Klar, T. A.; Jakobs, S.; Dyba, M.; Egner, A.; Hell, S. W., Fluorescence microscopy with diffraction resolution barrier broken by stimulated emission. *Proceedings of the National Academy of Sciences of the United States of America* **2000,** 97, (15), 8206-8210.

(48) Hirschfelder, J. O.; Curtiss, C. F.; Bird, R. B.; University of Wisconsin. Theoretical Chemistry, L., *Molecular theory of gases and liquids*. Wiley: 1954.

Chapter 2: Experimental Setup and Techniques

2.1 Introduction

All experimental conditions for multiphoton absorption polymerization (MAP) experiments are consistent with the exception of a few modifications that depend on the type of experiments being performed. This chapter focuses on methods for fabrication as well as the modifications made for different experiments performed in this work.

2.2 Optics Setup for Fabrication

2.2.1 Typical MAP Setup

Fabrication for MAP experiments used an 800 nm, pulsed laser source. In our setup, 532 nm light from a 5W Coherent Verdi laser was used to pump a titanium-sapphire ($Ti:Al_2O_3$) crystal contained within a Coherent Mira 900-F oscillator cavity. The output beam was centered at a wavelength of 800 nm with 200 fs pulses. When optimized, the laser can generate approximately 800 mW of power.

The beam power between the laser output and the sample was controlled using a combination of a half-wave plate and a polarizer. The size of the beam was expanded to approximately 10 mm in order to fill the back aperture of the microscope objective used. Exposure is limited with a shutter controlled by a computer.

The essential requirement for three-dimensional (3D) fabrication is the ability to move the photoresist relative to the focal point of the laser source or vice versa. This task can be accomplished in a number of ways. One method is to use galvanic scanning mirrors to move the focal point of the laser source in the transverse (XY) dimension before entering the microscope objective. This scheme moves the focal point relative to the sample in XY. Axial (Z) control in this method is accomplished using a vertical stage to move the photoresist up or down relative to the focal point.[1-3] Another method is to use an XY translation stage combined with a vertical stage so that the photoresist can move in all directions relative to the fixed focal point of the laser source. The method for 3D movement is to incorporate movement of the photoresist in all 3 directions through the use of a stage (or "nanostage" if position resolution is near or below 1 nm). The work presented here uses a combination of all three methods for a great degree of freedom for movement in 3D.

2.2.2 Inverted Microscope Setup

When the beam enters the inverted microscope (Zeiss Axiovert 100), Figure 2.1, it is reflected into a 1.45 NA, 100× oil-immersion microscope objective (Zeiss α Plan-FLUAR) using a dichroic mirror. The objective is fixed onto a rotation turret that allows for exchange of objectives. The objective mount can be moved vertically either manually or with joystick control to position the objective focal point within the sample.

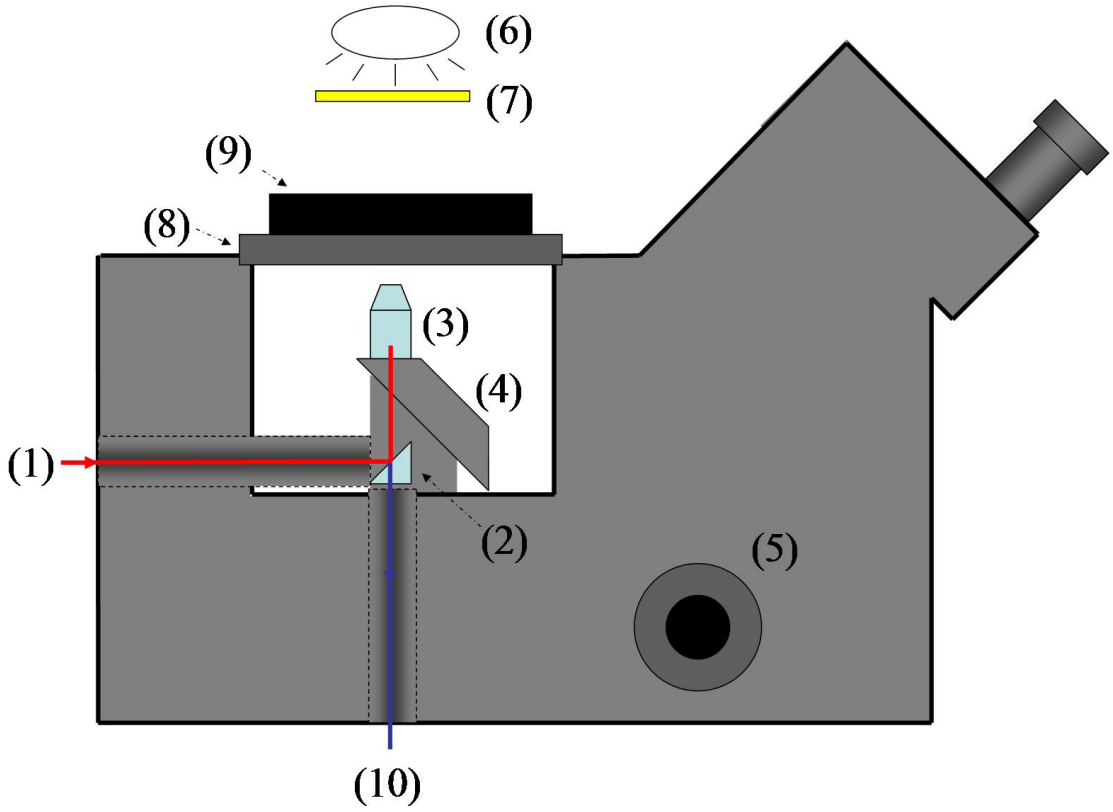

Figure 2.1. Diagram of the inverted microscope. The laser enters the microscope (1) and reflects off of dichroic mirror (2) into the microscope objective (3). The objective is located on rotational stage (4) that also moves vertically both manually (5) and with a joystick to focus on the sample. A light source (6) is filtered (7) before illuminating the sample. The sample is attached to an aluminum mount that is screwed in place atop two motorized stages: a translation stage (8) and a piezoelectric nanostage (9). Luminescence can be detected by avalanche photodiode detectors located beneath the microscope (10).

The progress of MAP fabrication can be viewed on a monitor through a CCD camera affixed to the microscope. Alternatively, any luminescence, produced through interaction of the laser with the sample can be viewed using avalanche photodiode detectors located below the microscope. The signal is transmitted downward, through the dichroic mirror into the detectors. An illumination source is located above the sample.

Two motorized stages are positioned above the objective. The first is a translation stage (Ludl) capable of moving in the X and Y directions via computer or joystick control. The second stage, attached atop the translation stage, is a piezoelectric nanostage (Physik

Instrumente) capable of X, Y, and Z control with a range of 200 μm in each direction and sub-nanometer resolution. The combination of the two stages allows for a greater range of movement with the capability to fabricate structures with high resolution.

2.2.3 Dual Beam Setup

For techniques, such as resolution augmentation through photo-induced deactivation (RAPID), that require two laser beams, a polarizing beam cube was used to combine the beams of orthogonal polarization before entering the microscope (Figure 2.2). For RAPID, a second Coherent Mira 900-F, Ti-sapphire was employed to produce a wavelength centered at 800 nm with, optimally, 1 W of output power. This second beam was set to be a continuous wave (CW) and served as the deactivation source. The laser power at the sample was controlled with a half-wave plate and a polarizer. The beam was expanded to fill the back aperture of the microscope objective. Additionally, a phase mask could be added to the beam path to alter the intensity distribution within the focal region. The phase mask used here has a circular region that creates a half-wave delay at 800 nm. This design deactivates primarily along the optical axis (Z-direction).

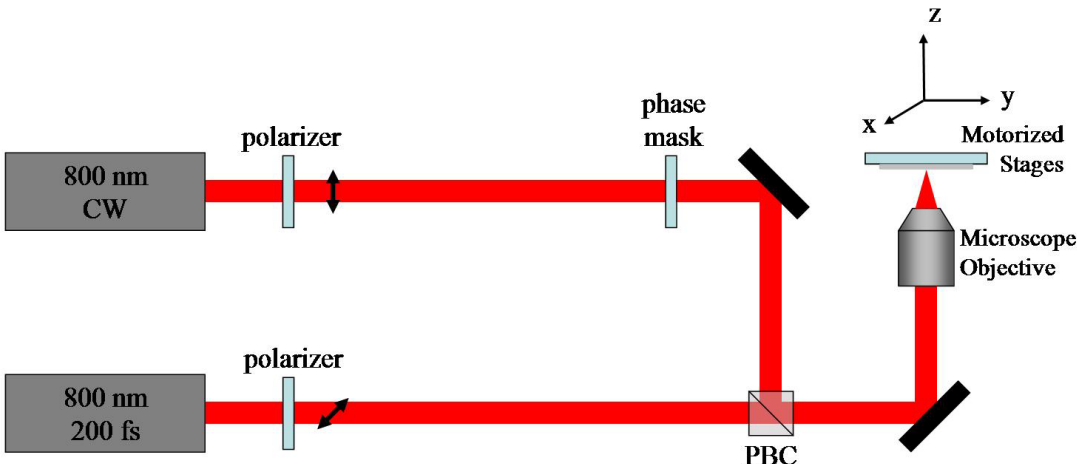

Figure 2.2. Diagram of the basic RAPID laser setup. Two 800 nm beams are employed: an excitation beam with 200 fs pulses and a CW deactivation beam. The polarizations of the beams are set orthogonally and the beams are combined in a polarizing beam cube. A phase mask can also be inserted in the deactivation beam path to deactivate in the Z-axis.

2.2.4 Overlapping Beams

To ensure precise overlap of laser beams in a dual beam experiment, multiphoton-absorption-induced luminescence (MAIL) was employed. In this technique, a glass slide containing gold nanoparticles on the surface was placed on an aluminum sample holder. Using a 100× oil-immersion microscope objective, the 800 nm pulsed laser, at low intensity, was scanned across an area containing a nanoparticle. The power of the laser was 1 to 5 mW at the sample. Multiphoton excitation of the nanoparticle resulted in luminescence that was recorded by an avalanche photodiode positioned below the microscope. The emission intensity was mapped as a function of excitation position to create an image.

Scanning of the laser beam can be accomplished in two ways. Method I was through the use of the scanning mirrors. If the scanning mirrors control both beams, altering the position of the beams on the scanning mirrors can be used to overlap the

beams. Here, the movement of the laser beam relative to a fixed particle creates the image. However, if the scanning mirrors control only one beam, then Method II is to scan the sample around the beam using the piezoelectric nanostage. Here, the movement of the particle relative to the fixed laser beam creates the image. The scanning is controlled by the LabVIEW program shown in Figure 2.3. Method II has a slower scan rate but it is required to produce an image with both beams.

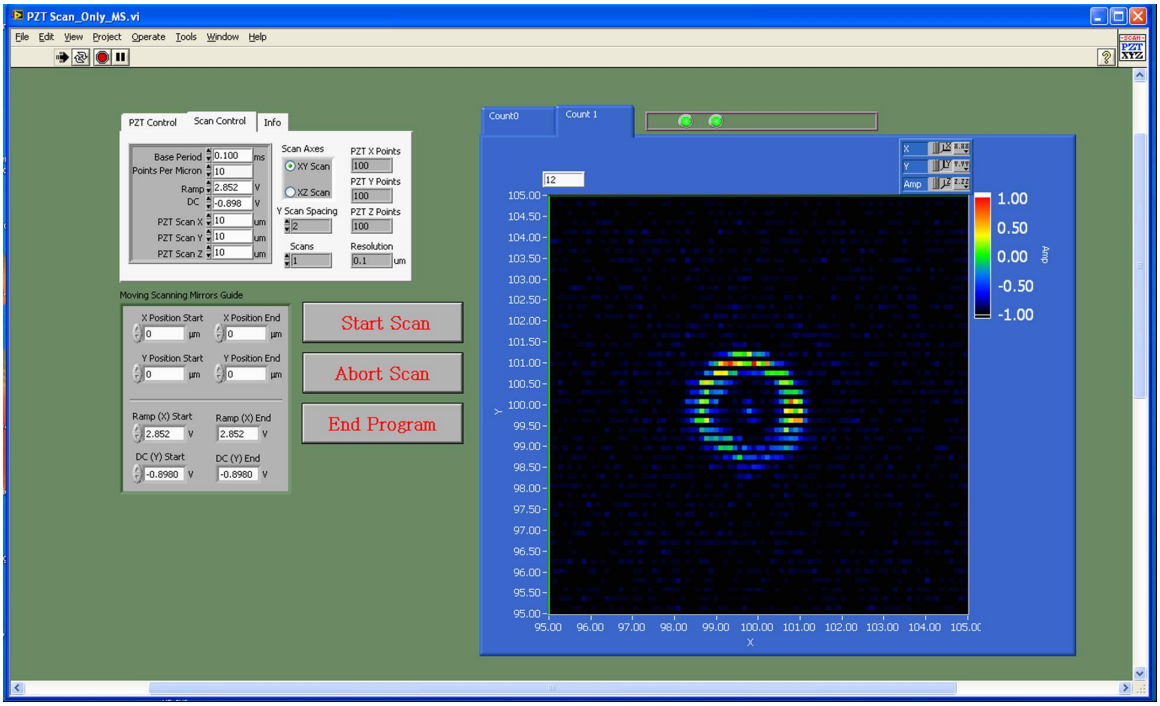

Figure 2.3. Front panel view of piezoelectric nanostage scanning program.

For the most efficient overlapping, the first step was to scan a gold nanoparticle with the laser beam using Method I (Step I, Figure 2.4). With the faster scans, the image refreshes and allows for the phase mask to be set at the optimal position within the deactivation beam path. Method II was then employed to overlap the beams, first by centering the fabrication beam and then moving the deactivation beam. The latter step is accomplished by changing the voltages applied to the scanning mirrors. Alignment can

be checked in each plane and the overlap can be verified, as seen in Figure 2.4. Once overlapped, the deactivation beam source can be changed to CW.

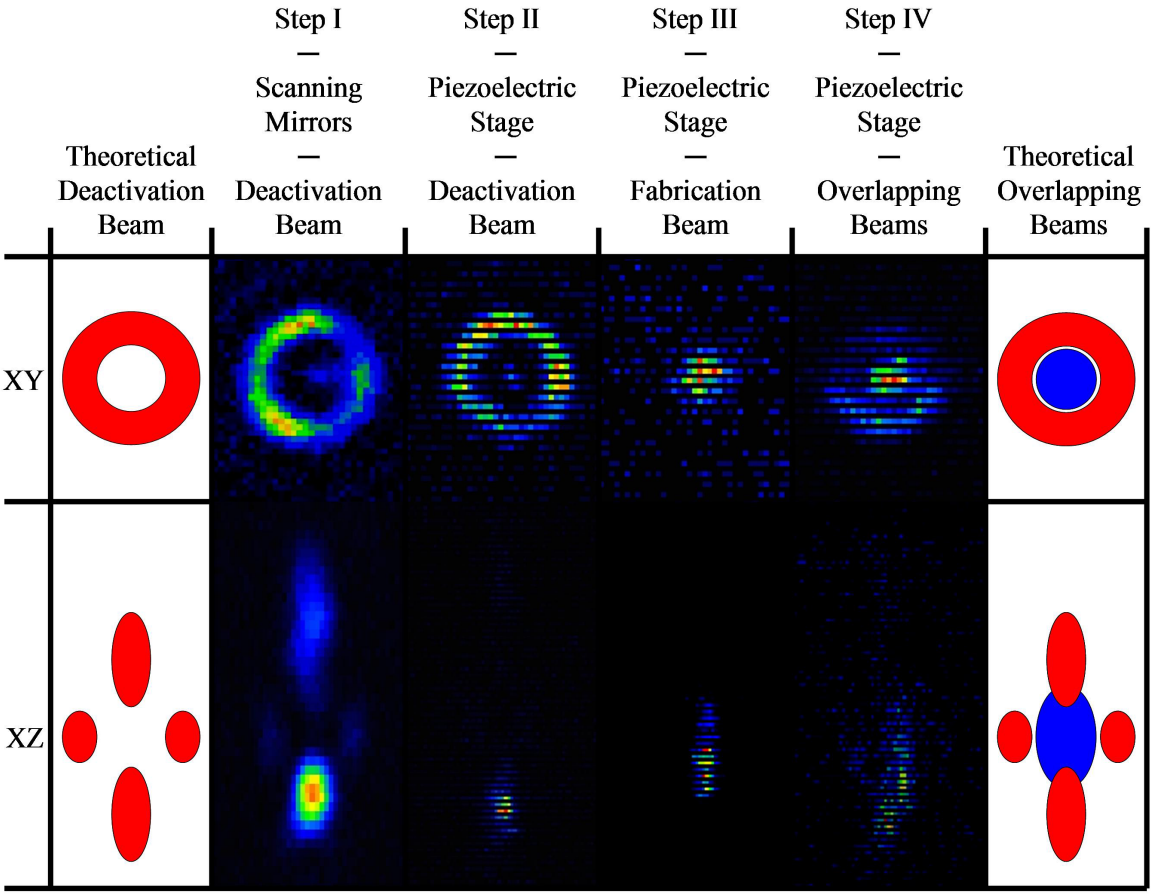

Figure 2.4. Luminescence images of RAPID beams produced by three-photon-absorption induced luminescence of a gold nanoparticle. (Step I) A particle is imaged using scanning mirrors controlling the deactivation beam and the phase masked put in the optimized position. (Step II) The same particle is found by scanning with the piezoelectric state. (Step III) The particle is centered with the piezoelectric nanostage using the fabrication beam as the excitation source. (Step IV) The deactivation beam is moved in XY by adjusting the voltage applied to the scanning mirrors to overlap with the fabrication beam. Both beams are collimated before entering the objective to ensure overlap in XZ plane.

2.2.5 Acousto-Optic Modulation

For exposure experiments, neither a chopper wheel nor a shutter was capable of providing the complex timing sequences required. A chopper wheel could provide the

short exposure resolution, however neither the specific number of exposures nor the delay between exposures could be controlled. A mechanical shutter allowed for more control of exposure conditions but could not provide the precision of the individual timing required. As a result, an acousto-optic modulator (AOM, IntraAction ME-805) was employed (Figure 2.5). In this capacity, an acoustic signal was applied to a Brewster-cut crystal to diffract the applied laser source. This process resulted in two beams, the primary, transmitted beam containing ~75% of the beam intensity and the secondary, diffracted beam containing the remaining intensity of ~25%. Application of the acoustic signal turns the diffracted beam on and off. It is this beam that was directed back into the normal beam path of the laser. The AOM was controlled by an electrical signal produced using a waveform generator (WFG, Wavetek Model 29). In order to perform complex timing sequences, an additional WFG was used as an external trigger source. The trigger WFG established the period and number of iterations while the source WFG was set to the individual exposure duration. The parameters for both WFGs were set and the exposures initiated using a LabVIEW program on a computer by using GPIB cables.[4]

For exposure experiments in which two beams were used, an additional AOM (IntraAction ME-815) was used in the second beam path. A third WFG provided the electronic control and the original external trigger source was attached to both signal-producing WFGs to ensure precise synchronization of the exposures.

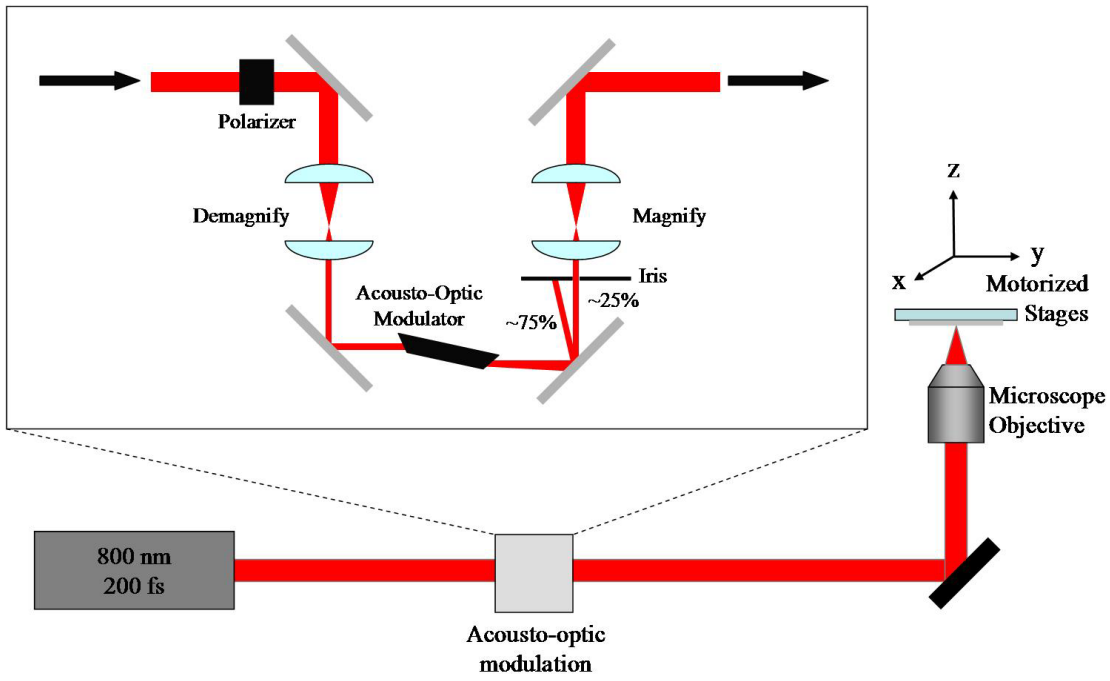

Figure 2.5. Diagram of acousto-optic modulation of the laser beam. The input beam was demagnified to make it small enough to pass through the acousto-optic modulator (AOM). Waveform generators controlled the formation of an acoustic signal that diffracted the beam. ~25% of the total beam intensity was diffracted, expanded and realigned into the beam path.

2.2.6 Other Wavelengths

Experiments requiring the use of a wavelength not producible by the Ti-sapphire oscillator (approximately 720 to 890 nm) resulted in the use of other sources directed into beam paths in a manner that would minimally affect the optics set up for the Ti-sapphire. The Coherent Verdi pumping lasers produce CW 532 nm light that can be diverted into the microscope. Additionally, an insertable helium-neon laser (Uniphase) produces CW light centered at 633 nm. For single-photon absorption experiments, a CW 405 nm diode laser (Vortran Stradus) producing 100 mW of power was used. This beam was magnified to ~10 mm and power control was accomplished using a wavelength-appropriate combination of a half-wave plate and a polarizer, as well as neutral density filters. A

long-pass filter (blocking wavelengths below 450 nm) was added to the microscope to prevent the 405 nm source from reaching the CCD camera. Additionally, a steel heat sink was attached to the laser diode module to disperse the heat.

2.3 Sample Preparation

2.3.1 Substrate Functionalization

To promote adhesion of polymerized acrylic structures on the substrates, glass cover slips were functionalized with terminal acrylate groups. Two different types of coverslips were used depending on the application: #1 Corning glass coverslips (25 × 25 mm) or #1.5 Zeiss glass coverslips (18 × 18 mm). A batch of coverslips was held on a quartz slide holder and placed in a plasma cleaner. A final oxygen pressure of ~200 mtorr was maintained and plasma was generated for 3 minutes to clean the coverslip surfaces. After plasma exposure, terminal acrylate groups were generated on the surface by immersion in an acrylate solution. The coverslips were placed into Teflon® slider holders and immersed in a solution containing, by volume, 93% anhydrous ethanol (Pharmco-Aaper), 5% deionized water and 2% (3-acryloxypropyl) trimethoxysilane (Gelest). Coverslips were left immersed, with constant stirring, overnight (~16 h). Subsequently, the Teflon® holders with coverslips were transplanted to an anhydrous ethanol bath to rinse for 1 hour with constant stirring, followed by removal and heating in an oven at 95 °C for 1 h to remove any remaining ethanol. Coverslips (henceforth acrylated substrates) were allowed to cool to room temperature and stored until required for fabrication experiments.

2.3.2 Bulk Photoresist Preparation

For each experiment, ~2 g of photoresist was prepared. An acrylate monomer resin was prepared by combining a 1:1 weight ratio of tris(2-hydroxyethyl) isocyanurate triacrylate (SR368, Sartomer) and ethoxylated (6) trimethylolpropane triacrylate (SR499, Sartomer), as shown in Figure 2.6. The mixture was stirred on a hot plate at 95 °C to reduce the viscosity, with occasional inversion and agitation and placement on a vortex mixer. These steps were repeated for ~30 min prior to addition of photoinitiator. The photoinitiator, used without further purification, was weighed directly into a test tube using either a spatula for solid powders (such as triarylmethane dyes) or a wooden applicator for liquids (such as Lucirin TPO-L). Photoinitiator percentages, by weight, in the photoresist ranged from 1.6% to 3% depending on the type of photoinitiator and the application. Using a disposable glass pipet, the acrylate monomer resin (at 95 °C) was then added at the appropriate weight to the photoinitiator to complete the photoresist. The test tube was then capped and covered by aluminum foil to avoid accidental light exposure. Mixing consisted of three steps: (1) 3 minutes in an oven at 95 °C, (2) vortex mixing for 30 s, and (3) constant inversion for 5 minutes. The steps were repeated two additional times. The sample was left to be constantly inverted overnight (~16 h) until just prior to fabrication experiments.

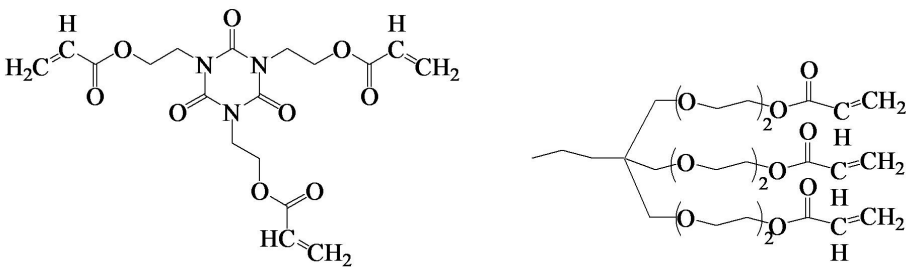

SR 368 SR 499

Figure 2.6. Triacrylate monomers used in MAP experiments: tris(2-hydroxyethyl) isocyanurate triacrylate (SR368) and ethoxylated (6) trimethylolpropane triacrylate (SR499).

Prior to use in experiments, the bulk mixtures containing solid photoinitiators were heated in an oven at 95 °C for 3 minutes, centrifuged at 3400 rpm for 5 minutes, reheated at 95 °C for 3 minutes, and syringe-filtered using a 0.20-μm-pore-size 30 mm nylon syringe filter (Fisher) to remove undissolved particles. All photoresists were finally centrifuged at 3400 rpm for 10 minutes to remove air bubbles.

Each freshly prepared photoresist could be used for a few days if required. Before reuse (more than 24 h after filtration), photoresists were heated to 95 °C for 3 minutes, placed on the vortex mixer for 30 s and centrifuged at 3400 rpm for 10 minutes. When photoresists were used months after initial experiments, the efficiency of polymerization was inconsistent. Therefore, a new photoresist was prepared for each experiment for consistent results.

2.3.3 Experimental Sample Preparation

A photoresist sample for experiments using an oil-immersion, 100× objective could be constructed in two different methods, as shown in Figure 2.7. In each case, a glass coverslip acted as a barrier between the oil and the photoresist. In order to integrate

the photoresist into the microscope setup, a glass slide (75 × 25 mm) was cut to two-thirds length. If fabricating on the "top" surface (Figure 2.7a), the acrylated substrate was secured using Scotch® Magic™ Tape (henceforth "tape") to the center of the glass slide. The tape also served as a separator allowing for photoresist thickness of ~30 µm. A small drop of photoresist was placed to the substrate using a wooden applicator. An additional glass coverslip of similar dimensions was applied on top, sandwiching the photoresist, and affixed using tape. This final coverslip acted as the barrier between the oil and the photoresist and must have a thickness of #1.5 (0.17 mm) or smaller to allow for the working distance of the microscope objective.

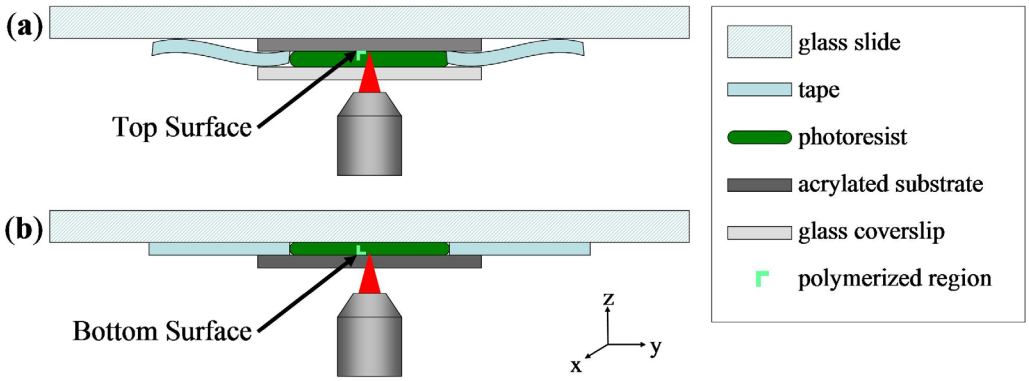

Figure 2.7. Schematic diagram of sample geometry. An acrylated substrate can be positioned so as to fabricate on either (a) the top or (b) the bottom of the photoresist. Tape is used to adhere the glass layers and act as ~30 µm spacer for the photoresist. Note: not drawn to scale.

If fabricating on the "bottom" surface (Figure 2.7b), tape was applied to the glass slide to provide the separation for photoresist to have a thickness of ~30 µm. A small drop of photoresist was applied to the glass slide. Finally the acrylated substrate was applied on top of the photoresist and affixed using tape. In this manner, the acrylated substrate also acts as the barrier between the immersion oil and the photoresist.

When the samples had been prepared, they were turned upside-down and screw-clamped into an aluminum sample mount. Immersion oil was applied to the microscope objective and the sample mount was screwed directly into the piezoelectric nanostage. The objective was then elevated until the focal distance was within the photoresist and polymerization took place.

2.3.4 Sample Development

When fabrication was complete, the microscope objective was lowered away from the sample and the mount was unscrewed from the piezoelectric nanostage. The sample slide was unclamped from the mount and the acrylated substrate removed from the slide. The acrylated substrate was then developed to remove the unpolymerized photoresist. The first two development steps were consecutive, 2 minute immersions in two different beakers containing *N,N*-dimethylformamide (DMF) to remove any remaining unpolymerized acrylate monomer resin. The substrate was then immersed in two consecutive ethanol washes for 2 minutes each to remove any remaining photoinitiator. If complex 3D structures were fabricated, an additional, 1 minute wash in hexanes was used to remove the ethanol. This step avoided or minimized damage, in the form of collapsing structures, due to surface tension that can occur if solvent evaporation is too slow.

2.4 3-Dimensional Fabrication Programming

A LabVIEW program controlled motion in three dimensions using a combination of scanning mirrors, an XY translation stage, and a piezoelectric XYZ nanostage. The

devices are controlled using a single LabVIEW program that read a text file containing code that includes the serial movement in the X, Y, and Z directions. In the course of experiments for this work, additional capabilities and instrumental control were integrated into the program. These new features included single-beam acousto-optic modulation, dual-beam acousto-optic modulation, and high-speed fabrication. Figure 2.8 shows the LabVIEW user interface of the program and Figure 2.9 shows the program that reads the code.

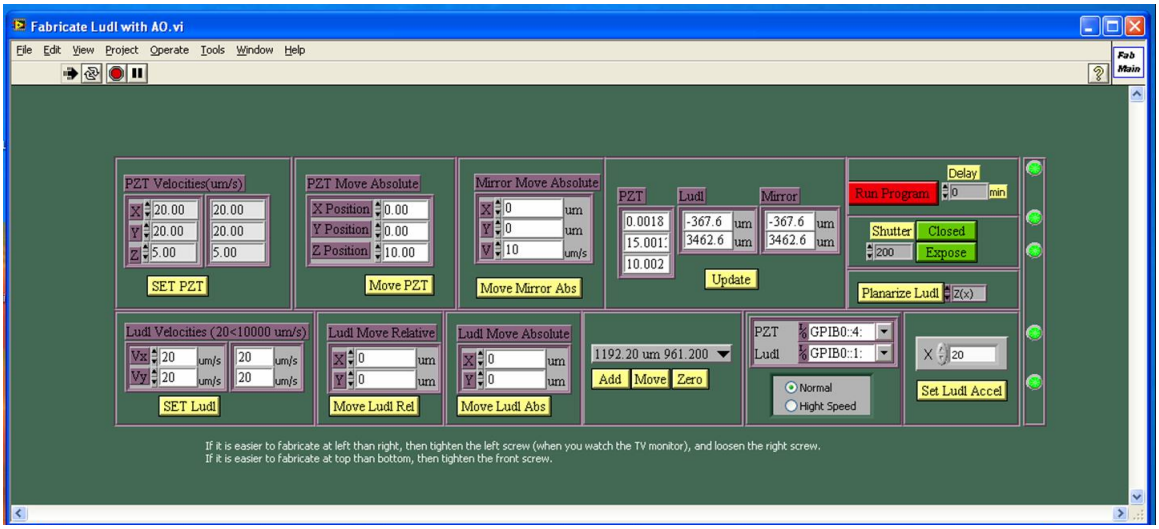

Figure 2.8. Front panel of the LabVIEW program used for control of the piezoelectric nanostage, the translation stage, and the scanning mirrors.

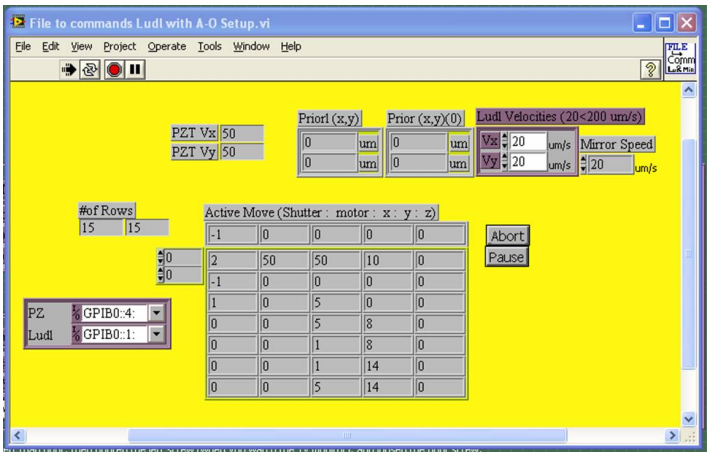

Figure 2.9. Front panel of LabVIEW program that reads commands for fabrication.

As seen in an example program in Figure 2.10, the first column signifies the commands to be used in the remainder of the line of code. The code is organized according to Figure 2.11 and represents the current capabilities. Complex 3D structures can be created using individual points or formulas to determine X, Y, and Z positions.

Row	Column 1	Column 2	Column 3	Column 4	Column 5	Column 6	
1	2	25	25	5			Set piezoelectric stage velocity
2	-1	0	0	0	0	0	Closed shutter and move
3	1	0	10	0	1	1	Open shutter and move
4	0	0	10	20	0	1	Repeat "Row 3" command
5	0	0	0	20	1	1	
6	0	0	0	0	0	0	
7	-1	0	20	0	0		
8	7	50	50				Set translation stage velocity
9	1	1	50	0			
10	0	1	0	25			
11	0	1	-50	0			
12	0	1	0	-25			
13	-1	1	75	0			
14	1	2	25	0	0		
15	0	2	25	10	0		
16	0	2	0	10	0		
17	0	2	0	0	0		
18	-1	0	0	50	0		
19	4	0	0	50	0	50	Expose for 50 ms
20	4	0	2	50	0	75	
21	4	0	4	50	0	100	
22	3						Pause until resumed by user
23	1	0	0	55	0		
24	8	1	1	1			Single beam acousto-optic exposure
25	1	0	2	55	0		
26	8	1	0.5	1			
27	1	0	4	55	0		
28	8	0.1	0.1	0.5			
29	1	0	0	60	0		
30	9	0.5	0.5	1			Dual beam acousto-optic exposure
31	1	0	2	60	0		
32	9	0.5	0.5	2			
33	1	0	4	60	0		
34	9	0.1	0.5	0.5			
35	-1	0	0	75	0		
36	3						
37	7	10000	25				
38	10	5000					Move translation stage in x-direction at high
39	-1	0	0	0	0		

Figure 2.10. Sample program to control aspects of fabrication.

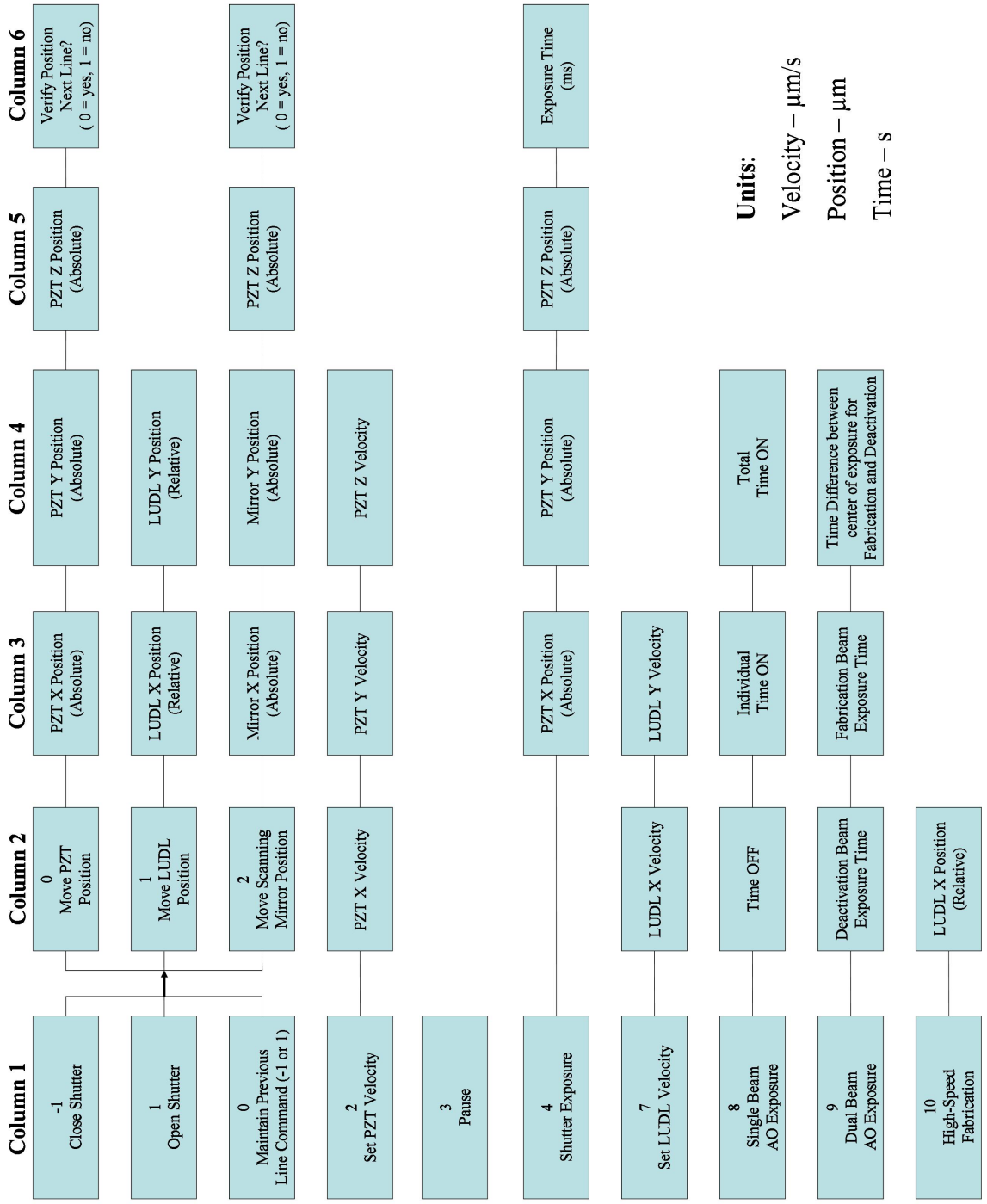

Figure 2.11. Flow diagram of fabrication programming. The first column indicates the command to be followed for the rest of the line. Each command is programmed in LabVIEW to control an aspect of fabrication.

2.5 Analysis with Scanning Electron Microscopy

When working in the tens to hundreds of nanometers scale, the most efficient method for analyzing feature sizes is to use scanning electron microscopy (SEM). Accurate measurements can only be made in the XY plane and non-conductive polymeric structures must be coated with metal for imaging. Measurements of small features must therefore take into account the added size from deposited metal. For very small features in which depositing metal is not an option, fabrication can be performed on an acrylate-functionalized indium-tin-oxide (ITO) substrate. The conductive ITO is transparent so it allows for fabrication using the sample preparation steps described above.

For SEM imaging, a sample is cut to approximately 7 × 7 mm and attached to a circular, 15 mm diameter SEM mount using carbon tape with adhesive on both sides. The sample is then placed into a sputter coater (Cressington 108) with a palladium-platinum target (57 × 0.1 mm, Ted Pella) and subjected to argon plasma. A thin layer, ~25 nm, of palladium-platinum is deposited on the slide. All samples described here were imaged in a Hitachi SU-70 scanning electron microscope at 5.0 eV.

Line widths described in this work were measured from SEM images using a LabVIEW program (front panel in Figure 2.12). Each image contained the center 6 μm, length-wise, of four fabricated lines. The accuracy of the analysis was optimized by summing the pixel values for each column or x-value. The width of each line was then extracted using the full width at half-maximum (FWHM) pixel value and the scale bar for conversion to nanometers. Value for the widths of the four lines and an average value were recorded.

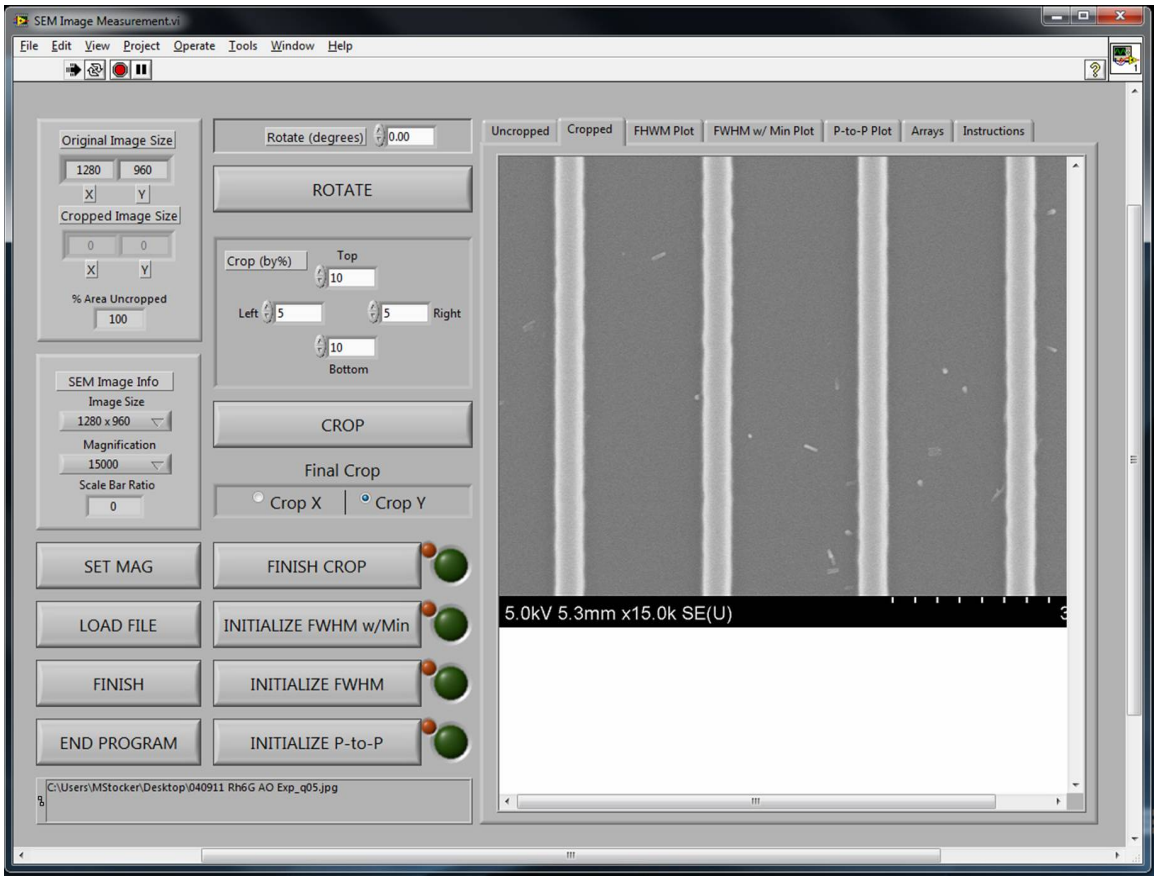

Figure 2.12. Front panel of the LabVIEW program used to measure line widths from SEM images.

Voxel and exposure studies were performed by measuring the maximum XY feature sizes for 3 to 4 exposure areas in imaging software (GIMP 2.0) and converted to nanometers using the scale bar ratio. Averages were then calculated.

References:

(1) Nielson, R.; Koehr, B.; Shear, J. B., Microreplication and Design of Biological Architectures Using Dynamic-Mask Multiphoton Lithography. *Small* **2009,** 5, (1), 120-125.

(2) Li, Y.; Qi, F. J.; Yang, H. H.; Gong, Q. Z.; Dong, X. M.; Duan, X., Nonuniform shrinkage and stretching of polymerized nanostructures fabricated by two-photon photopolymerization. *Nanotechnology* **2008,** 19, (5).

(3) Maruo, S.; Ikuta, K., Submicron stereolithography for the production of freely movable mechanisms by using single-photon polymerization. *Sensors and Actuators A - Physical* **2002,** 100, (1), 70-76.

(4) Stocker, M. P.; Fourkas, J. T., Elucidating the kinetics and mechanism of RAPID lithography. *Proceedings of SPIE* **2012,** 8249, 824902-1-7.

Chapter 3: Self-Deactivating MAP Photoinitiators[‡1]

3.1 Introduction

As a result of the Abbe criterion (Eq. 1.1), methods for improving resolution in lithography must go beyond the use of simple lens systems to deliver a laser source to a photoresist. Resolution augmentation through photo-induced deactivation (RAPID) demonstrates[2,3] that by applying a second laser source, the photochemistry of excitation is altered. Therefore, further improvement is sought by manipulating the fabrication methods through chemical means.

In the original implementation of RAPID, ultrafast pulses with a center wavelength of 800 nm were used to activate a photoresist through two-photon absorption. Deactivation was accomplished with a continuous-wave (CW) laser that was also tuned to 800 nm. With a phase-masked deactivation beam, axial resolution as fine as 40 nm ($\lambda/20$) has been demonstrated.

RAPID relies on the use of a photoinitiator that, after excitation, can be deactivated and regenerated by the deactivation beam before it is able to initiate polymerization of the photoresist. In the original implementation of RAPID,[3] malachite green carbinol base (MGCB, **1**; Figure 3.1) was used as the photoinitiator in a resist composed of viscous acrylic monomers. Although MGCB is not a conventional radical

[‡] Reprinted in part with permission from *Nat. Chem.*, *3* Stocker, M. P.; Li, L.; Gattass, R. R.; Fourkas, J. T. "Multiphoton photoresists giving nanoscale resolution that is inversely dependent on exposure time," 223-227, Copyright 2011 by the Nature Publishing Group.

photoinitiator, it was chosen for RAPID due to the combination of its ability to drive multiphoton absorption polymerization[4-6] (MAP) with short-pulsed, 800 nm light and its large extinction coefficient, which would be favorable for deactivation through stimulated emission depletion[7] by a second, picosecond pulsed light source. However, the deactivation of MGCB proved to be insensitive to the delay time between excitation and deactivation pulses over the experimentally available span of 13 ns, indicating that stimulated emission is not responsible for the deactivation process. Instead, deactivation involves a long-lived intermediate created upon photoexcitation of MGCB, which is why deactivation is efficient even with a CW deactivation laser. It was reasoned that by investigating molecules that are related to MGCB, it could be possible to improve upon the properties of this intermediate state to accomplish deactivation more efficiently. Highly efficient deactivation is an important step towards implementing RAPID at the wafer scale.

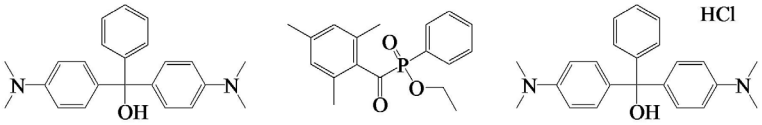

(1) **(2)** **(3)**

Figure 3.1. Radical photoinitiators used here for multiphoton absorption polymerization: malachite green carbinol base (MGCB, 1), Lucirin TPO-L (2), and malachite green carbinol hydrochloride (MGC·HCl, 3).

It is demonstrated here that for a broad class of common dye molecules, deactivation is so efficient that the ultrafast laser pulses used for excitation can also deactivate the photoinitiator. A remarkable consequence of this efficient deactivation is that the transverse dimension of fabricated features is proportional to the fabrication velocity. In other words, lower exposures can lead to larger feature sizes than higher

exposures. Additionally, it is demonstrated that by combining two different photoinitiators, it is possible to create a photoresist in which the transverse resolution is independent of fabrication velocity over a wide range of velocities.

3.2 Materials and Methods

Acrylic photoresists were prepared as described in Section 2.3.2. MAP, specifically two-photon polymerization, was performed using the 200 fs pulsed, 800 nm laser source while single-photon polymerization was performed using the CW, 405 nm diode laser source. Fabrication was controlled using the piezoelectric nano-stage with velocity trend measurements made at linear velocities ranging from 1 to 200 μm/s. For applicable illustrations of fabrication trends, pyramids were created. Here, each successive layer was constructed at decreasing scanning velocities of 100 μm/s for the first (lowest) layer followed by layers fabricated at 75, 50, and 25 μm/s, respectively. The direction of scanning was from left to right (and right to left) in the images shown.

3.3 Results and Discussion

3.3.1 PROVE Dependence

In MAP, an ultrafast laser beam is focused tightly into a photoresist. Owing to the inherent nonlinearity of the multiphoton absorption and polymerization processes, polymerization occurs only within the focal volume of the laser. When a conventional radical photoinitiator is used for MAP, the feature size grows with increasing exposure time once the threshold for exposure has been exceeded. If the laser focal point is moved

through the photoresist at a constant velocity, a line of constant thickness is created. The higher the velocity, the thinner the line, because any given point along the line receives less exposure. This behavior is illustrated in Figure 3.2a for a typical radical photoinitiator, Lucirin TPO-L (**2**, Figure 3.1)[8], in an acrylic photoresist excited with ultrafast pulses at a wavelength of 800 nm. Thus, the transverse resolution of a line decreases approximately linearly with the fabrication velocity for a given laser power (Figure 3.2b). One consequence of this exposure dependence is that when more complex structures are created, there is an increase in thickness at the turning points, where the laser dwells for a longer period. Shown in Figures 3.2c-e are images of a pyramid created in an acrylic photoresist with Lucirin TPO-L as the photoinitiator. Significant ridges are observed at the turning points of the scans and are most evident at the lowest scan velocities.

For conventional MAP (that is, without a deactivation beam), when MGCB (**1**) in an acrylic photoresist is excited with ultrafast, 800 nm pulses the velocity dependence of the feature size is similar to that of a standard photoinitiator (Figure 3.3). The ridges at the turning points in the pyramids are considerably larger when Lucirin TPO-L is the photoinitiator than when MGCB is used, which is consistent with the weaker velocity dependence observed for the line width in this velocity range, as shown in Figure 3.3b.

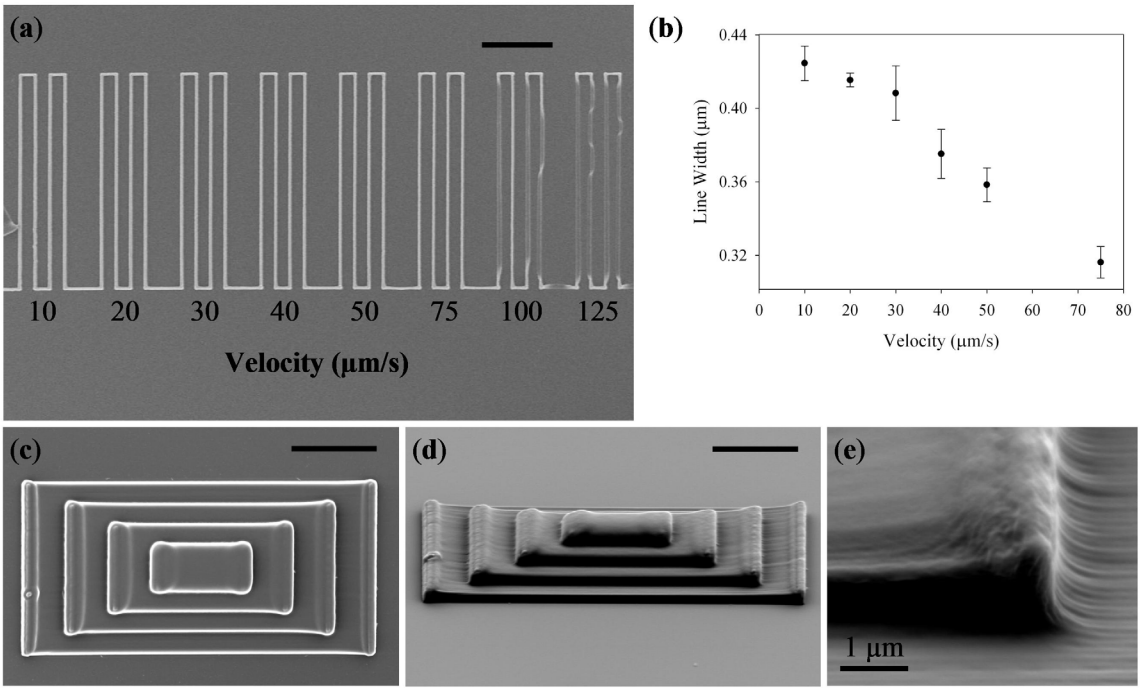

Figure 3.2. Fabrication with Lucirin TPO-L. Lines fabricated at different velocities in acrylic photoresist (a) with corresponding transverse resolution as a function of fabrication velocity (b). Error bars represent ±1 standard deviation. Top (c) and 60° tilt (d) views of pyramid and turn points (e) created with MAP. Successive levels of the pyramid (from bottom to top) were created with velocities of 100, 75, 50, and 25 µm/s. All scale bars are 10 µm unless overwise noted.

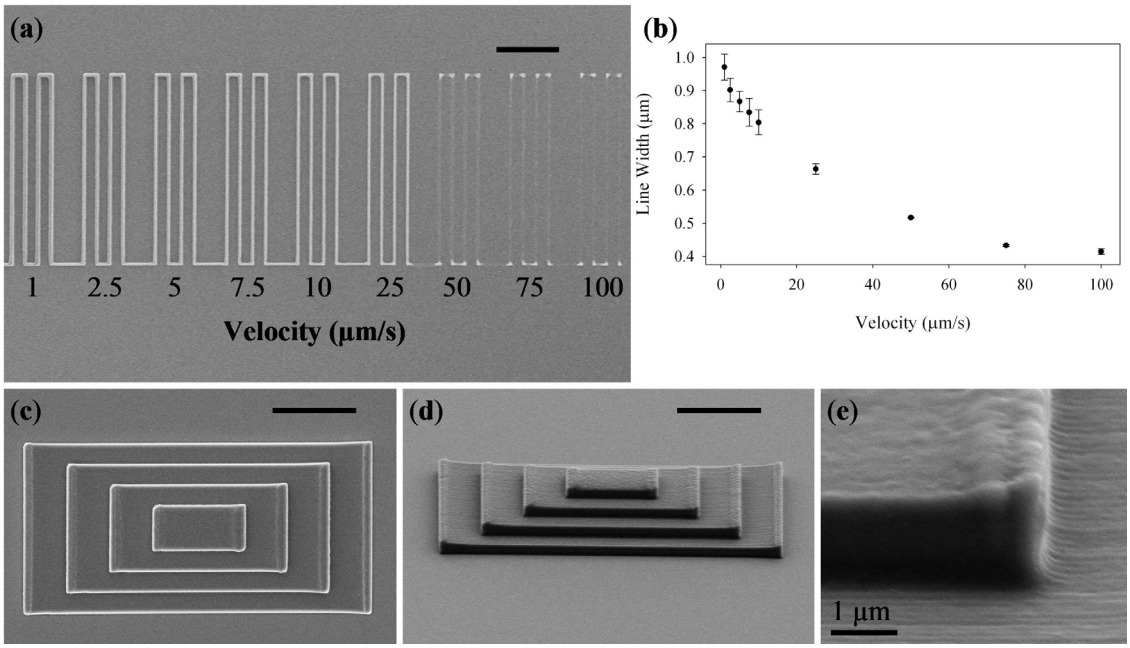

Figure 3.3. Fabrication with MGCB. Lines fabricated at different velocities in acrylic photoresist (a) with corresponding transverse resolution as a function of fabrication velocity (b). Error bars represent ±1 standard deviation. Top (c) and 60° tilt (d) views of pyramid and turn points (e) created with MAP. Successive levels of the pyramid (from bottom to top) were created with velocities of 100, 75, 50, and 25 µm/s. All scale bars are 10 µm unless overwise noted.

It was discovered that when malachite green carbinol hydrochloride (MGC·HCl, **3**; Figure 3.1) was used as the photoinitiator, the observed trend was a line width having a proportional velocity (PROVE) dependence. Figure 3.4a shows lines created in an acrylic photoresist at different velocities with MGC·HCl as the photoinitiator. At the lowest fabrication velocities, no lines are apparent. As shown in Figure 3.4b, for somewhat higher velocities the transverse line width grows linearly with the fabrication velocity. As a result of the PROVE dependence, the height of the pyramid structures tapers off at the turning points rather than increasing (Figures 3.4c-e).

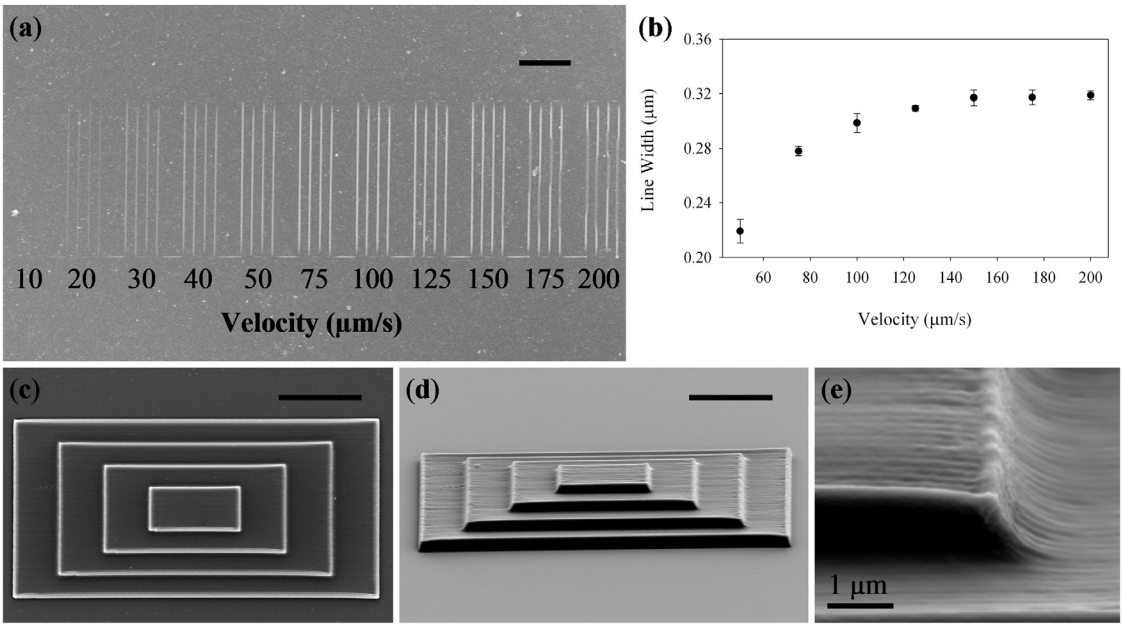

Figure 3.4. Fabrication with MGC·HCl. Lines fabricated at different velocities in acrylic photoresist (a) with corresponding transverse resolution as a function of fabrication velocity (b). Error bars represent ±1 standard deviation. Top (c) and 60° tilt (d) views of pyramid and turn points (e) created with MAP. Successive levels of the pyramid (from bottom to top) were created with velocities of 100, 75, 50, and 25 µm/s. All scale bars are 10 µm unless overwise noted.

3.3.2 Photoinitiator Studies

To investigate the cause of the PROVE dependence observed for MGC·HCl, other photoinitiator molecules containing similar triarylmethane (or triphenylmethane) backbones were tested. Synthetic dyes of these types have been studied for more than a century and a large number exist both in the literature and commercially for purposes such as textile dyes, biological stains, and pH indicators.[9] The intensely colored dyes consist of different functional groups and for ionic dyes, include: (1) a chromophore, (2) an auxochrome, and (3) a counter-ion. The chromophore produces the color, and for the dyes used here consists primarily of a quinonoid benzene ring containing an imidium cation (Figure 3.5a).[9] The auxochromes are subgroups that are bound to the chromophore and can influence the wavelength(s) of peak absorption and as well as the overall absorption strength. Finally, the counter-ion balances the charge of the ionic dye molecule and creates a stable salt. For the cationic dyes, the counter-ion is usually a chloride anion. It has been noted that unless the counter-ion itself is a chromophore, the only consequence it should have on the properties of the dye is in solubility.[10] In light of this information, the variables considered for different photoinitiator molecules were the overall charge, counter-ions for anionic or cationic dyes, and the position of substituents, such as nitrogen and oxygen, on the arene rings.

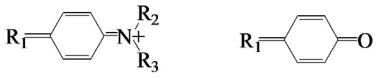

(a) **(b)**

Figure 3.5. Chromophores of triarylmethane, diarylmethane and xanthene dyes studied here. A quinonoid benzene ring contains either the imidium cation (a) or the hydroxyl group (b).

The first hypothesis was that, in the presence of the acrylic monomers, the hydroxide detached from the MGC·HCl leaving a positive charge on the central carbon. The very presence of color when the dye is dissolved in the acrylic monomer suggests this picture to be true. This scheme would also differentiate it from MGCB in the presence of a hydrochloride. Resonance stabilization allows the cation to be localized at either the central carbon atom (**4a**) or one of the two nitrogen atoms (**4**), shown in Figure 3.6. The chloride ion serves as the counter-ion. The result is a commercially-available, analytical-grade triarylmethane dye called malachite green chloride (**4**). (As such, MGC·HCl will henceforth be depicted by **4**.) Due to the PROVE-like nature of fabrication in the presence of MGC·HCl, other cationic dyes of this type, as well as their analogous neutral and anionic species were tested for indications as to the cause of PROVE dependence.

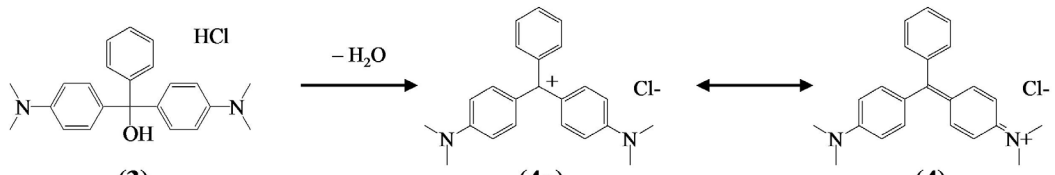

Figure 3.6. Conversion of MGC·HCl (3) to resonance-stabilized forms of malachite green chloride: the carbocation (4a) and the imidium (4).

In order to study PROVE dependence, the first comparison was made between malachite green oxalate (MGO, **5**) and MGC·HCl, for which the only difference was the form of the counter-ion. MGO, too, was found to have a PROVE dependence and fabricated in such manner as to determine that the counter-ion had minimal effect on the PROVE trend. This results was supported by the UV-visible absorption spectroscopy of both MGC·HCl and MGO which showed that both dyes had the same absorption (Figure

3.7a). It was concluded that the identity of the counter-ion had little to no effect on polymerization.

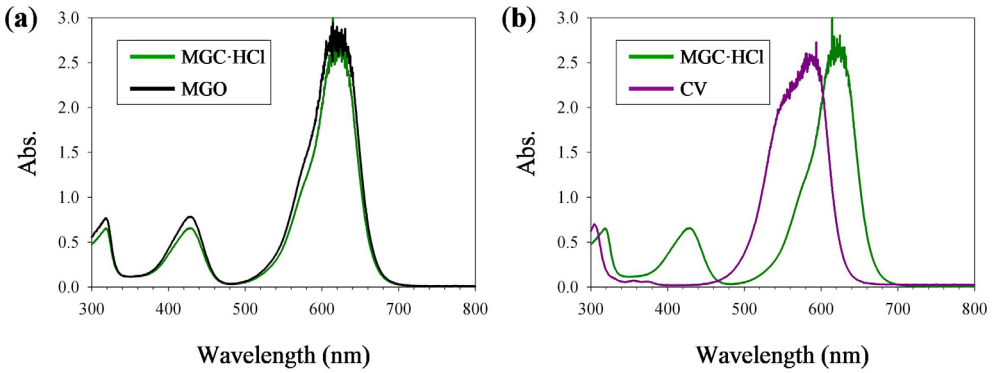

Figure 3.7. UV-Visible absorption spectra for (a) MGC·HCl and MGO, in ethanol, showing that counter-ion has little effect on absorption; (b) MGC·HCl and crystal violet (CV, 9) showing the blue shift of dyes that are more symmetric.

MGC·HCl and MGO have four auxochromes each: two tertiary amines each containing two methyl groups. To study the impact of auxochromes on PROVE dependence, a number of other cationic triarylmethane dyes were tested. Each dye possessed different auxochromes, including those with varying amine groups or the addition of atoms or chains of atoms to the phenyl groups.[10] Nearly all were shown to exhibit a varying degree of PROVE dependence when using ultrafast, 800 nm pulses. It was concluded that the type of auxochrome determined the degree to which a dye PROVE dependence was observed. It is logical to conclude that PROVE dependence cannot continue to hold for arbitrarily high velocities; at some relatively high velocity, exposure would be too short to induce polymerization. Therefore, at some velocity point, feature size should begin to decrease with increasing velocity or polymerization should stop abruptly. The former condition was observed for some dyes as a maximum in

feature size was evident at higher velocity before a conventional velocity dependence took over.

The diaminotriarylmethane dyes tested included malachite green chloride (as MGC·HCl), MGO (**5**) and brilliant green (**6**). The addition of an amine to the third phenyl group forms the triaminotriarylmethane dyes and results in a blue shift in the primary absorption peaks (Figure 3.7b). Dyes tested include pararosaniline chloride (**7**), methyl violet (**8**), crystal violet (**9**), and methyl green (**11**). Similar molecules with three amino groups include a triaminodiphenylnapthylmethane, Victoria blue R (**10**).

To further investigate the impact of auxochromes on PROVE, strongly fluorescent molecules such as cationic rhodamines were studied, and also exhibited PROVE dependence. Rhodamines, a subclass of xanthene dyes, contain the triarylmethane backbone with the addition of an oxygen connecting two of the benzene rings to form a heterocyclic six-member ring. Dyes tested included rhodamine B (**12**), rhodamine 6G (with both the chloride, **13**, and perchlorate, **14**, counter-ions), and rhodamine 123 (**15**). Auramine O (**16**), a commercially available cationic diarylmethane dye was found to have a PROVE dependence as well. Additionally, an analogue to auramine O, acridine orange (**17**) fabricated with a PROVE dependence and may extend this trend to other acridine dyes (those where a nitrogen links the two phenyl groups creating an anthracene-like molecule). [It should be noted that for some dyes that absorb strongly in the green to yellow region, it becomes necessary to use a long-pass filter for the illumination source that eliminates wavelengths below 600 nm.]

Several cationic dyes that were tested did not exhibit a PROVE dependence. Xanthenes rhodamine 101 (**21**) and rhodamine 110 (**22**) both have a conventional

velocity dependence. Rhodamine 101 exists as a zwitterions, which may explain its fabrication trend. This result also suggests that there must be a net negative charge on the molecule for PROVE dependence. The conventional velocity behavior of rhodamine 110 is likely due to the formation of a lactone in the acrylic resin, similar to the neutral rhodamine B base (**20**). Even though rhodamine 110 is structurally similar to rhodamine 123, the PROVE-like dependence in rhodamine 123 and not in rhodamine 110 could be explained by the methyl group on the carboxylate on rhodamine 123, which might prevent it from forming a lactone.

Analogues to the diarylmethane and acridine dyes, azin dyes in the form of neutral red (**25**) and safranin O (**26**, also a heterocyclic analogue to triarylmethanes) were tested. These were found to have conventional velocity dependence, however. This observation implies a central carbon atom is required for PROVE, possibly due to the formation of a carbocation as an intermediate for initiation of polymerization.

To determine if PROVE dependence was only possible with cationic dyes, neutral analogues of the dyes listed above were tested. The neutral species is usually in the form of the leuco (R-H, where R is the central carbon), carbinol (R-OH), lactone (R-COO-R') or zwitterion. In their pure form, these neutral species should be colorless, as the central carbon is unable to form resonance structures. The presence of color in some neutral species demonstrates a degree to which the environment (i.e., the acrylic monomer) affects the resonance stabilization of the central carbon atom. In each case, the neutral species resulted in a conventional velocity dependence. MGCB (**1**) and pararosaniline base (**18**) were tested as the carbinol base forms of MGC·HCl (**4**) and pararosaniline chloride (**7**), respectively. Crystal violet lactone (**19**) and rhodamine B base (**20**) are the

cyclic ester forms of crystal violet (**9**) and rhodamine B (**12**), respectively. Additionally, fluorescein (**23**) and rose bengal (**24**), which have been previously tested,[11] were used and found to have a conventional velocity dependence in this acrylic resin. In these two examples the chromophore is a quinonoid benzene ring containing a hydroxyl group (Figure 3.5b). Cationic analogues of these dyes have not yet been tested but may be PROVE photoinitiators. Although not a dye because it lacks the amino groups to form a chromophore, triphenylmethanol (**27**) was tested as a control and, as expected, did not initiate polymerization.

Finally, anionic dyes such as patent blue VF (**28**), light green SF (**29**), and sulforhodamine B (**30**) were tested and resulted in no polymerization when using ultrafast, 800 nm pulses. In these instances, the analogues to the cationic dyes (the former two triarylmethanes and the latter rhodamines) contain a varying number of sulfate groups to provide the negative charge of the dye molecule. The complete results are summarized in Figure 3.8, in which the dyes are arranged according to their fabrication trend and dye classification.

PROVE Dependence

Triarylmethanes

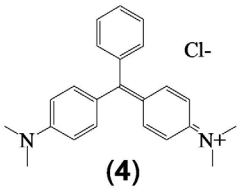

(4)

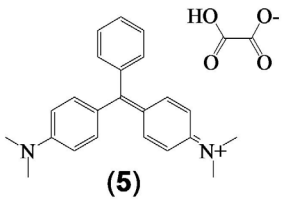

(5)

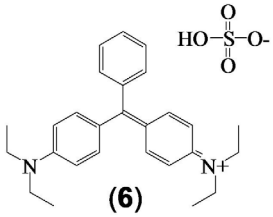

(6)

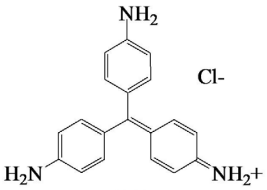

(7)

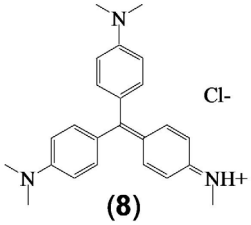

(8)

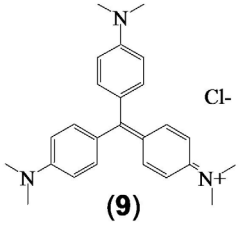

(9)

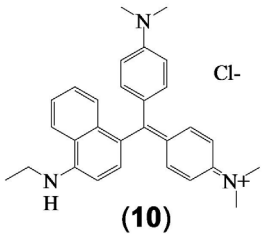

(10)

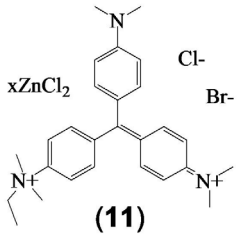

(11)

Xanthenes

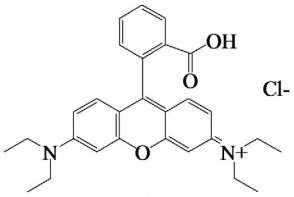

(12)

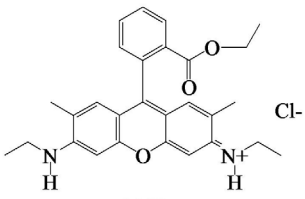

(13)

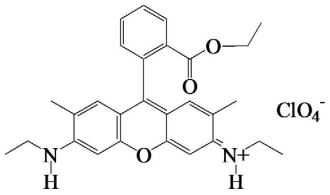

(14)

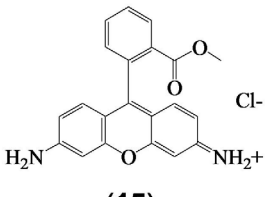

(15)

Diarylmethane

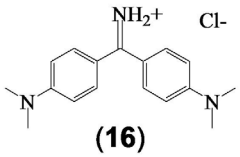

(16)

Other

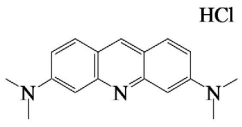

(17)

Conventional Velocity Dependence

Triarylmethanes

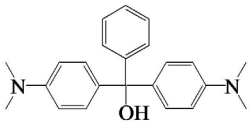

(1)

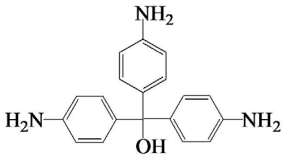

(18)

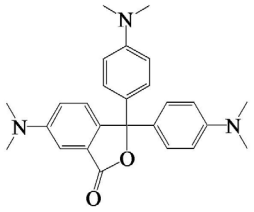

(19)

Xanthenes

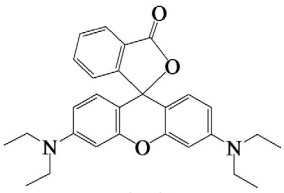

(20)

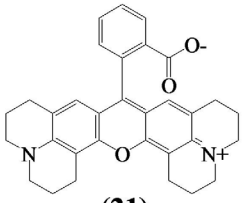

(21)

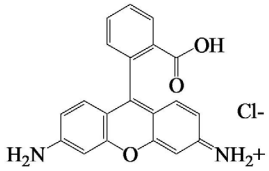

(22)

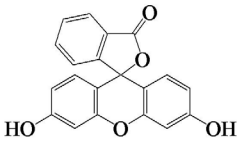

(23)

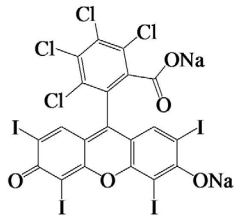

(24)

Others

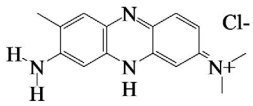

(25)

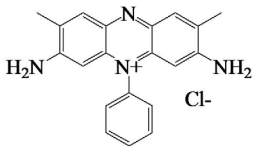

(26)

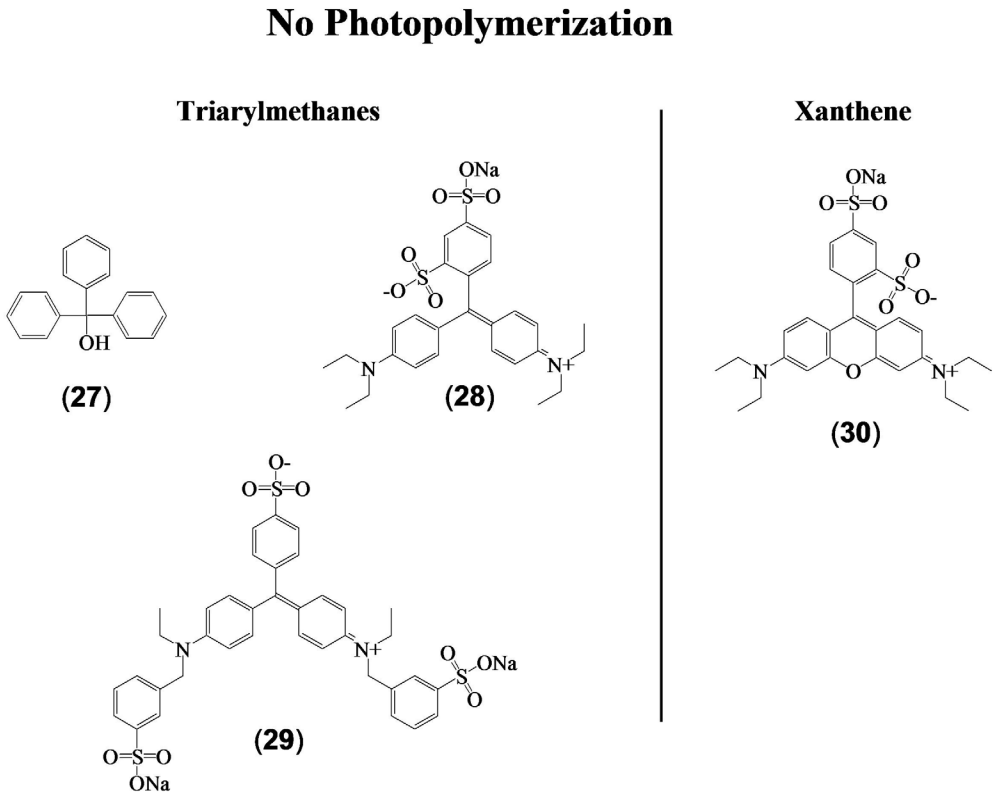

Figure 3.8. Summary of photoinitiator study where triarylmethane dyes and their analogues were tested for a PROVE dependence. Dyes are organized by fabrication trend and dye types.

It should be noted that many of these dyes are often used commercially due to their thermochromic nature.[12-14] For these dyes, the application of heat drives the equilibrium from the cationic, colored form to the neutral, colorless configuration. Under the fabrication conditions used here, heat emanating from the microscope illumination source is sufficient to induce this transition, causing the fabrication trend to shift from a PROVE dependence to a conventional velocity dependence. This phenomenon is shown in Figures 3.9c,d for a resist containing crystal violet (**9**) as the photoinitiator. Turning off the illumination source for a period of time results in a marginal return of PROVE dependence, indicating some degree of reversibility (Figures 3.9e,f).

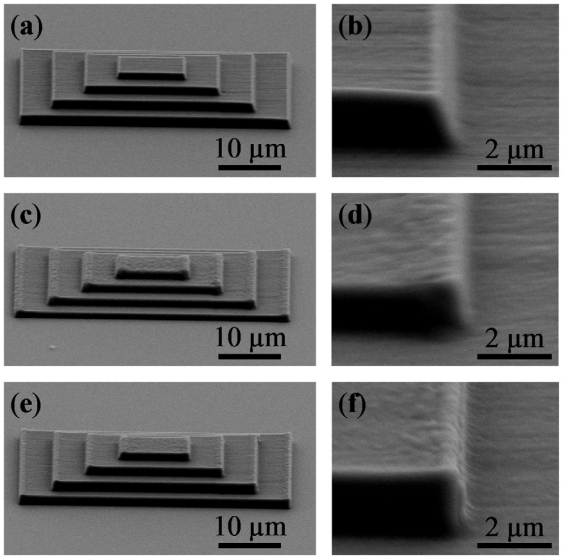

Figure 3.9. Pyramids fabricated with crystal violet as photoinitiator demonstrating thermochromic effect on polymerization. SEM images (tilted at 60°) of (a,b) initial fabrication, (c,d) after 45 min of light exposure, and (e,f) after 30 min of no light exposure. Transition of fabrication trend shows some reversibility.

3.3.3 Mechanism and Kinetic Modeling

In the original report of RAPID photolithography using MGCB as the photoinitiator, two-photon excitation was accomplished using ultrafast pulses with a wavelength of 800 nm and deactivation was performed with a CW laser tuned to the same wavelength.[3] It was proposed that some time after two-photon excitation, the photoinitiator is driven into an intermediate state (which we will call the active species) that initiates polymerization only on a relatively long timescale and can revert back to MGCB upon absorption of another 800 nm photon. Based on this model, the deactivation process could be driven by the ultrafast activation pulses themselves. Because two-photon excitation and one-photon deactivation can be driven at the same wavelength, these two processes will compete with one another even in the absence of a deactivation beam. A key prediction of this model is that if light at the wavelength needed for single-

photon excitation does not lead to efficient deactivation, then a conventional velocity dependence should be observed. In agreement with this prediction, for excitation with CW light at a wavelength of 405 nm, the width of lines decreases with increasing fabrication velocity, as shown in Figure 3.10.

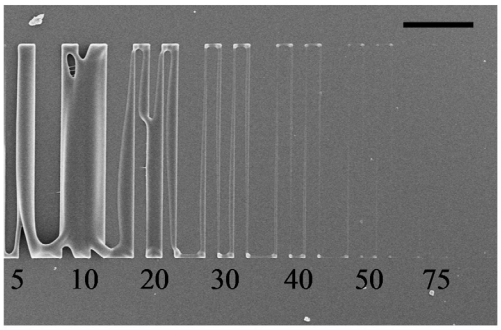

Figure 3.10. Single-photon absorption polymerization of MGC·HCl showing a conventional velocity dependence. The scale bar is 10 μm.

If deactivation is more efficient than excitation, then fabrication would not be expected to occur if the laser focus is held in a fixed position in the sample (as is observed here experimentally). However, there is a relatively long induction time between excitation and polymerization in RAPID photoinitiators.[3] As a result of this long induction time, at finite velocity the focal region of the beam can move away from photoinitiators that have been excited to the intermediate state before deactivation occurs. In this situation, a higher fabrication velocity will lead to a larger concentration of excited photoinitiator molecules being left behind as the focal point moves, causing a PROVE dependence for the transverse feature size. The PROVE dependence is therefore a hallmark of highly efficient deactivation.

In fact, the existence of a PROVE dependence for some RAPID photoinitiators constitutes conclusive proof for the existence of an intermediate state in the

photoinitiation mechanism. Because there is no polymerization if the beam is held in a constant position with a PROVE photoinitiator, we can conclude that the concentration of radicals (and therefore the concentration of the active species) is below the threshold for polymerization. An essential requirement for the observation of a PROVE dependence is therefore that the concentration of the active species must increase after the light is turned off or the focal spot moves away from a region.

In a conventional radical photoinitiator, the active species is either generated directly by photoexcitation or relatively rapidly following photoexcitation.[15] A kinetic scheme for the former case that incorporates deactivation is shown in Figure 3.11. In this scheme the active species (A) is created directly by two-photon absorption of the photoinitiator (PI) and can be deactivated by a single-photon process. Within this scheme, the concentration of species A can only decrease after the light is turned off, so this type of kinetic mechanism is not consistent with a PROVE dependence. The same argument holds true for any mechanism in which the same state that is excited is also deactivated by light, even when the state that is excited can convert to the active state either directly or through intermediate steps.

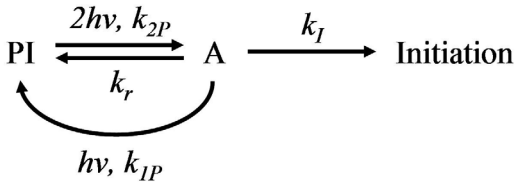

Figure 3.11. In a system with direct deactivation of the state that is excited, the photoinitiator (PI) is excited with effective rate constant, $k_{2P} I^2$ (where I is the intensity). Deactivation occurs with effective rate constant $k_{1P} I$. State A relaxes to PI with rate constant k_r and initiates polymerization with rate constant k_I.

Based on the above argument, a necessary condition for PROVE behavior is that the state that can be deactivated by light is not the state that is excited initially. A minimal

kinetic model that embodies this principle is shown in Figure 3.12. In this scheme, the photoinitiator is first excited to state PI*. Some time later, PI* converts to the active state A, which can be deactivated with light. It can be shown rigorously that if the light is present for long enough that the concentrations of PI* and A reach a pseudo-steady state, then the concentration of A must grow when the light is turned off. The same argument holds if there are intermediate states between PI* and A or if there are states between A and the state that initiates polymerization.

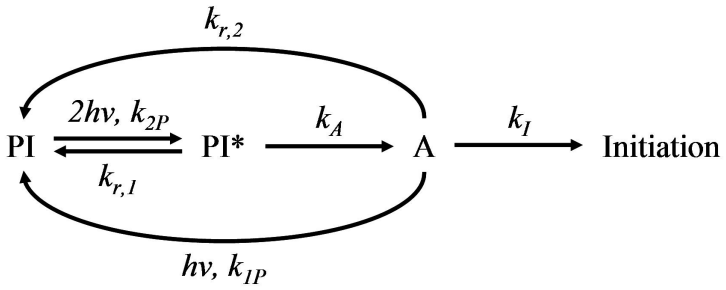

Figure 3.12. Kinetic model for excitation and deactivation of intermediate. For RAPID photoinitiators of types studied here, PI is excited to state PI* and can relax with rate constant $k_{r,1}$. PI* converts to A with rate constant k_A. Species A can be deactivated by light or can relax to PI with rate constant $k_{r,2}$.

Although the concentration of species A is guaranteed to grow after the light is turned off, the magnitude of this increase depends on the rate constants, concentrations and intensities involved. In Figure 3.13a, this process is modeled for different values of the ratio of the deactivation rate constant to the excitation rate constant. The light was turned on at time t = 0 in the simulation and turned off at time t = 600 units. For $\rho = 1\times10^8$, the concentration of species A increases by an order of magnitude when the light is turned off. As ρ becomes smaller, the pseudo-steady state concentration of A grows, and the corresponding growth in this concentration when the light is turned off decreases.

It is clear from this simulation that higher values of ρ make a photoinitiator more likely to exhibit PROVE behavior.

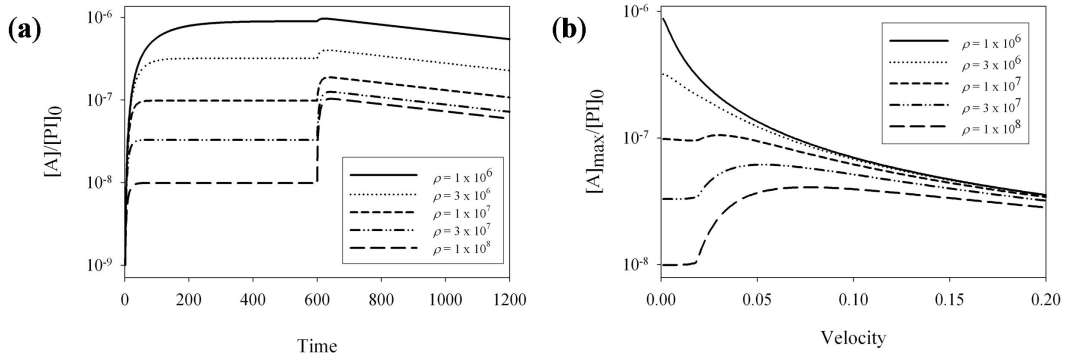

Figure 3.13. (a) Simulation where light is turned on at t = 0 and off at t = 600; $\rho = k_{1P} I/k_{2P} I^2$. (b) Simulation where a spatial Gaussian light beam passes over a point in space and $[A]_{max}$ is determined as a function of velocity. (Simulation constants were $I = 10^{-4}$, $k_{2P} = 1$, $k_A = 0.1$, $k_{r,1} = 0.001$, $k_{r,2} = 0.001$, $k_1 = 10^{-5}$, FHWM = 5 to 1000.)

A one-dimensional simulation was also performed of the concentration of A when a Gaussian laser beam moves over a fixed point in space. Representative results from this simulation are shown in Figure 3.13b, in which the maximum concentration of A is plotted as a function of velocity. For smaller values of (corresponding to weaker deactivation), the maximum concentration of A is large at the lowest velocities and decreases with increasing velocity. This case corresponds to conventional photoinitiation. However, when deactivation is more efficient (larger values of), the maximum concentration of A increases with velocity before reaching a maximum and then decreasing. This situation corresponds to initiators that display PROVE behavior.

Although the kinetic arguments presented above guarantee the existence of an intermediate state, the structure of this state has yet to be determined. The photochemistry and photophysics of triarylmethane dyes such as MGCB and MGC·HCl and related diarylmethane and rhodamine dyes are highly complex, and depend sensitively on

environment.[16] As a result of this complexity, despite extensive study there exists little consensus on the mechanisms of most photochemical and photophysical processes supported by these dyes. Nevertheless, previous work provides important clues regarding the mechanism of initiation and deactivation of these species.

The observation that virtually every cationic species investigated in these classes exhibits PROVE behavior suggests PROVE is a quite general phenomenon. In the case of cationic triarylmethane dyes, it has been suggested previously that excitation leads to intersystem crossing followed by generation of a solvated electron.[17] Furthermore, it has been proposed that recombination of the radical dication with the solvated electron can regenerate the dye.[17] A similar process was previously proposed for MGCB in RAPID lithography: photoexcitation generates a pair of weakly reactive radicals by means of electron transfer and the parent molecule can be regenerated by photo-induced back transfer.[3] When the parent species is cationic, this back transfer would be expected to be especially efficient, leading to PROVE behavior for cationic dyes in the classes studied here. It is propose therefore that the mechanism shown in Figure 3.14 leads to a PROVE dependence for MGC·HCl and other cationic triarylmethanes. After photoexcitation to an excited singlet state, the photoinitiator undergoes intersystem crossing to a triplet state. The triplet molecule can then convert to a solvated electron and a radical dication, either of which may initiate polymerization on a relatively long timescale. Absorption of another 800 nm photon can drive recombination of the electron and the dication, regenerating the photoinitiator. The dication and solvated electron would be expected to be closely associated, but if they diffuse apart then photodeactivation will no longer be

possible, accounting for the second, non-deactivatable polymerization channel that we have observed previously.[3]

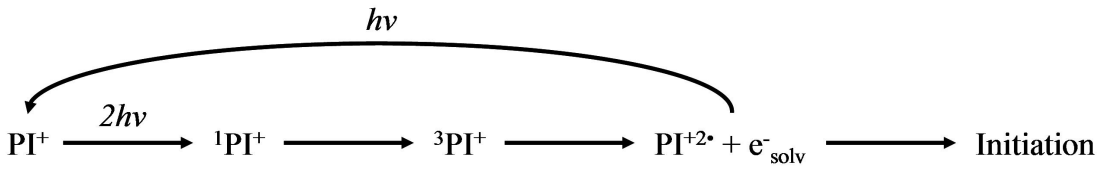

Figure 3.14. A cationic triarylmethane photoinitiator is excited and then crosses to a triplet state. The triplet can convert into a radical dication plus a solvated electron, either of which can initiate polymerization. Absorption drives the dication/electron pair back to the parent molecule.

3.3.4 Tuning Velocity Dependence

It is also possible to tailor the velocity dependence of fabrication by using mixtures of photoinitiators. For instance, if a photoinitiator that has a conventional velocity dependence is combined with one that has a PROVE dependence, then the transverse line width of the fabricated line should be independent of velocity when appropriate proportions of these two photoinitiators are mixed together. Experiments at different proportions of MGC·HCl to MGCB indicate that as the fraction of MGCB is increased, behavior transitions from a PROVE dependence to a conventional velocity dependence. For 2 wt% of total photoinitiator, a 2:1 mixture of MGC·HCl to MGCB was found to lead to a line width that is nearly independent of velocity over a broad range of velocities (Figure 3.15b). Shown in Figure 3.15a are lines created at different velocities with this mixture. It was found that by changing the ratio of these two photoinitiators, the velocity dependence of fabrication can be tuned to any point between the behaviors observed for the individual photoinitiators.

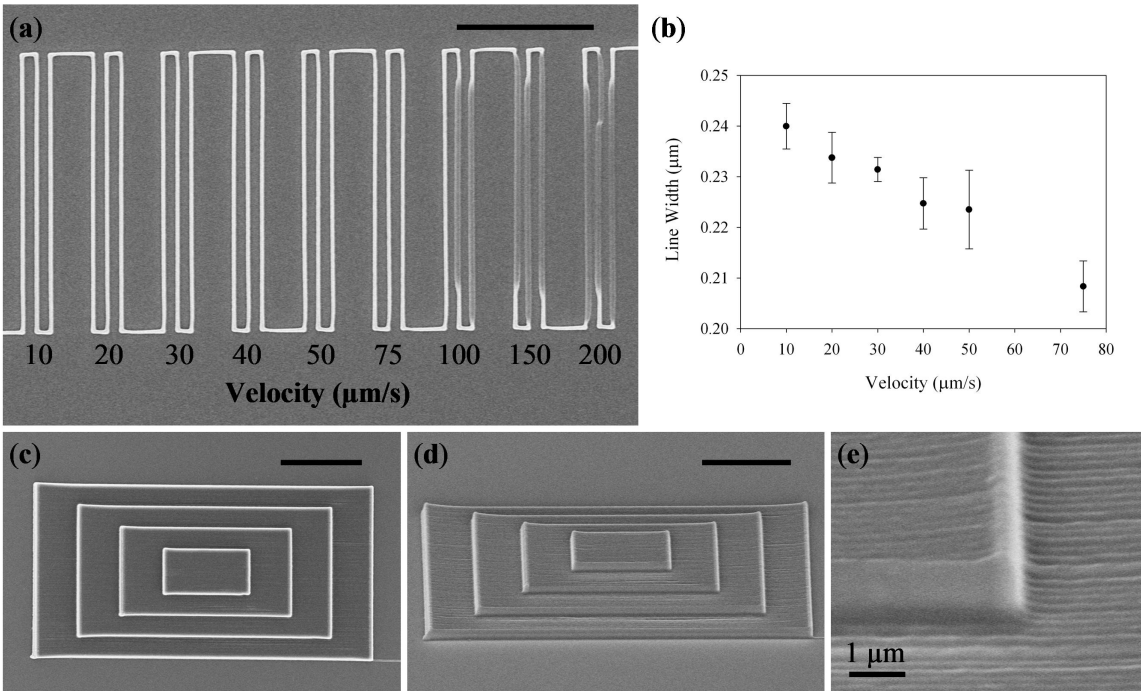

Figure 3.15. Fabrication with 2:1 wt% mix of MGCB and MGC·HCl. Lines fabricated at different velocities in acrylic photoresist (a) with corresponding transverse resolution as a function of fabrication velocity (b). Error bars represent ±1 standard deviation. Top (c) and 45° tilt (d) views of pyramid and turn points (e) created with MAP. Successive levels of the pyramid (from bottom to top) were created with velocities of 100, 75, 50, and 25 µm/s. All scale bars are 10 µm unless overwise noted.

Figures 3.15e-c show images of a pyramid created with the MGC·HCl/MGCB mixture as the photoinitiator. Despite the fact that the transverse feature size is independent of velocity over the range of velocities used to create this pyramid, ridges are observed at all of the turning points of the structure. This phenomenon arises because the dependence of the axial feature size on fabrication velocity is different from that of the transverse feature size. This difference in the velocity dependence of features in the transverse and axial directions is a direct result of the geometry of the laser beam in the focal region, where fabrication occurs.

The velocity dependence of the photoinitiator has a dramatic effect on the ability to control fabrication. To demonstrate the importance of the velocity dependence, two-

dimensional sinusoidal patterns were created using different photoinitiators (Figure 3.16). In each case, the stage moved with a constant velocity in the X-direction (horizontal in the images) and with a sinusoidal velocity in the Y-direction (vertical in the images). The velocity at the turning points of the sine wave is considerably lower than that in the linear regions. When MGCB is used as the initiator the line is notably thicker at the turning points than in the remainder of the sine wave (Figure 3.16a,b). Conversely, when MGC·HCl is used, the line becomes significantly thinner at the turning points (Figure 3.16c,d). Finally, with the 2:1 MGC·HCl/MGCB mixture, the line is of constant thickness throughout the sine wave (Figure 3.16e,f). Thus, with the velocity-independent initiator, structures with a constant transverse feature size can be created without the need to design a fabrication path that has equal point spacing.

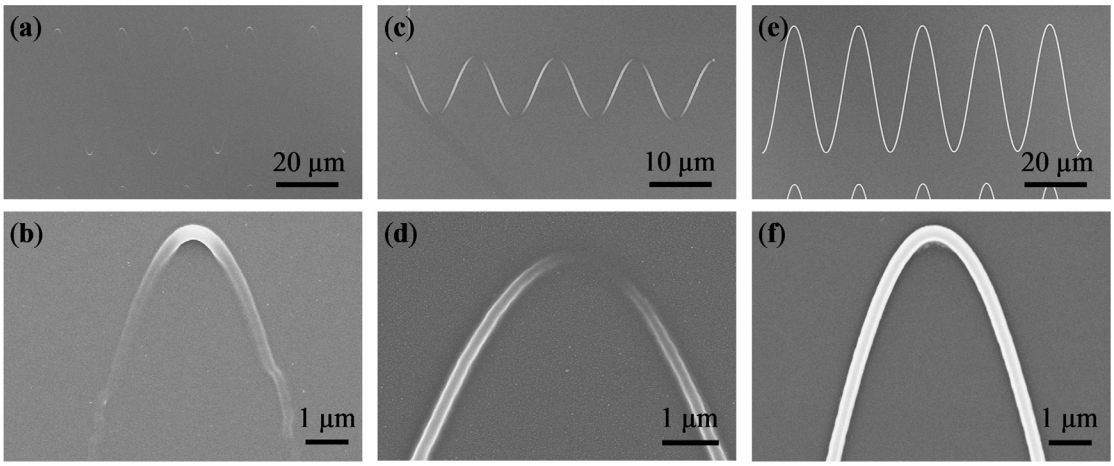

Figure 3.16. Fabrication of sinusoidal acrylic structures with nonuniform velocities. With MGCB as the initiator the lines are thickest at the turning points where the velocity is the smallest (a and b). With MGC·HCl as the initiator, the lines are thinnest at the turning points (c and d). With a 2:1 MGC·HCl/MGCB mixture, the lines are of uniform width (e and f).

Velocity independence and multiple other observations of the behavior of MGCB and MGC·HCl would indicate that, in the acrylic resin, an equilibrium exists between the neutral and cationic forms of the dyes. Therefore, changing the ratio of neutral (MGC) to

cationic (MGC·HCl) should result in fabrication that can be tuned from conventional behavior to PROVE-like behavior. It is also possible that a small amount of the salt form of malachite green probably exists in the MGCB photoresist producing the green color. The environmental factors in which the dyes are placed in, including pH, temperature and solvent can all affect this equilibrium.[16]

To test the contents of dyes directly as purchased, UV-visible spectroscopy was performed. Previous studies[18,19] have shown that for malachite green, at a pH greater than 12, only the neutral species are present and the solution is colorless. Altering the pH to less than 4 turns the solution a greenish-blue color as the molecules are all present in the cationic form. Figure 3.17a shows this absorbance change as a result of decreasing pH with the evolution of peaks at 425 and 621 nm at pH ~ 1. Both as-purchased samples of MGCB and MGC·HCl, dissolved in ethanol showed these peaks at ~425 and ~621 nm (Figure 3.17b).

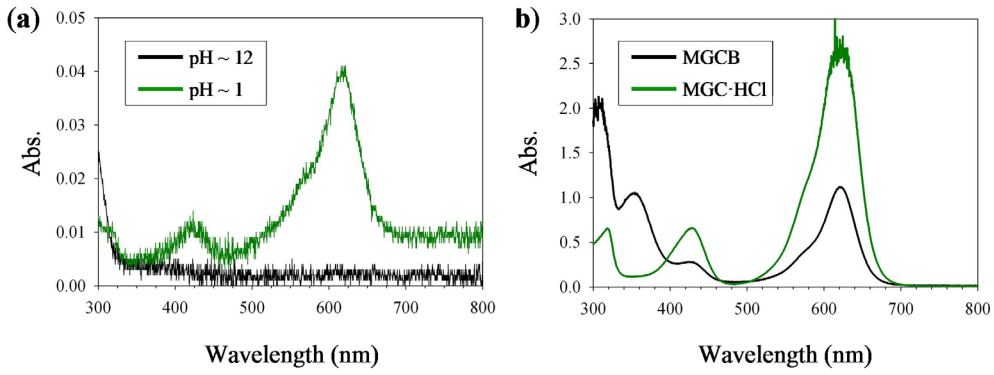

Figure 1.17. (a) UV-Visible absorption spectra for MGCB, ~1.5 µM in water, indicating dependence on pH. At higher pH (>12) the solution is colorless and in the neutral configuration; at lower pH (< 4) the solution is greenish-blue and in the cationic configuration. (b) Spectra for MGCB and MGC·HCl samples, in ethanol, directly from vendor.

The existence of impurities[9] in each dye could explain why MGCB may have some cationic species as indicated by the presence of color when dissolved in the resin.

For these experiments, MGCB was used without further purification as sold by the vendor (Sigma-Aldrich) and has 90% dye content. To test for the presence of halides as an impurity, an excess amount of MGCB was dissolved in water (in which it is weakly soluble) in a test tube. The mixture was centrifuged and the transparent, green supernatant was transferred to another test tube. Silver nitrate was then added to the solution. A white precipitate formed indicating the formation of an insoluble silver compound that results from a contaminant in the original MGCB sample.

3.4 Conclusions

It has been discovered that a broad class of common dye molecules can be used as photoinitiators for RAPID lithography and that these initiators exhibit extremely efficient deactivation. As a result of this efficient deactivation, when used for MAP these photoinitiators can create features with a transverse width that is proportional to the fabrication velocity, rather than inversely proportional (as is the case for conventional radical photoinitiators). Furthermore, by combining a PROVE initiator and an initiator with a conventional velocity dependence in appropriate proportions, it is possible to create a photoresist for which the transverse line width in MAP fabrication is independent of the fabrication velocity over a substantial range velocities.

PROVE behavior appears to be a nearly universal feature of cationic triarylmethane, diarylmethane and rhodamine dyes, providing broad opportunities for tuning the properties of these molecules for optimization of lithographic processes. As a result, PROVE initiators will provide important new capabilities for lithography using negative-tone photoresists. The exceptional deactivation efficiencies of PROVE initiators

such as MGC·HCl will allow RAPID lithography to be performed at considerably lower deactivation powers and over larger areas than has been possible previously. These initiators should further enable the implementation of large-area RAPID lithography using single-photon excitation. Additionally, the use of velocity-independent initiator combinations for MAP will enable fabrication with even higher precision than is available currently.

References:

(1) Stocker, M. P.; Li, L. J.; Gattass, R. R.; Fourkas, J. T., Multiphoton photoresists giving nanoscale resolution that is inversely dependent on exposure time. *Nature Chemistry* **2011,** 3, (3), 223-227.

(2) Fourkas, J. T., Nanoscale Photolithography with Visible Light. *Journal of Physical Chemistry Letters* **2010,** 1, (8), 1221-1227.

(3) Li, L.; Gattass, R. R.; Gershgoren, E.; Hwang, H.; Fourkas, J. T., Achieving lambda/20 Resolution by One-Color Initiation and Deactivation of Polymerization. *Science* **2009,** 324, (5929), 910-913.

(4) LaFratta, C. N.; Fourkas, J. T.; Baldacchini, T.; Farrer, R. A., Multiphoton fabrication. *Angewandte Chemie-International Edition* **2007,** 46, (33), 6238-6258.

(5) Maruo, S.; Fourkas, J. T., Recent progress in multiphoton microfabrication. *Laser & Photonics Reviews* **2008,** 2, (1-2), 100-111.

(6) Yang, D.; Jhaveri, S. J.; Ober, C. K., Three-dimensional microfabrication by two-photon lithography. *MRS Bulletin* **2005,** 30, (12), 976-982.

(7) Klar, T. A.; Jakobs, S.; Dyba, M.; Egner, A.; Hell, S. W., Fluorescence microscopy with diffraction resolution barrier broken by stimulated emission. *Proceedings of the National Academy of Sciences of the United States of America* **2000,** 97, (15), 8206-8210.

(8) Baldacchini, T.; LaFratta, C. N.; Farrer, R. A.; Teich, M. C.; Saleh, B. E. A.; Naughton, M. J.; Fourkas, J. T., Acrylic-based resin with favorable properties for three-dimensional two-photon polymerization. *Journal of Applied Physics* **2004,** 95, (11), 6072-6076.

(9) Lillie, R. D.; Conn, H. J.; Biological Stain, C., *H. J. Conn's Biological stains: a handbook on the nature and uses of the dyes employed in the biological laboratory*. 9 ed.; Williams & Wilkins: Baltimore, 1977; p 692.

(10) Gurr, E., *Synthetic Dyes in Biology, Medicine and Chemistry*. Academic Press Inc.: New York, 1971; p 807.

(11) Campagnola, P. J.; Delguidice, D. M.; Epling, G. A.; Hoffacker, K. D.; Howell, A. R.; Pitts, J. D.; Goodman, S. L., 3-dimensional submicron polymerization of acrylamide by multiphoton excitation of xanthene dyes. *Macromolecules* **2000,** 33, (5), 1511-1513.

(12) Burkinshaw, S. M.; Griffiths, J.; Towns, A. D., Reversibly thermochromic systems based on pH-sensitive spirolactone-derived functional dyes. *Journal of Materials Chemistry* **1998,** 8, (12), 2677-2683.

(13) Gessner, T.; Mayer, U., Triarylmethane and Diarylmethane Dyes. In *Ullmann's Encyclopedia of Industrial Chemistry*, Wiley-VCH Verlag GmbH & Co. KGaA: 2000.

(14) Rosenthal, I.; Peretz, P.; Muszkat, K. A., Thermochromic and Hyperchromic Effects in Rhodamine-B Solutions. *Journal of Physical Chemistry* **1979,** 83, (3), 350-353.

(15) Colley, C. S.; Grills, D. C.; Besley, N. A.; Jockusch, S.; Matousek, P.; Parker, A. W.; Towrie, M.; Turro, N. J.; Gill, P. M. W.; George, M. W., Probing the reactivity of photoinitiators for free radical polymerization: Time-resolved infrared spectroscopic study of benzoyl radicals. *Journal of the American Chemical Society* **2002,** 124, (50), 14952-14958.

(16) Duxbury, D. F., The Photochemistry and Photophysics of Triphenylmethane Dyes in Solid and Liquid-Media. *Chemical Reviews* **1993,** 93, (1), 381-433.

(17) Bangert, R.; Aichele, W.; Schollmeyer, E.; Weimann, B.; Herlinger, H., Photooxidation of Malachite Green and Crystal Violet. *Melliand Textilberichte International Textile Reports* **1977,** 58, (5), 399-404.

(18) Fischer, A. R.; Werner, P.; Goss, K. U., Photodegradation of malachite green and malachite green carbinol under irradiation with different wavelength ranges. *Chemosphere* **2011,** 82, (2), 210-214.

(19) Reisfeld, R.; Chernyak, V.; Jorgensen, C. K., Photophysical Behavior of Malachite Green in Solid and Liquid-Media. *Chimia* **1992,** 46, (4), 148-151.

Chapter 4: Kinetic Simulations of Deactivation

4.1 Introduction

For multiphoton absorption polymerization (MAP) to be an efficient method for the fabrication of micro- and nanoscale devices, the trends associated with polymerization must be understood and, if possible, tuned to match the application. The effects of velocity and exposure time on feature sizes are two of those important trends. For example, when using a serial mechanism for motion, frequent changes in velocity occur, especially at turning points where there is necessarily a deceleration followed by an acceleration. The primary phenomenon that needs to be studied is when changing velocity the duration of an exposure at single point along the line. Experiments were designed to observe and measure quantitatively how the exposure duration affects polymerization.

The second goal of these studies was to understand how exposure duration affects feature size for photoinitiators that show a proportional velocity (PROVE) dependence versus conventional photoinitiators. It was theorized[1] that if a photoinitiator was capable of deactivation through the addition of another single photon, either from the excitation source (self-deactivation) or from a second laser beam (resolution augmentation through photo-induced deactivation, RAPID), then it should have an associated self-deactivation efficiency, ρ:

$$\rho = \frac{k_{1P} I}{k_{2P} I^2}, \tag{4.1}$$

where k_{1P} is the rate of the single-photon deactivation process, k_{2P} is the rate of two-photon absorption and I is the intensity of light. According to this equation, for a conventional photoinitiator that can be used for RAPID, ρ should be small. For a PROVE photoinitiator, ρ should be large. If the value for ρ could be determined for a photoresist, then deactivation could be more efficiently performed depending on the application.

The first type of experiment performed was a velocity dependence study in which a laser with a Gaussian spatial intensity distribution was used to create lines by single passes at different velocities. When the velocity increases, the exposure time at each point decreases. As a parallel to the velocity study, the dependence of feature size on the duration of a single exposure at a single location was also studied. Single exposures correlate to velocity in that if a single exposure of 0.1 s is performed using a laser with a beam diameter of 0.5 μm, it would be analogous to creating a line at a velocity of 5 μm/s. Accordingly, reducing the exposure time to 0.001 s corresponds to a velocity of 500 μm/s. The concept of this study closely resembles voxel studies previous used to measure feature sizes.[2,3]

The single-exposure experiments can also be correlated to the understanding of how self-deactivation occurs. Previous experiments on PROVE photoinitiators showed that a single exposure at a single point can induce polymerization. This observation implies that self-deactivation cannot inhibit polymerization completely. Thus, it was theorized that with efficient self-deactivation the polymerized feature size should remain relatively constant as long as the exposure time is long enough to both excite and then

deactivate the photoinitiator. However, when the light source is turned off and the deactivation pathway is eliminated the size of the feature should increase (Figure 4.1).[1] However, at some shorter exposure time, the duration should be sufficient for excitation to occur but too short for the absorption of an additional photon to induce deactivation. In this situation, even shorter exposures would result in decreasing feature sizes. The latter of the two proposed results should be the same as for a photoinitiator that does not exhibit self-deactivation, for which decreasing the exposure time decreases the feature size.

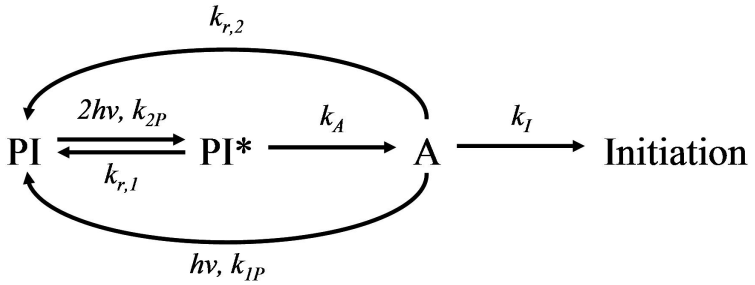

Figure 4.1. Kinetic model for deactivation. Two-photon absorption excites photoinitiator, PI, to PI* followed by a transition to the active intermediate state, A. A can lead to initiation of polymerization or undergo deactivation via a single-photon process or relaxation to return to the ground state.

An additional experiment was designed to determine the cumulative effect of multiple exposures on feature sizes. In this experiment, the varying number of exposures still ultimately produces the same cumulative exposure time. The cumulative exposure time is divided into shorter exposures, each being repeated after a defined delay. The delay between exposures is set to allow for some relaxation of excited molecules. For PROVE photoinitiators, at some exposure time, deactivation will not have had time to occur before the light source is turned off, resulting in some polymerization. The hypothesis was therefore that a multitude of short exposures should result in a final feature size that is larger than a single, longer exposure, even if the total exposure time

remained the same. For conventional photoinitiators, in which self-deactivation is negligible, the short exposures would not produce enough radicals for widespread polymerization. Multiple exposures should therefore result in a final feature size smaller than that for a single exposure of the same total duration.

One of the criteria in the design of the experiments described above was that they could be simulated using the kinetic model that was developed for RAPID and was later applied to describe self-deactivation (Figure 4.1). The preliminary kinetic parameters used in Chapter 3 produced qualitative simulations. Therefore, the kinetic parameters were modified and more detailed results incorporated so that the experimental results could be simulated more accurately. The kinetic parameters could then provide information on the timescales of each step as well as establishing a value for ρ.

However, before performing simulations, some considerations had to be applied to the kinetic model based on prior observations. First, a new intermediate species, A′, was created to track the concentration of active intermediates that would only result in initiation of polymerization. This scheme provides a more accurate account of how much initiation of polymerization occurs. Second, it was observed in the original RAPID experiments that at a given power, it no longer was possible to deactivate the photoinitiator molecule, regardless of the deactivation power.[4] To account for this phenomenon, a branching pathway was applied to the kinetic model, in which two paths now lead away from the active intermediate A toward the new intermediate, A′. These pathways have different reaction rates, one to account for a slower process in which deactivation is more likely to occur and limit it effectiveness, and another to account for a faster process in which deactivation was less likely to have an effect. This faster step

provides the non-deactivatable pathway towards initiation. The final proposed kinetic model is shown in Figure 4.2.

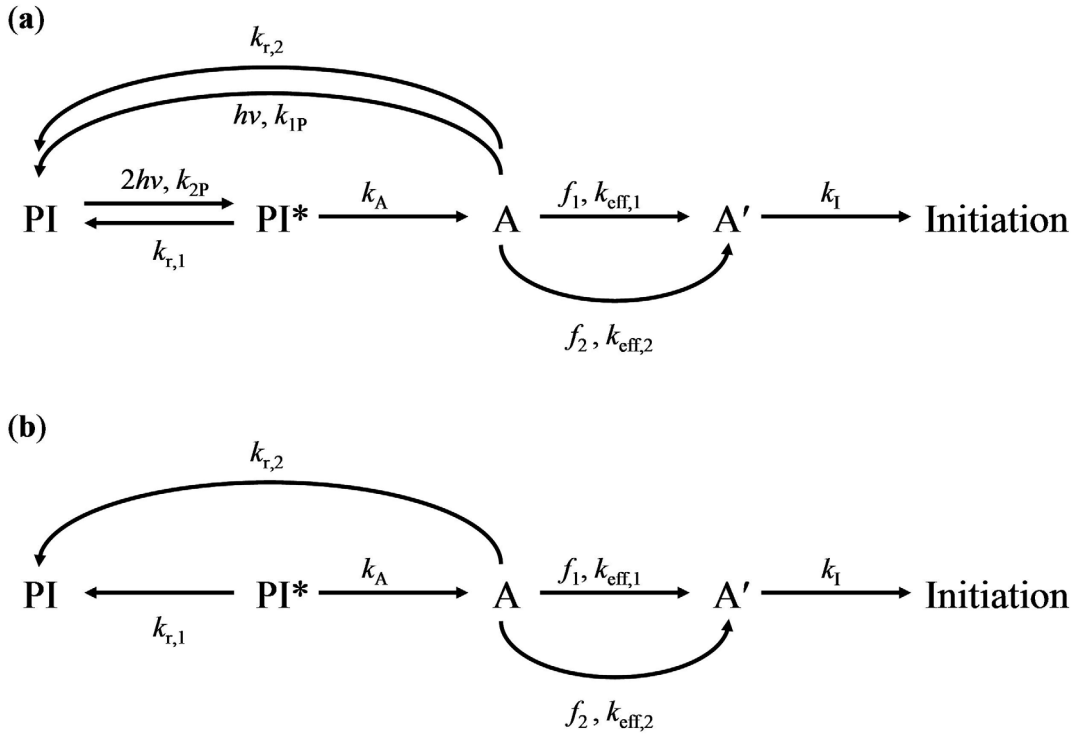

Figure 4.2. Kinetic model for deactivation with the light source on (a) and off (b). Changes are tracked via a new intermediate state, A′, that is capable of only initializing polymerization. A branching pathway leads from A to A′ to account for a slow ($k_{eff,1}$) process and fast ($k_{eff,2}$) process that prevents complete deactivation.

The kinetic equations are set up as follows:

$$\frac{d[\mathrm{PI}]}{dt} = k_{r,1}[\mathrm{PI^*}] + (k_{r,2} + k_{1P}I)[\mathrm{A}] - k_{2P}I^2[\mathrm{PI}] \tag{4.2}$$

$$\frac{d[\mathrm{PI^*}]}{dt} = k_{2P}I^2[\mathrm{PI}] - (k_{r,1} + k_A)[\mathrm{PI^*}] \tag{4.3}$$

$$\frac{d[\mathrm{A}]}{dt} = k_A[\mathrm{PI^*}] - (k_{r,2} + k_{1P}I + f_1k_{eff,1} + f_2k_{eff,2})[\mathrm{A}] \tag{4.4}$$

$$\frac{d[\mathrm{A'}]}{dt} = (f_1k_{eff,1} + f_2k_{eff,2})[\mathrm{A}] - k_I[\mathrm{A'}] \tag{4.5}$$

When the light source is turned off, as shown in Figure 4.2, $I \rightarrow 0$ and the equations become:

$$\frac{d[\mathrm{PI}]}{dt} = k_{\mathrm{r},1}[\mathrm{PI}^*] + (k_{\mathrm{r},2})[\mathrm{A}] \tag{4.6}$$

$$\frac{d[\mathrm{PI}^*]}{dt} = -(k_{\mathrm{r},1} + k_{\mathrm{A}})[\mathrm{PI}^*] \tag{4.7}$$

$$\frac{d[\mathrm{A}]}{dt} = k_{\mathrm{A}}[\mathrm{PI}^*] - (k_{\mathrm{r},2} + f_1 k_{\mathrm{eff},1} + f_2 k_{\mathrm{eff},2})[\mathrm{A}] \tag{4.8}$$

$$\frac{d[\mathrm{A}']}{dt} = (f_1 k_{\mathrm{eff},1} + f_2 k_{\mathrm{eff},2})[\mathrm{A}] - k_{\mathrm{I}}[\mathrm{A}'] \tag{4.9}$$

With a series of experiments and the capability to simulate the results, the goal was to develop a better overall understanding of deactivation. With this knowledge, it should be possible to tailor photoinitiator systems to specific applications. Velocity-independent resins could be formulated for any range of velocities. RAPID could be used to produce features below λ/20 by using the rate parameters to select a photoinitiator that behaves in a manner that fits the desired results. With those end goals in mind, the results of these studies are presented here.

4.2 Materials and Methods

The photoinitiators used here include two with a conventional velocity dependence, malachite green carbinol base (MGCB, **1**; Figure 4.3) and rhodamine B base (RhBB, **2**; Figure 4.3) and two with a PROVE dependence, malachite green carbinol hydrochloride (MGC·HCl, **3**; Figure 4.3) and rhodamine 6G (Rh6G, **4**; Figure 4.3). Concentrations of the photoinitiators were set at 2 wt% in the acrylic monomer. When

using MGCB and MGC·HCl, a long-pass filter that eliminates wavelengths shorter than 500 nm was used to prevent undesired polymerization from the white-light illumination source. When RhBB and Rh6G were used, a long-pass filter eliminating wavelengths shorter than 600 nm was used for the same reason.

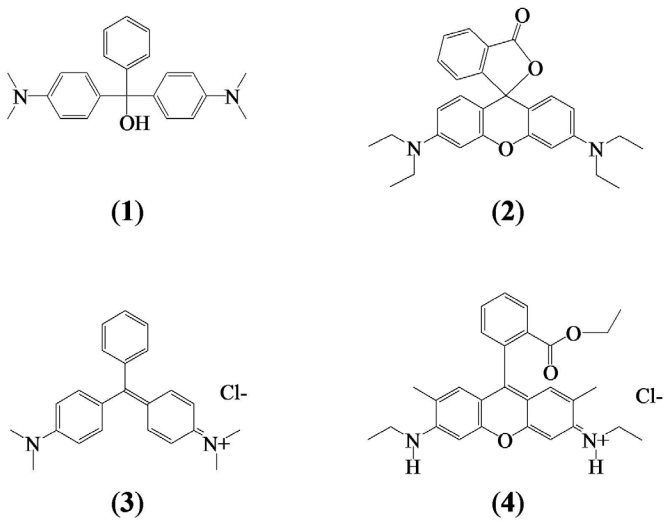

Figure 4.3. Photoinitiator molecules used for the velocity and exposure studies: (1) MGCB, (2) RhBB, (3) MGC·HCl, and (4) Rh6G. (1) and (2) have a conventional velocity dependence, (3) has a PROVE dependence and (4) exhibits both, depending upon the velocity range.

The single acousto-optic modulator setup (see Section 2.2.5) was used with the fabrication beam. For the initial fabrication and velocity studies, the modulator was set to provide a constant diffracted beam. The intensity of the laser varied according to the photoinitiator being used. However, for each study, the intensity was set so that fabrication occurred at 20 μm/s (for both conventional velocity and PROVE photoinitiators). These parameters led to polymerization without any of the explosions that can result from localized heating of the resin.

Velocity studies were carried out using the piezoelectric nanostage to vary the velocity from 1 to 200 μm/s. Grids were fabricated for exposure studies and the constant diffracted beam was eliminated. The waveform generators were used to control exposure

conditions. For the single-exposure studies, the duration of exposure was set on the computer and consisted of integer divisions of 0.1 s. For example, exposures would be lengths of 0.1 s (0.1 s divided by 1), 0.05 s (0.1 s divided by 2), and so forth down to 0.001 s (0.1 s divided by 100). Experiments at each exposure condition were repeated multiple times, separated by 3 μm, at a set Z-position. The Z-position was increased and the exposures repeated. Cumulative exposure studies were set up in the same way, however multiple exposures were carried out at a single location. Each location received the same cumulative exposure of 0.1 s. The duration of each exposure was an integer division of 0.1s. Each exposure was followed by a period of 1.0 s with no exposure. This duration allowed for some relaxation of excited molecules. If the delay is set to a smaller duration, the result is a net increase in the overall population of molecules in the excited state with each exposure. If the delay is too long, relaxation still occurs but the experiments take longer. The cumulative exposure study is shown schematically in Figure 4.4 and consisted of conditions of one exposure of 0.1 s, two exposures of 0.05 s, and so forth up to 100 exposures of 0.001 s. The timing sequences are shown in Table 4.1.

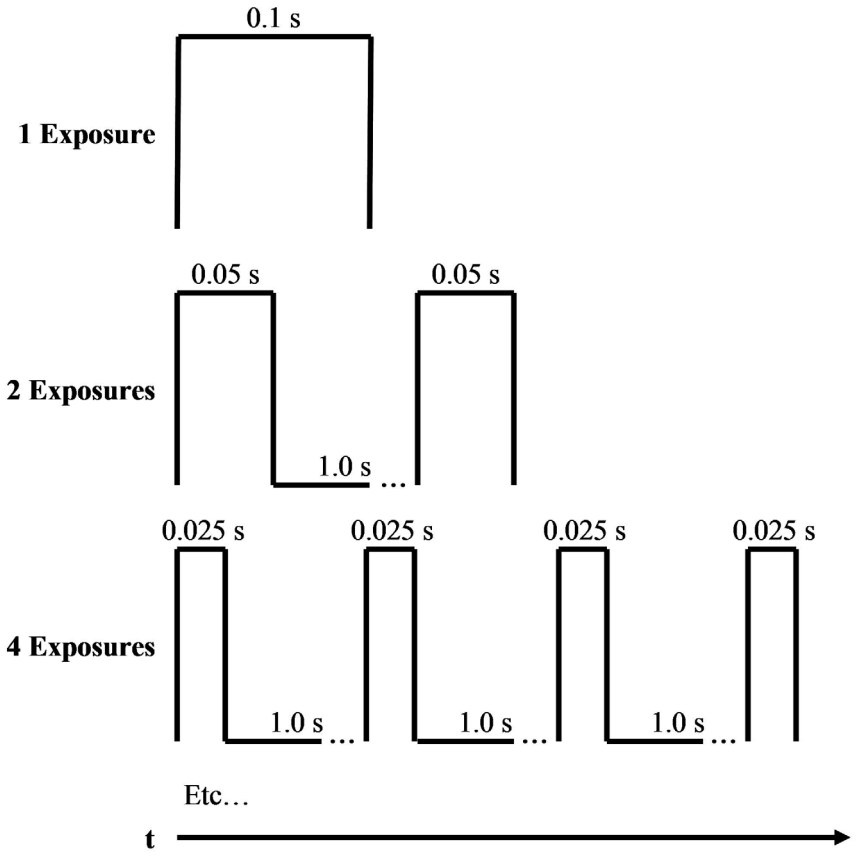

Figure 4.4. Timing sequence example for the cumulative exposure studies. A total exposure of 0.1 s is divided into multiple, smaller exposures to observe exposure trends of conventional and PROVE photoinitiators. (Adapted from ref 5.)

Table 4.1. Exposure conditions for the cumulative exposure study in which the total exposure was 0.1 s.

Exposures (N)		Individual Exposure Duration (s)		Cumulative Exposure Duration (s)
1	×	0.1	→	0.1
2	×	0.05	→	0.1
3	×	0.03333	→	0.1
4	×	0.025	→	0.1
5	×	0.02	→	0.1
8	×	0.0125	→	0.1
10	×	0.01	→	0.1
15	×	0.006667	→	0.1
20	×	0.005	→	0.1
25	×	0.004	→	0.1
30	×	0.003333	→	0.1
40	×	0.0025	→	0.1
50	×	0.002	→	0.1
80	×	0.00125	→	0.1
100	×	0.001	→	0.1

4.3 Results and Discussion

4.3.1 Velocity and Exposure Experiments

Velocity studies with MGCB and MGC·HCl were discussed in Chapter 3 and are shown again in Figures 4.5a and 4.6a, respectively. Results for the feature size dependences on velocity for RhBB and Rh6G are shown in Figures 4.7a and 4.8a, respectively. The transverse feature sizes of standing line was measured. However, it can be seen that for higher velocities, the aspect ratio for the lines (axial to transverse dimension) were large enough to result in a collapsed or fallen line. The axial dimension of the fallen lines was more evident, but due to possible bends in the fallen line, measurements of the axial dimension were not regarded as being accurate. The presence of polymerization at turning points of fabrication is one of the signature differences between initiators with a conventional velocity dependence (MGCB and RhBB) and those with a PROVE dependence (MGC·HCl and Rh6G). The most obvious contrast in fabrication trends can be seen when comparing MGC·HCl to Rh6G. For Rh6G, a peak in feature size is evident at 40 μm/s, indicating that at approximately this velocity, self-deactivation is no longer the dominant force in determining feature size. Instead, the width of the lines decreased with increasing velocity as a result of a reduction in radical formation, much as for a conventional photoinitiator. It stands to reason, then, that a peak feature size exists for MGC·HCl at some velocity that was not tested. However, this peak feature size must occur at a higher velocity, and therefore MGC·HCl should be considered to be more efficient at self-deactivation that Rh6G.

It should be noted that, for each photoinitiator tested, the fabrication trends are relatively consistent regardless of the intensity of the laser source or concentration (1-3

wt%) of photoinitiator. The changes were observed in overall feature size due to these two parameters with the complication of a trade-off between too much localized heating causing explosions at lower velocities and larger feature sizes at higher velocities. Therefore, it was difficult to compare dimensions for two separate samples of the same photoinitiator prepared on different occasions unless all parameters were kept constant, which was difficult due to environmental conditions such as temperature and laser quality.

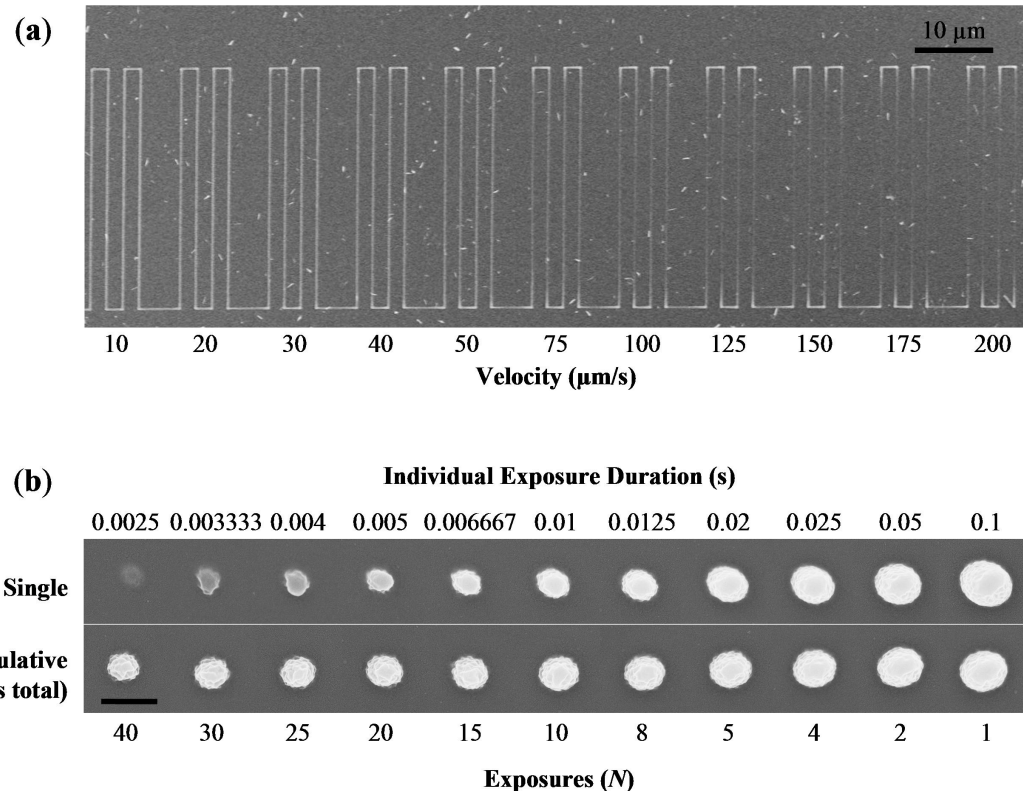

Figure 4.5. Experimental results for a velocity study (a) and exposure studies (b) with MGCB as a MAP photoinitiator. The top line of (b) shows feature sizes resulting from single exposures of the listed duration. The bottom line of (b) shows the feature sizes resulting from multiple exposures when that individual exposure is repeated to a cumulative exposure of 0.1 s. Each SEM image is representative of the measured feature size trend. The scale bar in (b) represents 500 nm. (Adapted from ref 5.)

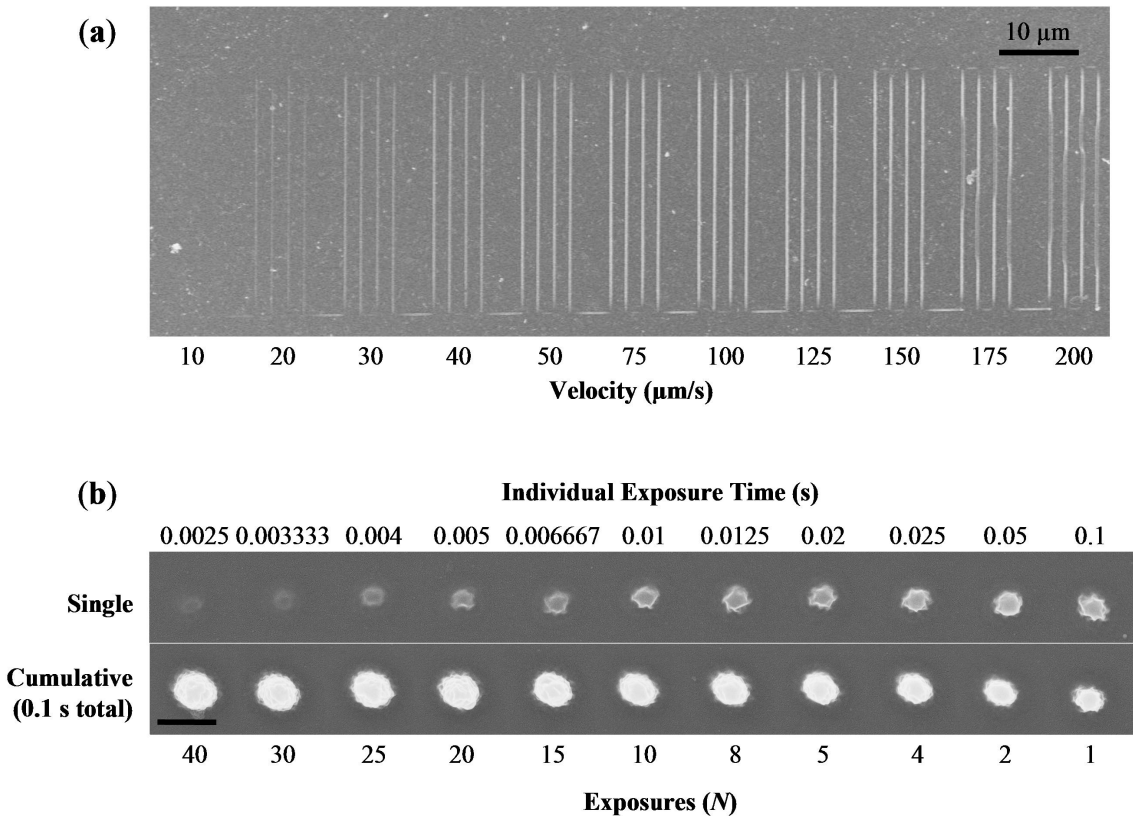

Figure 4.6. Experimental results for a velocity study (a) and exposure studies (b) with MGC·HCl as a MAP photoinitiator. The top line of (b) shows feature sizes resulting from single exposures of the listed duration. The bottom line of (b) shows the feature sizes resulting from multiple exposures when that individual exposure is repeated to a cumulative exposure of 0.1 s. Each SEM image is representative of the measured feature size trend. The scale bar in (b) represents 500 nm. (Adapted from ref 5.)

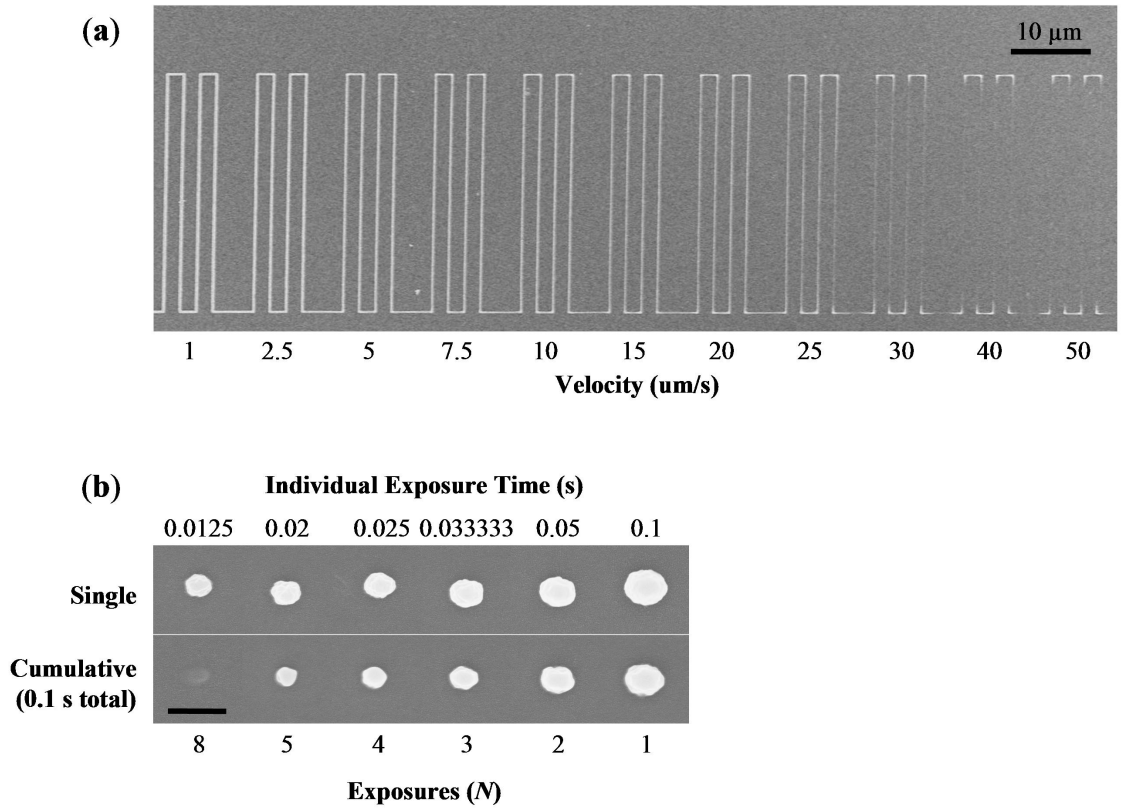

Figure 4.7. Experimental results for a velocity study (a) and exposure studies (b) with RhBB as a MAP photoinitiator. The top line of (b) shows feature sizes resulting from single exposures of the listed duration. The bottom line of (b) shows the feature sizes resulting from multiple exposures when that individual exposure is repeated to a cumulative exposure of 0.1 s. Each SEM image is representative of the measured feature size trend. The scale bar in (b) represents 500 nm.

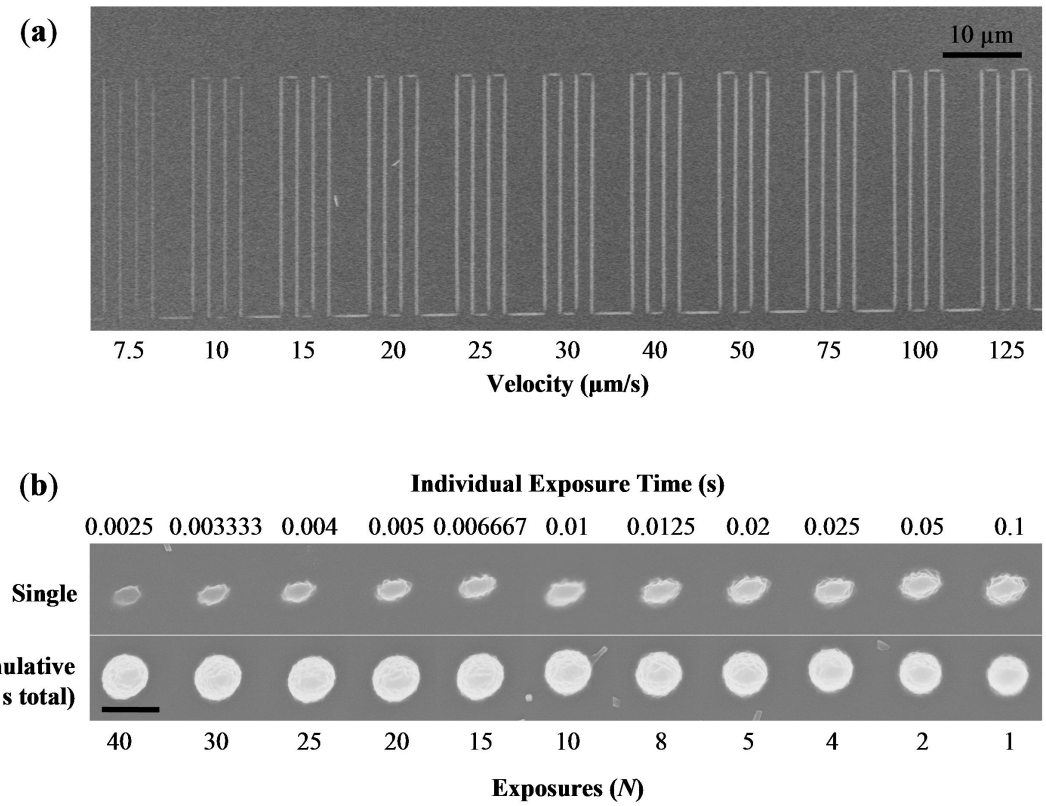

Figure 4.8. Experimental results for a velocity study (a) and exposure studies (b) with Rh6G as a MAP photoinitiator. The top line of (b) shows feature sizes resulting from single exposures of the listed duration. The bottom line of (b) shows the feature sizes resulting from multiple exposures when that individual exposure is repeated to a cumulative exposure of 0.1 s. Each SEM image is representative of the measured feature size trend. The scale bar in (b) represents 500 nm.

Figures 4.5b and 4.7b show the results of the exposure studies for MGCB and RhBB, respectively. Each SEM image is of a single voxel in a set that serves as a representative sample of the observed trend. The first line of voxels is from the single exposure study and the last line is from the corresponding cumulative 0.1 s exposure study. From the contrasting images, it is clear that for both MGCB and RhBB, the longer the exposure, the larger the transverse feature size. Additionally, there is some cumulative build-up of polymerization with multiple bursts of shorter duration, but the largest feature resulted from a single exposure equivalent to the cumulative exposure

duration. It can therefore be said that polymerization with MGCB and RhBB has a net negative cumulative effect, which is a hallmark of a conventional photoinitiator.

The contrast in fabrication trends between MGCB and MGC·HCl (Figure 4.6b) can be seen clearly in the differences in the cumulative exposure study.[5] Unlike MGCB, for MGC·HCl, the size of the features increases with the total number of exposures, even when the individual exposures were short. This phenomenon validates the assertion that for a PROVE photoinitiator, the short exposures provide enough time for excitation but not enough time for deactivation. The short exposures result in polymerization and have a net positive cumulative effect.

As with its velocity dependence, Rh6G exhibits a maximum in the cumulative exposure (Figure 4.8b) at some duration between a single exposure and the maximum number of exposures. This observation indicates that at a short enough exposure duration, Rh6G no longer has a net positive cumulative effect and begins to behave like a conventional photoinitiator. The value of ρ of Rh6G, therefore, is somewhere below that of MGC·HCl but above that of conventional photoinitiators such as MGCB and RhBB.

4.3.2 Kinetic Simulations

After analyzing the experimental results of the exposure studies, attention was turned to refining the kinetic model parameters. The first conclusion was that RhBB has a value of 0 for ρ. The premise for both self-deactivation and RAPID is that light of the same wavelength could be used for two-photon absorption and single-photon deactivation. While RhBB is capable of MAP at 800 nm, it is incapable of being deactivated using a second source. This observation eliminates the single-photon process as $k_{1P} = 0$, and

hence $\rho = 0$. While the results for MGCB suggest a fabrication trend similar to that of RhBB, the ability of MGCB to undergo deactivation via RAPID would mean that it must have a non-zero value for ρ, albeit relatively small.

Depending upon the kinetic rates, the fabrication trends for RhBB, MGCB and MGC·HCl are relatively simple to simulate for all three experiments as each represents an extreme calculated value for ρ: values for RhBB and MGCB were small (0 and 1 respectively), while the value for MGC·HCl was large (150,000). The fabrication results from using Rh6G, however, provide the key to understanding how a photoinitiator behaves when the value of ρ lies between that of a conventional photoinitiator and that of a PROVE photoinitiator. With this information, the kinetic parameters were altered systematically until they yielded results that fit all of the experimental data from the four photoinitiators. Table 4.2 shows the kinetic rate constants and the simulation constants used. The kinetic rate constants for the two-photon absorption and single-photon deactivation processes were considered to be relative values for the simulations, as they scale according to the values for ρ shown in Table 4.3. Overviews of the effect the value of ρ has on each experiment are shown in Figures 4.9, 11, and 13. The results of the simulations were overlapped with the each experimental result for the four photoinitiators (Figures 4.10, 12, and 14).

Table 4.2. Kinetic rate constants and simulation constants employed based on the kinetic model shown in Figure 4.2. The rates for two-photon absorption and single-photon deactivation are relative and scale by the self-deactivation efficiency, ρ calculated in Equation 4.1.

Kinetic Rate Constants (s^{-1})		Simulation Constants	
$k_{r,1}$	0.001	$[PI]_0$	1
$k_{r,2}$	1	I	0.1
k_A	1000	f_1	0.99
$k_{eff,1}$	1	f_2	0.01
$k_{eff,2}$	1000		
k_I	0.01		
k_{2P}	1		
k_{1P} (RhBB)	0		
k_{1P} (MGCB)	1		
k_{1P} (Rh6G)	3000		
k_{1P} (MGC·HCl)	15000		

Table 4.3. Calculated values for self-deactivation efficiency, ρ, based on experimental measurements for each MAP photoinitiator used in this study.

Photoinitiator	ρ
RhBB	0
MGCB	10
Rh6G	30000
MGC·HCl	150000

One of the more important kinetic rate constants is k_A, which reflects the time period between initial excitation and creation of the active intermediate state, A. From the simulations, k_A was assigned a value of 1000 s^{-1} indicating a lifetime of approximately 1 ms. This lifetime relates to RAPID in that the deactivation source must arrive within 1 ms in order to deactivate efficiently. In the original RAPID experiments, it was observed that deactivation was capable of occurring at delays of longer than 13 ns, the experimental limit of pulse-synchronization at that time. It seems that deactivation is

possible on a timescale that was nearly 5 orders of magnitude longer than previously tested.

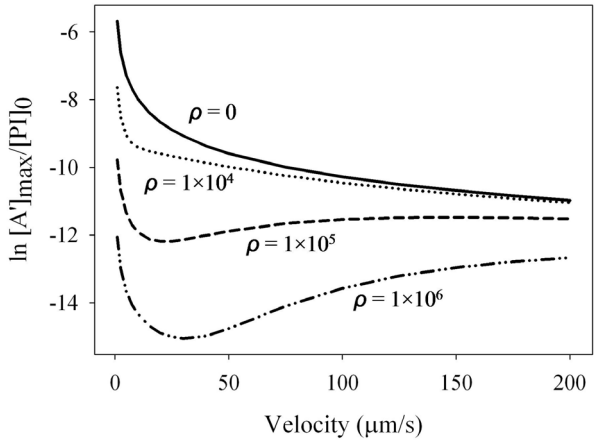

Figure 4.9. Overview of velocity simulations using kinetic models shown in Figure 4.2 and kinetic parameters identified in Table 4.2. Simulations were performed by measuring the maximum concentration of A′ of a single location along a line when exposed to a Gaussian laser beam with a 0.5 μm FWHM. While radical concentration increases at lower velocities, inefficient initiation of polymerization by photoinitiators with higher values of ρ make fabrication in those ranges impossible without localized heating causing explosions.

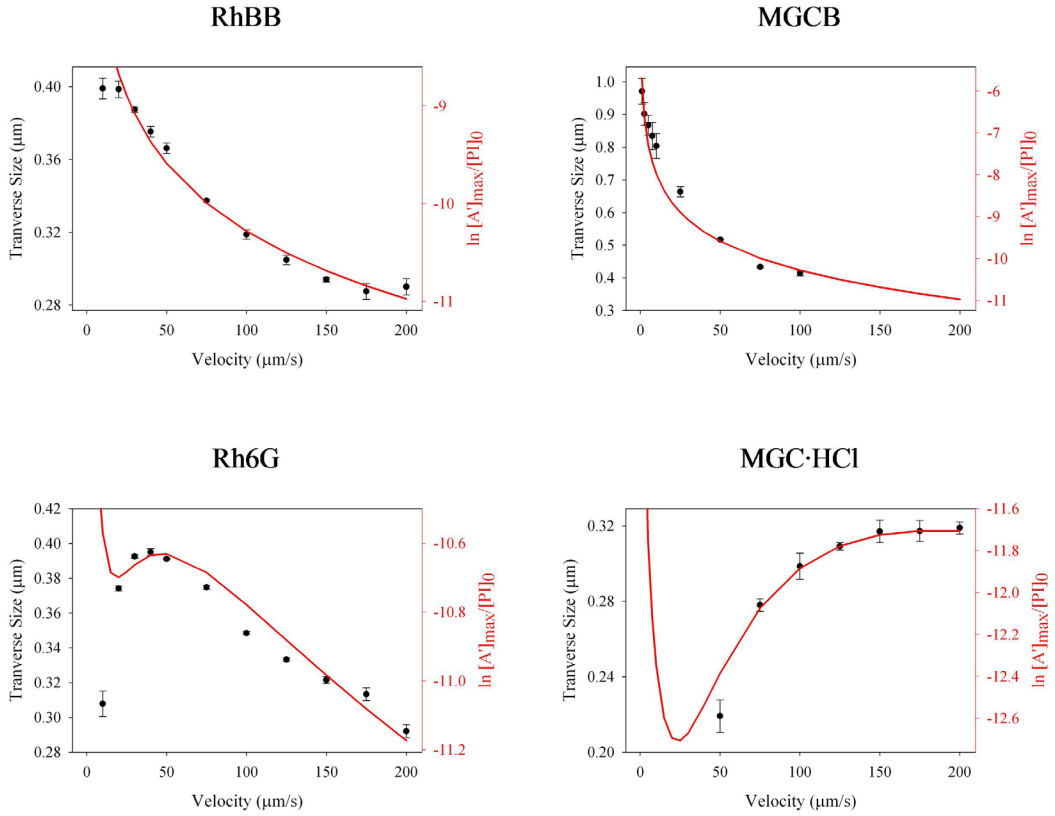

Figure 4.10. Overlap of velocity dependence experimental results for the four MAP photoinitiators and kinetic simulations of associated values for ρ listed in Table 4.3.

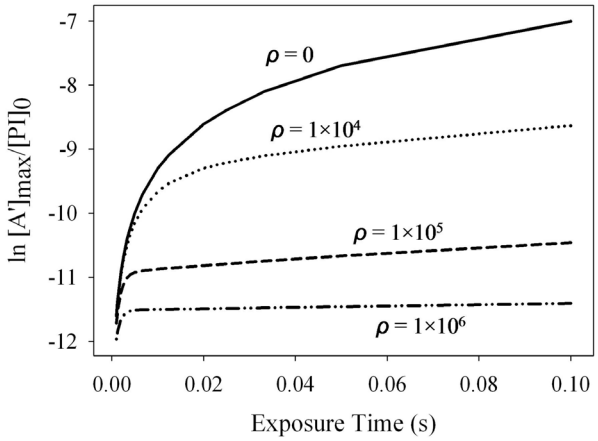

Figure 4.11. Overview of single-exposure simulations using the kinetic models shown in Figure 4.2 and the kinetic parameters identified in Table 4.2.

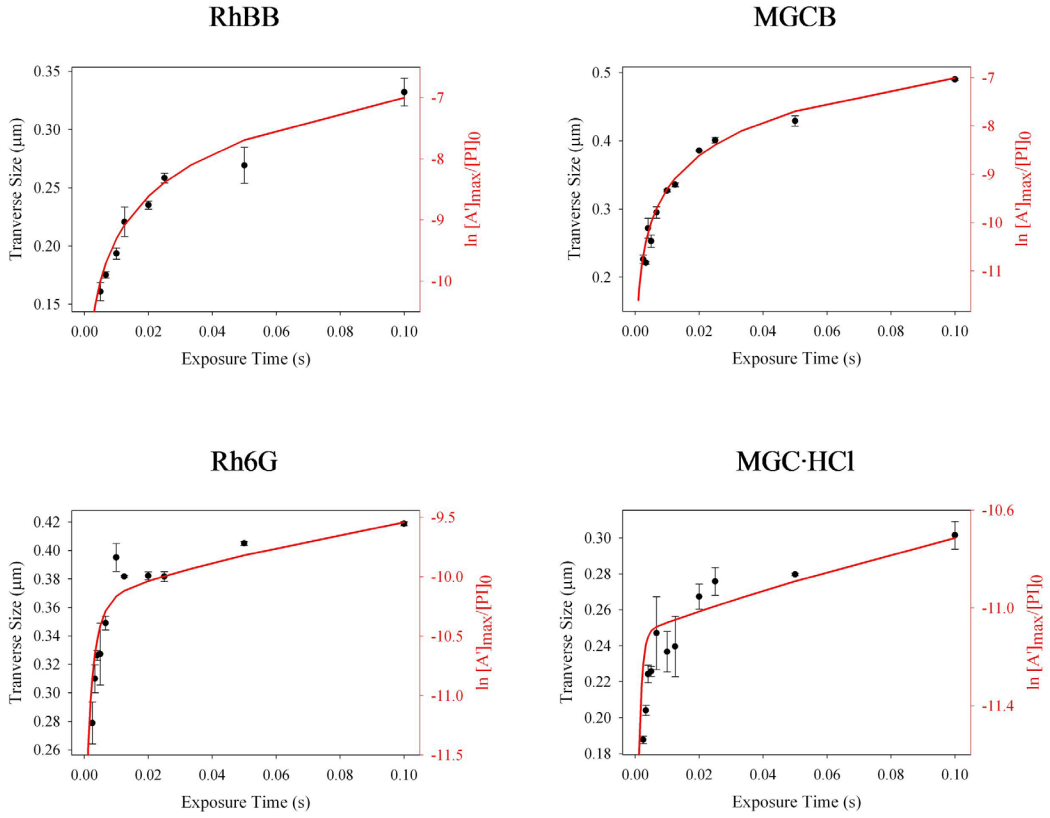

Figure 4.12. Overlap of single-exposure experimental results for the four MAP photoinitiators and the kinetic simulations of associated values for ρ listed in Table 4.3.

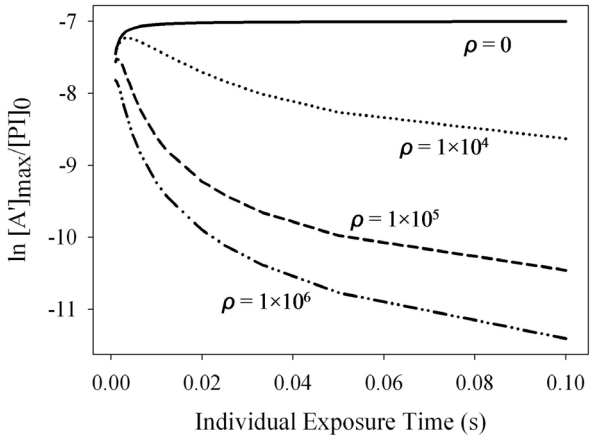

Figure 4.13. Overview of the cumulative-exposure simulations using kinetic models shown in Figure 4.2 and the kinetic parameters identified in Table 4.2. The total exposure was 0.1 s with a delay of 1.0 s between each exposure.

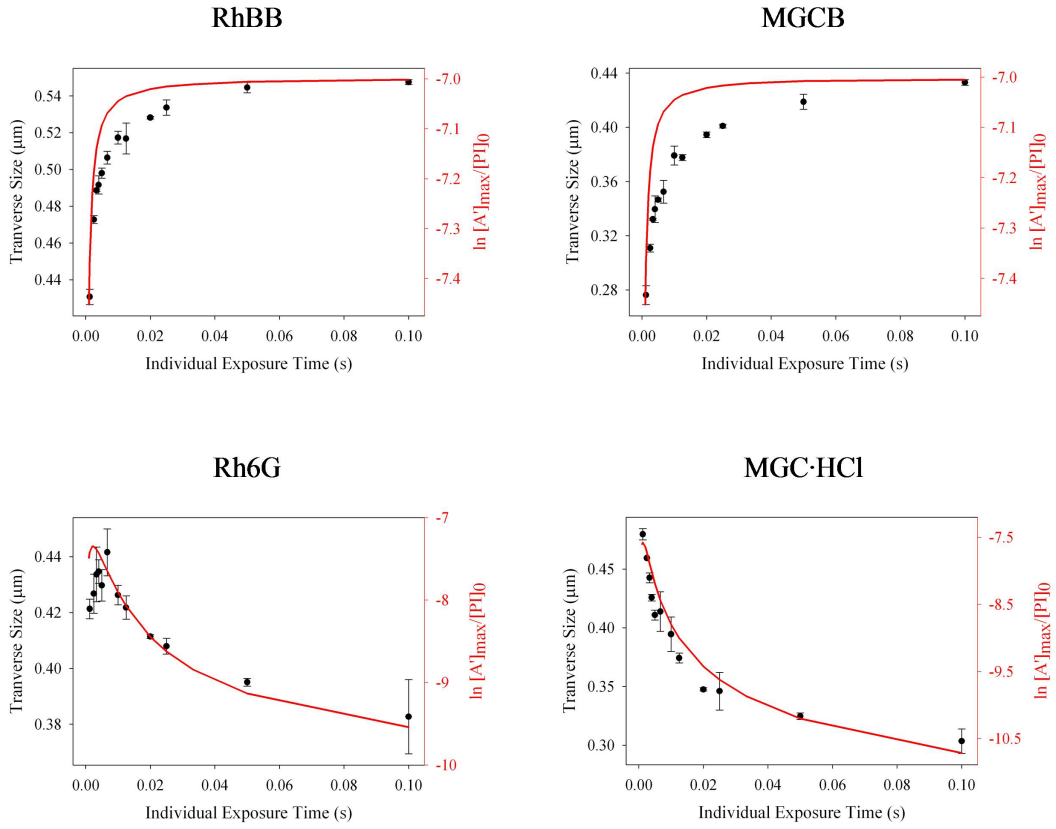

Figure 4.14. Overlap of the cumulative-exposure experimental results for the four MAP photoinitiators and kinetic simulations of associated values for ρ listed in Table 4.3.

The other parameter of note is the branching ratio of f_1 to f_2. It seems that approximately 99% of the active intermediate, which leads to polymerization, goes

through the slower and more probable deactivation route. The remaining 1% goes via a faster pathway and is less likely to be deactivated. This faster pathway should account for the inability to deactivate above a certain excitation intensity.[4]

Even though the simulations mimic all the polymerization experiments, it should be noted that the simulations actually reflect the relative concentration of radicals. The simulated results show a natural logarithmic relationship to the experimental data, which is most likely a consequence of the Gaussian spatial shape of the radical concentration that lies above the threshold, $[R]_{threshold}$, required to initiate polymerization:

$$[R]_{threshold} = [R]_0 \exp\left[-\frac{(x_{threshold})^2}{\sigma^2}\right] \tag{4.10}$$

$$x_{threshold} = \sigma\sqrt{\ln\left(\frac{[R]_0}{[R]_{threshold}}\right)} \tag{4.11}$$

where $x_{threshold}$ is the distance from the beam center. Additionally, further discrepancies between the experimental data and the logarithmic simulation results are likely due to an intermediate state that is not accounted for.

4.4 Conclusions

Through the use of three different experiments varying the exposure conditions of fabrication in four MAP photoinitiators, and a kinetic model designed for MAP photoinitiators capable of undergoing deactivation, important information about the excitation and deactivation processes was extracted. Of the four photoinitiators, MGC·HCl was the photoinitiator that exhibited the most efficient self-deactivation ($\rho \approx$ 150,000). Additionally, based on previous qualitative velocity dependence studies of the

cationic dyes discussed in Chapter 3, MGC·HCl would appear to be the extreme of PROVE dependence. Conventional photoinitiators such as MGCB have relatively low values of ρ ($\rho \approx 1$), but this low value can be overcome by the addition of a second deactivation source as with RAPID. Photoinitiators such as Rh6G ($\rho \approx 30{,}000$), can also exist for which the exposure dependence is more sensitive and can exhibit both conventional and PROVE trends.

Assigning values for ρ to analogous dyes should yield values somewhere in the same range. As a result, photoresists for MAP and RAPID could be tailored to a specific application in which it would be important to understand the implications of varying fabrication velocity. The kinetic rate constants extracted from simulations such as the ones presented here should also provide a pathway for the most efficient deactivation parameters to be set in order to create features with a size below $\lambda/20$.

References:

(1) Stocker, M. P.; Li, L. J.; Gattass, R. R.; Fourkas, J. T., Multiphoton photoresists giving nanoscale resolution that is inversely dependent on exposure time. *Nature Chemistry* **2011,** 3, (3), 223-227.

(2) LaFratta, C. N.; Fourkas, J. T.; Baldacchini, T.; Farrer, R. A., Multiphoton fabrication. *Angewandte Chemie-International Edition* **2007,** 46, (33), 6238-6258.

(3) Sun, H.-B.; Kawata, S., Two-Photon Photopolymerization and 3D Lithographic Microfabrication. *Advances in Polymer Science* **2004,** 170, 169-273.

(4) Li, L.; Gattass, R. R.; Gershgoren, E.; Hwang, H.; Fourkas, J. T., Achieving lambda/20 Resolution by One-Color Initiation and Deactivation of Polymerization. *Science* **2009,** 324, (5929), 910-913.

(5) Stocker, M. P.; Fourkas, J. T., Elucidating the kinetics and mechanism of RAPID lithography. *Proceedings of SPIE* **2012,** 8249, 824902-1-7.

Chapter 5: Conclusions and Future Work

5.1 Conclusions

The field of micro- and nanoscale patterning has thrived in the last few decades with new techniques constantly being developed to push feature sizes to new minimums. However, the fundamental limits of photolithography are beginning to be reached as the cost of producing the energy required to produce the features continues to rise as the feature sizes decrease. The focus can no longer be on producing radiation or charged particles with sufficiently short wavelengths to push lithographic features to smaller sizes. The best way forward may just be to step back and use light sources in the visible and near-IR and instead alter the photochemistry of polymerization. In this way, costs are conserved and the Abbe criterion is no longer the limiting factor in lithographic resolution. Multiphoton absorption polymerization (MAP) has shown the promise of producing sub-100 nm feature sizes and the capability to produce complex, 3D structures. With the incorporation of resolution augmentation through photo-induced deactivation (RAPID), the features sizes can be made smaller and the previous mark of $\lambda/20$ can be beat.

In Chapter 3, a variety of dye molecules were tested to determine their capabilities as radical photoinitiators that can undergo RAPID. It was determined that many of these molecules are so efficient at deactivation that they were capable of undergoing self-

deactivation without the need for a second laser source. This phenomenon leads to the feature size having a proportional velocity (PROVE) dependence. Given this broad assortment of cationic dye molecules, photoresists can be tailor-made for specific applications. Incorporating mixtures and changing environmental conditions such as pH allows photoresists to be tuned to behave either with a PROVE dependence or a conventional velocity dependence, or even to be velocity-independent for a range of velocities.

Chapter 4 provided a more detailed study into the kinetic mechanisms involved photoexcitation and photodeactivation. Four dye molecules that exhibited different fabrication characteristics were studied in depth. Malachite green carbinol base (MGCB) has only a slight ability to self-deactivate but is capable of undergoing deactivation with the addition of a second CW laser source at the same excitation wavelength. Rhodamine B base (RhBB) has no self-deactivation capability and cannot be force to deactivate via RAPID. Malachite green carbinol hydrochloride (MGC·HCl) is extremely efficient at self-deactivation requiring higher velocities and higher power intensities to fabricate. Rhodamine 6G (Rh6G) exhibits a self-deactivation efficiency in between those of MGCB and MGC·HCl. By applying a kinetic model to overlap with experimental data from these photoinitiators, we were able to account for the broad range of polymerization characteristics. Kinetic rates and intermediate lifetimes were then extracted to provide a wide breadth of information applicable to understanding and improve deactivation.

5.2 Future Work

5.2.1 RAPID Exposure Studies

The kinetic rate constants determined in Chapter 4 need to be verified through further exposure timing experiments. One of the most critical parameters to verify is the time between excitation and the formation of the active intermediate, proposed here to be ~1 ms. This goal can be reached by performing a RAPID voxel study in which the timing between exposures of excitation and deactivation is varied. The exposure control of the deactivation beam would be accomplished through the use of a second acousto-optic modulator. These complex timing sequences will require precision in synchronizing and delivering the triggers to each acousto-optic modulator to initiate exposure. MGCB would serve as the model photoresist.

The expectation would be that for delays between excitation and deactivation exposures of longer than 1 ms, the feature size should behave as if no deactivation had occurred. Delays of 1 ms or shorter should lead to correspondingly smaller features indicating deactivation took place. If the phase mask were to be applied, the most definitive method for measuring the relative axial feature size would be via atomic force microscopy (AFM).

5.2.2 Refinement of the Kinetic Model

With a better estimate of the kinetic rate constants through additional exposure studies, the parameters in the kinetic model (Figure 5.1a) should be refined further. The model itself could also be refined in a number of different ways. The first possibility is to

alter the branching pathway, as shown in Figure 5.1b. In doing so, another intermediate is added as an alternate destination for the excited photoinitiator molecule. This scheme provides a pathway that cannot, under any circumstances, be deactivated and will always lead to initiation of polymerization. The radical concentration would be observed by tracking A″.

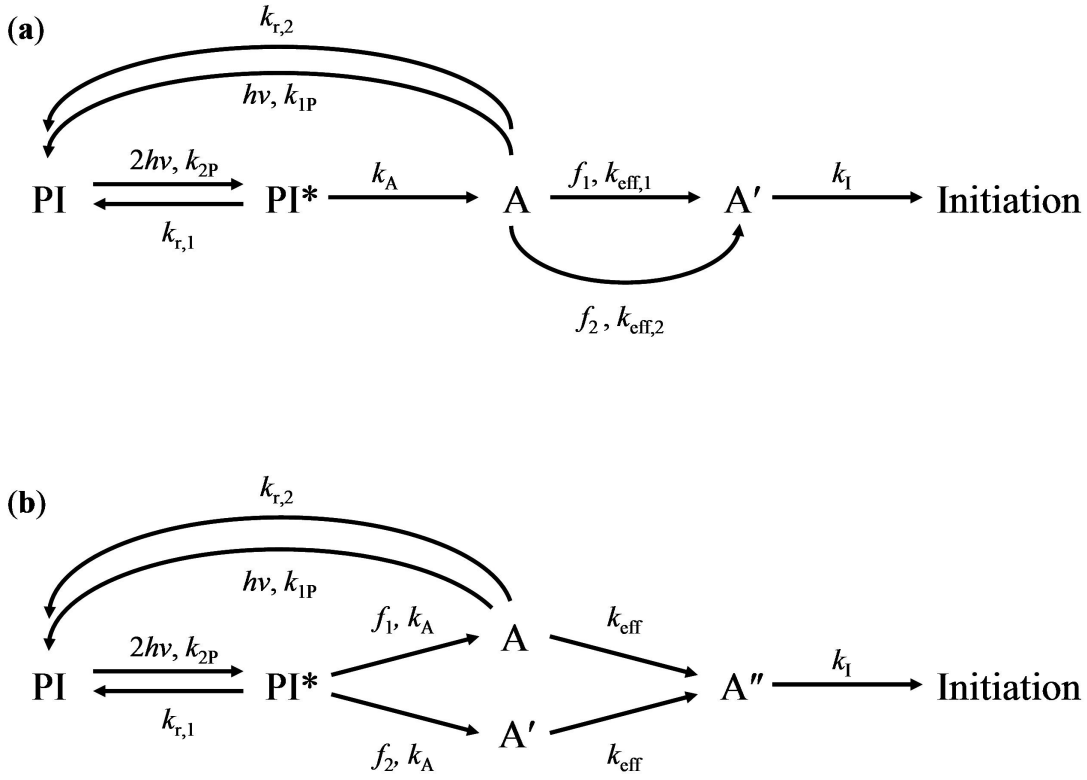

Figure 5.1. Kinetic models for photodeactivation. The kinetic simulations presented in Chapter 4 used model (a). A possible variation of the kinetic model is presented in (b). Here, the branching pathway is altered so that one pathway produces A′, which is not capable of being deactivated. The radical concentration is observed by tracking A″.

An additional method for refining the kinetic model is to incorporate the concept of the radical threshold in more detail. In Figure 5.1b, k_I represents the rate constant for which initiation occurs from intermediate A′, which is used to track the radical concentration in this model. However, this rate might actually reflect the existence of the radical threshold by allowing the intermediate, A′, to slowly proceed to initiation.

Determination of the relationship between k_I and the Gaussian spatial shape of the radical concentration above the threshold is essential and could possible better align the experimental and simulation data.

5.2.3 Customization of Photoresists

After the kinetic model has been refined, simulations of varying self-deactivation efficiencies, ρ, should be compared to experimental data for the photoinitiators not studied in Chapter 4, but known to have some degree of PROVE dependence as determined in Chapter 3. Values for ρ could then be assigned to each photoinitiator to build a database.

Photoresists could then be created to match specific applications. For example, if an applications calls for the creation a complex array of lines without the consequences of large features at the turning points, a photoresist with a large ρ could be prescribed. If intricate details are required, an initiator with a medium value for ρ (more velocity-independent) could be used. Alternatively, if very fine features at high resolution are required, a photoinitiator with a small value for ρ could be used with RAPID to provide precise deactivation.

Other, more novel tuning of polymerization trends should also be investigated including the use of the thermochromic effect, particularly with crystal violet.[1] If the temperature of the photoresist could be altered during fabrication, the polymerization trends could be altered *in situ*, making it very powerful in creating various features with only a single photoresist.

5.2.4 Single-Photon RAPID

One of the more promising extensions of RAPID is its use with single-photon excitation.[2,3] In this method, a CW 405 nm laser is used to initiation polymerization while a CW 800 nm laser induces deactivation, the results of which are shown in Figures 5.2b,d. The advantages to linear excitation include a higher efficiency of polymerization with absorption of a single-photon as well the prospect of using two CW laser sources. The polymerization efficiency is advantageous because it would require only a relatively small amount of power to fabricate smaller features. It could also be extended high-speed fabrication using a higher laser power, which would be advantageous for fabricating on silicon wafers in an industrial lithography process that requires fast velocities across large areas. High resolution features could be realized by scanning the 405 nm source across an area while deactivating at 800 nm.

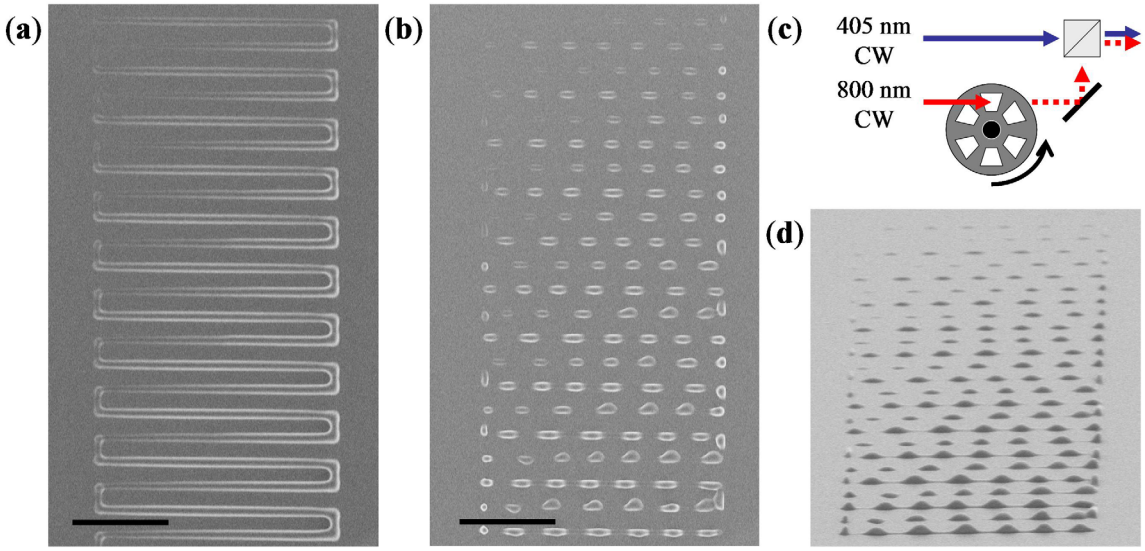

Figure 5.2. SEM images of single-photon polymerized lines using MGCB as a photoinitiator. Lines fabricated without deactivation are shown in (a). Line fabricated with a deactivation beam being chopped (b) according to the diagram (c). A 60° tilted view of (b) is shown in (d). A CW 405 nm laser source was used for excitation and a CW 800 nm laser source was used for deactivation. The scale bars represent 25 µm.

Using two CW laser sources is less expensive than using a pulsed laser source. To produce the small amount of power necessary with 405 nm, a simple light-emitting diode (LED) could be used. For more uniform features, a collimated diode laser source could be used. For deactivation, there are many commercially-available diode lasers with wavelengths near 800 nm.

The main disadvantage of using single-photon polymerization is the inability to localize polymerization effectively. With a two-photon process, polymerization is confined to the focal region of the laser. With a single-photon process, this localization is not necessarily the case. If the power of the CW 405 nm source is set appropriately, the only area in which the intensity of the beam is high enough to initiate polymerization would be the focal region. The problem becomes an accumulation of radicals the longer the laser is left exposed in the photoresist, resulting in a slow increase in feature size, as shown in Figure 5.2a.

The most logical method for avoiding the increase in feature size is to instead use a thin film of photoresist. The consequence of using a thin film is the loss of the capability to fabricate in all three dimensions; however, this consequence is acceptable for 2D patterning in industrial photolithography. The most likely method for applying a thin film is by spin-coating the photoresist onto the substrate. This process presents a number of challenges. First, it requires the photoresist to have a very low viscosity and, therefore, must incorporate a volatile solvent that will evaporate upon spin-coating. The less viscous the mixture and the faster the spin, the thinner the film will be. The goal would be to produce a film of 100 nm or less, depending upon the application for which the features are intended, namely metal deposition or material etching. The second

challenge in creating a thin film is the even distribution of photoinitiator within the acrylic monomers. There must be a sufficient amount of photoinitiator to overcome the radical threshold for polymerization and it must be evenly distributed so all features would have the same dimensions.

References:

(1) Burkinshaw, S. M.; Griffiths, J.; Towns, A. D., Reversibly thermochromic systems based on pH-sensitive spirolactone-derived functional dyes. *Journal of Materials Chemistry* **1998,** 8, (12), 2677-2683.

(2) Li, L.; Gattass, R. R.; Gershgoren, E.; Hwang, H.; Fourkas, J. T., Achieving lambda/20 Resolution by One-Color Initiation and Deactivation of Polymerization. *Science* **2009,** 324, (5929), 910-913.

(3) Stocker, M. P.; Li, L. J.; Gattass, R. R.; Fourkas, J. T., Multiphoton photoresists giving nanoscale resolution that is inversely dependent on exposure time. *Nature Chemistry* **2011,** 3, (3), 223-227.

Appendix A: LabVIEW Programs

LabVIEW programs with front panel views and relevant block diagram details. The connector is the diagram seen if VI is used as a sub VI. Embedded VIs are the sub VIs used in the program.

Name: SEM Image Measurement.vi

Connector: none

Embedded VIs:

Picture Control to 2D Pixmap.vi

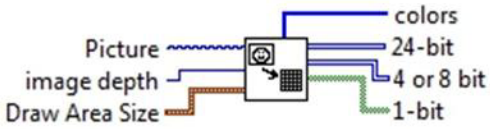

rotate pixmap.vi

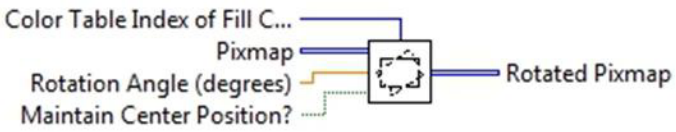

Front Panel:

Block Diagram:

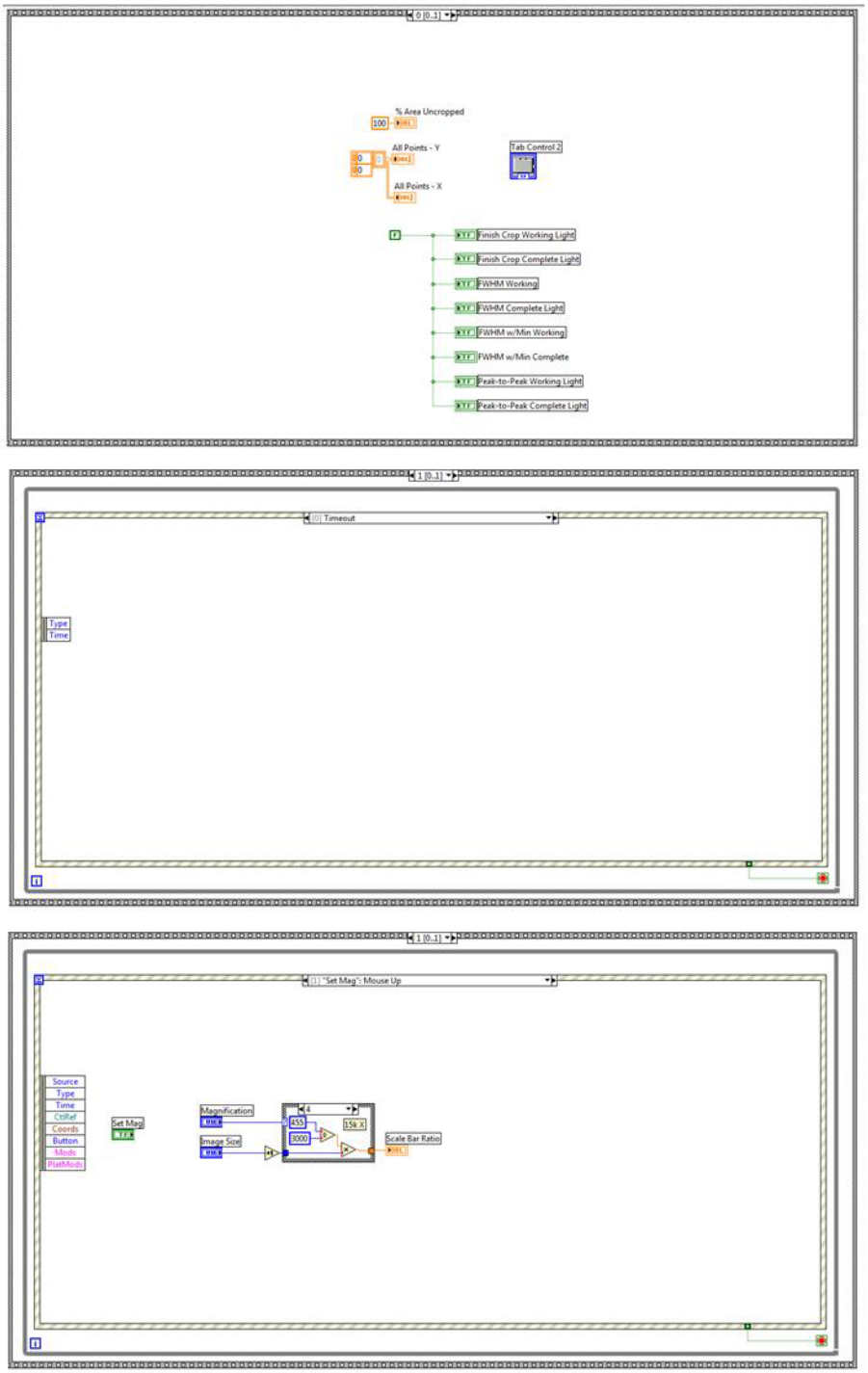

Block Diagram:

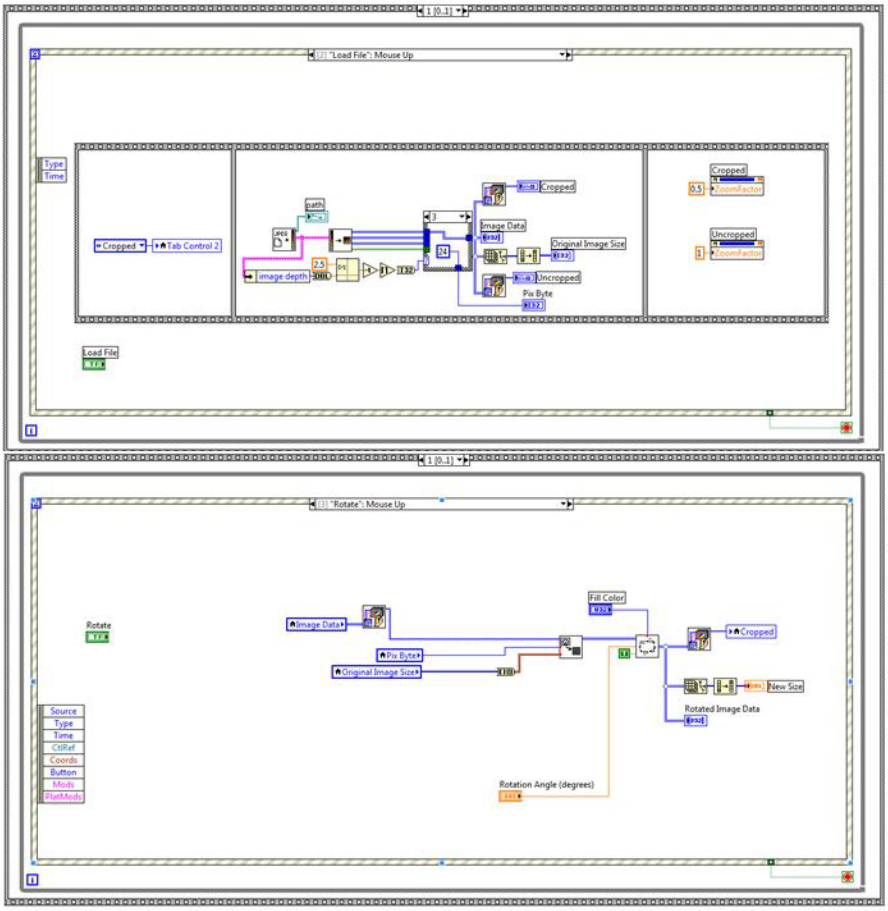

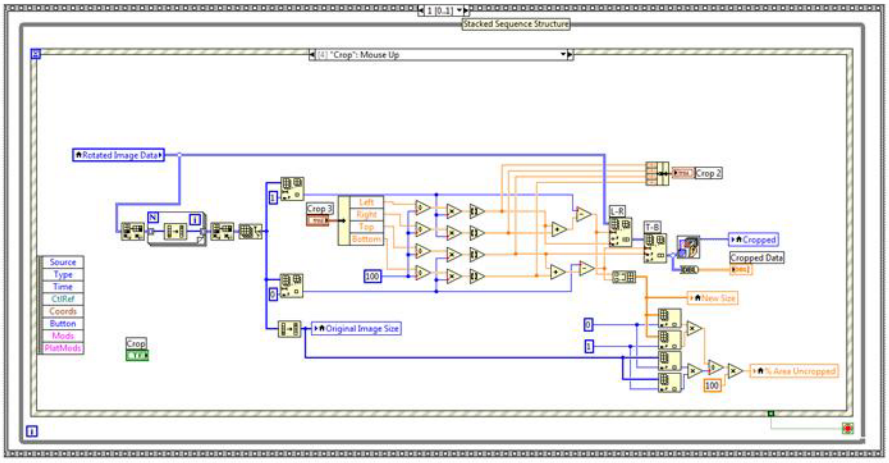

Block Diagram:

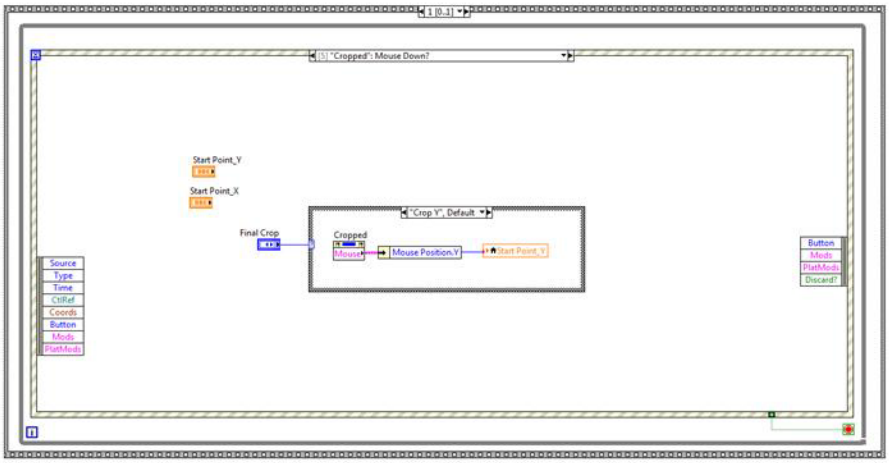

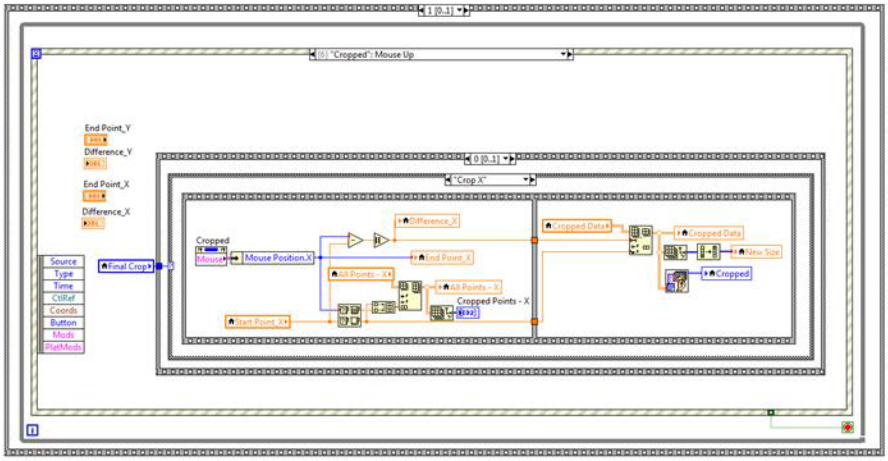

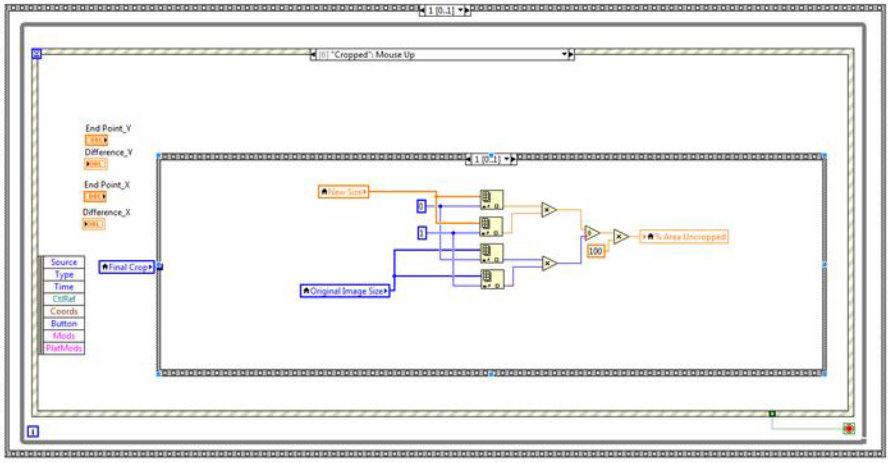

Block Diagram:

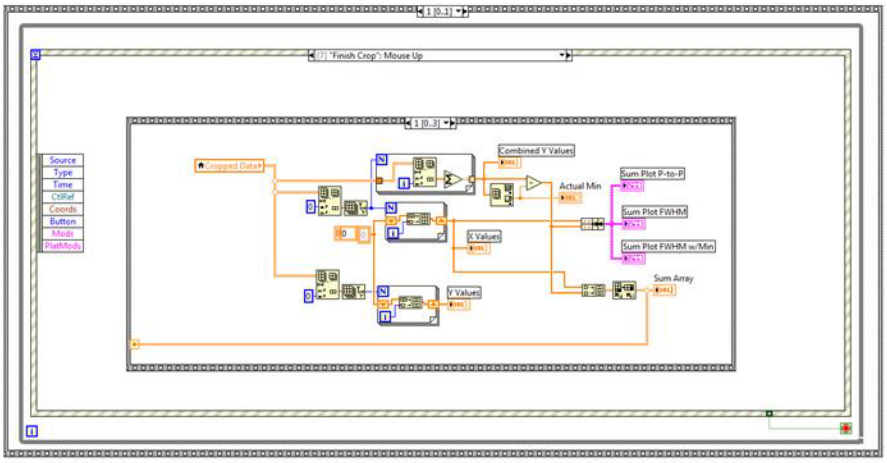

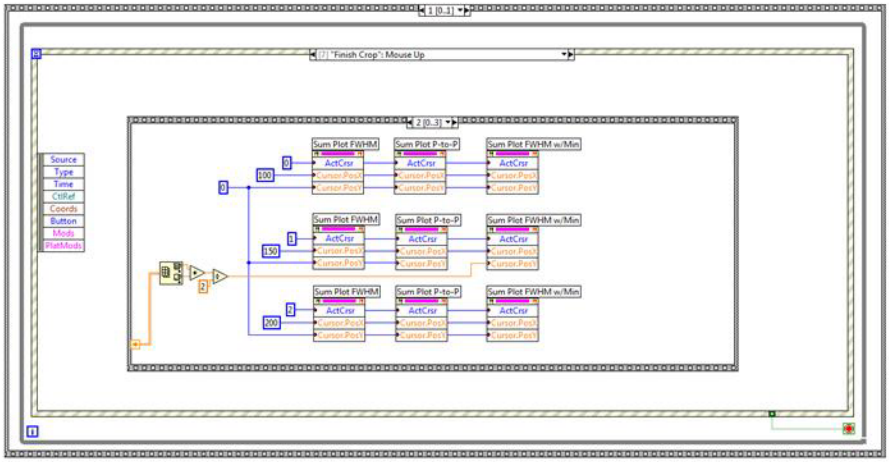

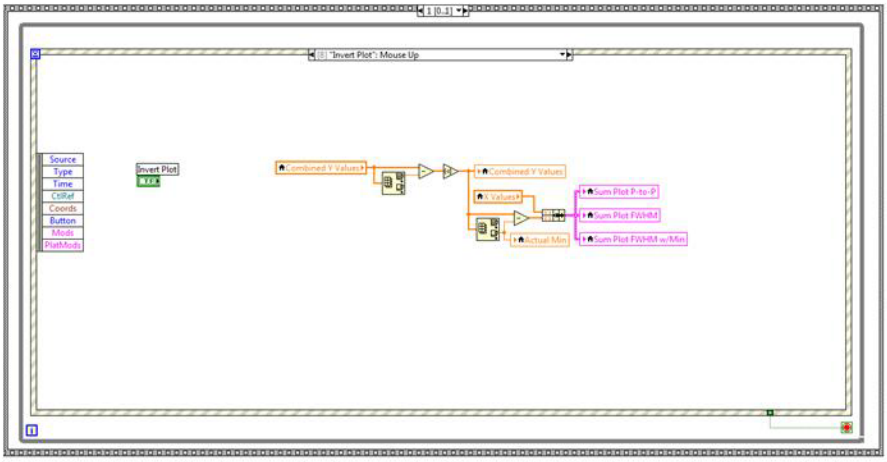

Block Diagram:

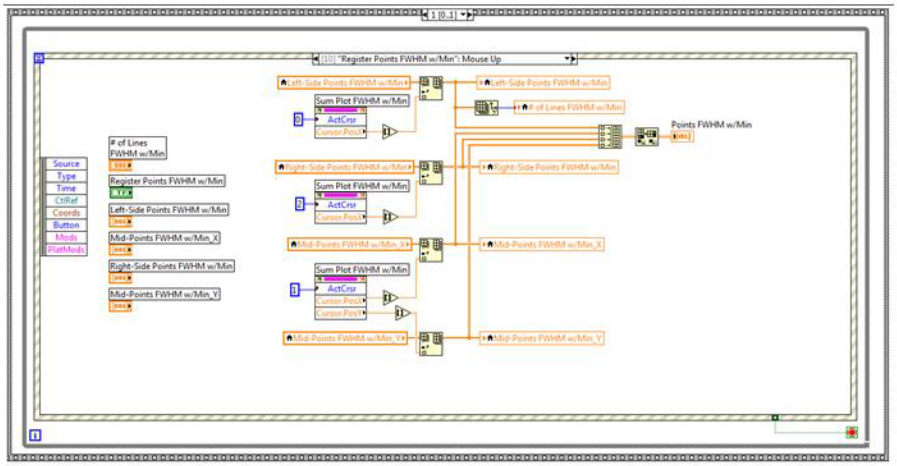

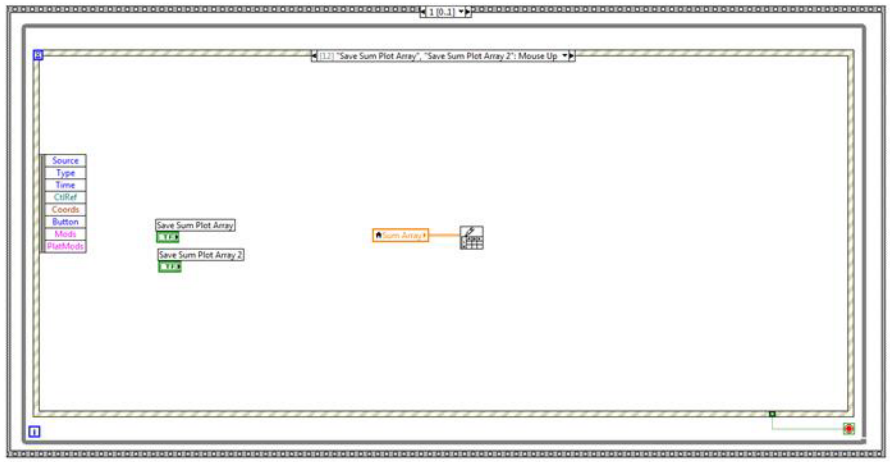

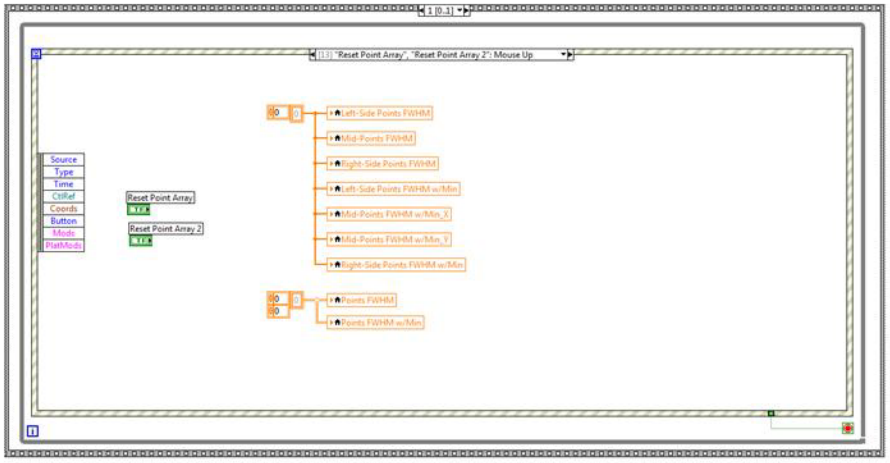

Block Diagram:

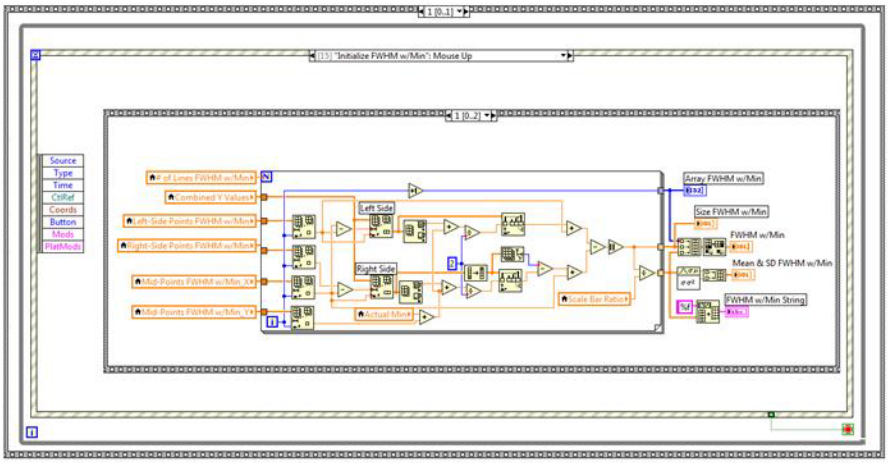

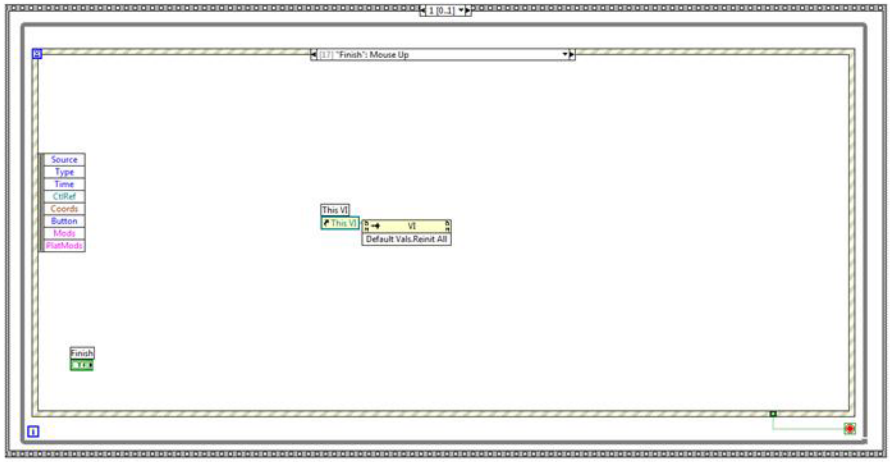

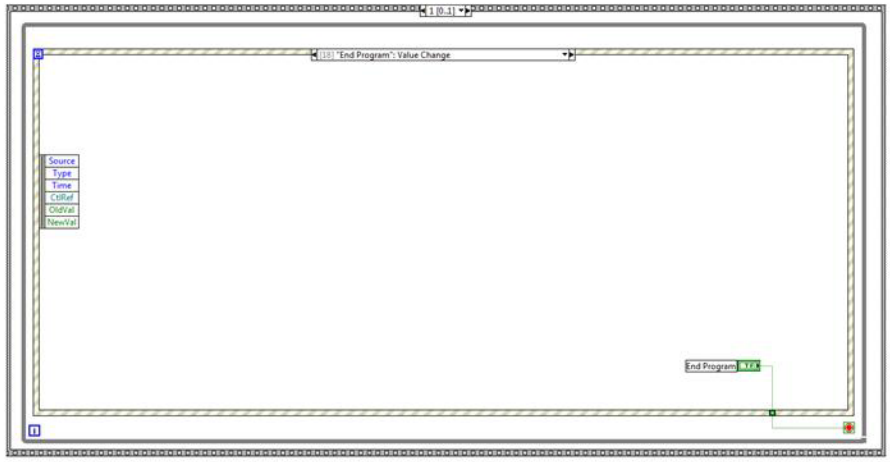

Name: Lights ON Calculations_SubVI.vi

Connector:

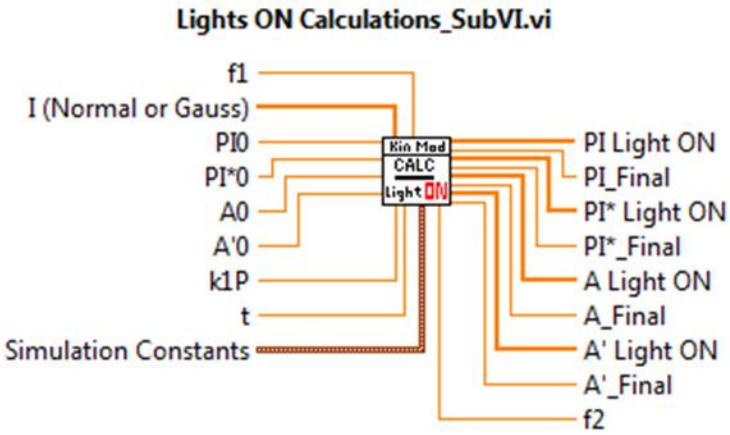

Embedded VIs: none

Front Panel:

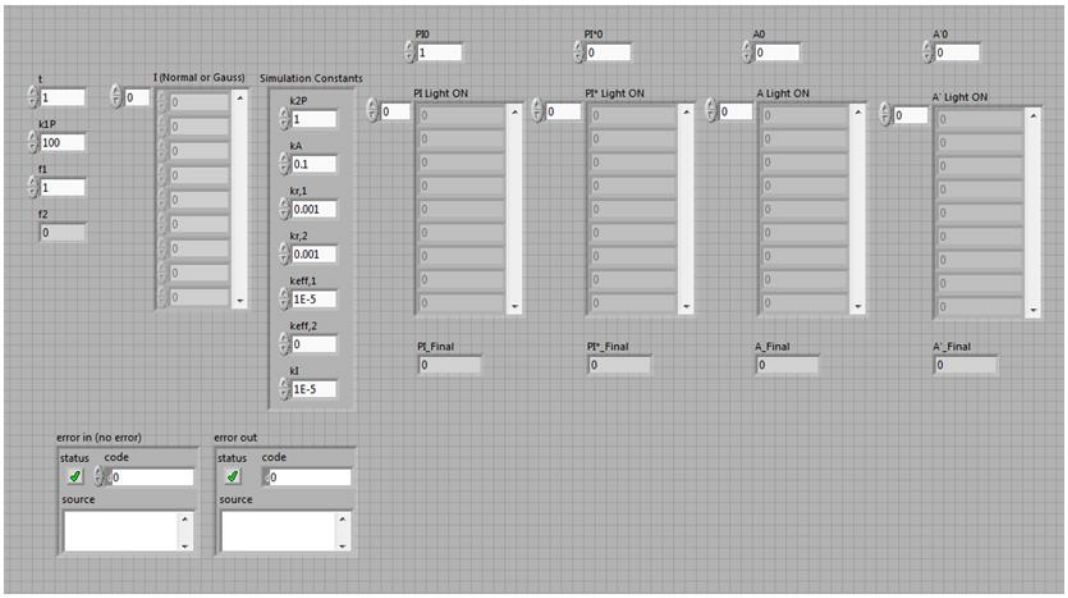

Block Diagram:

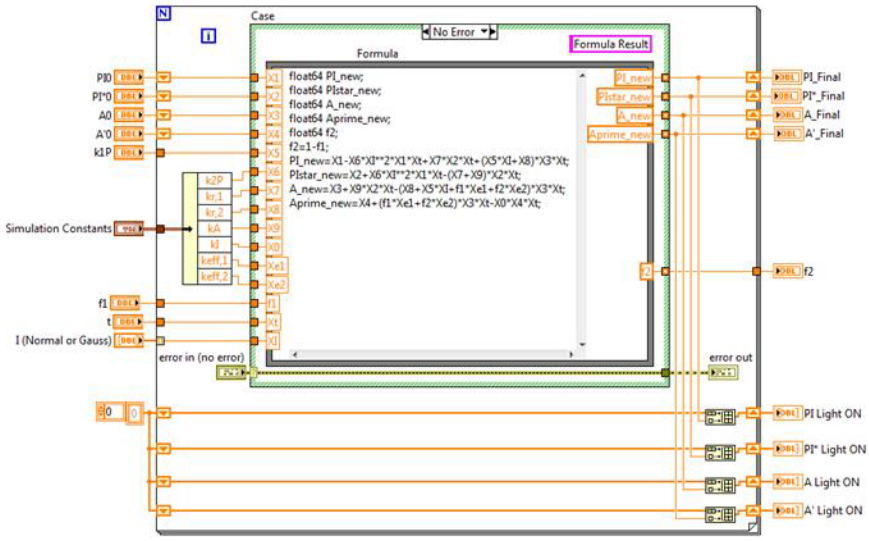

Name: Kinetic Modeling_AO Simulations.vi

Connector: none

Embedded VIs:

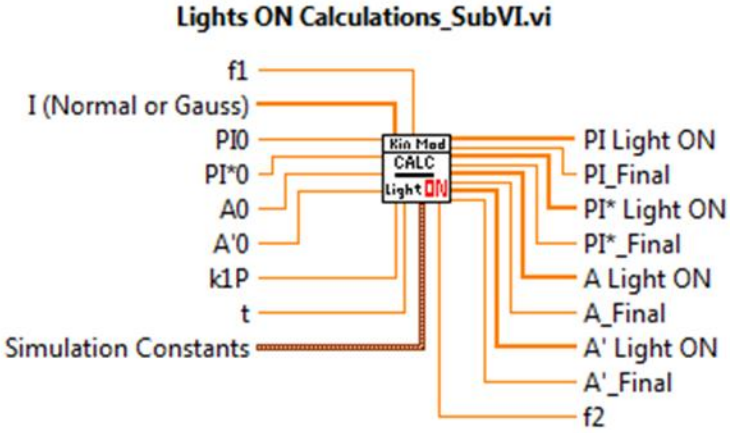

Front Panel:

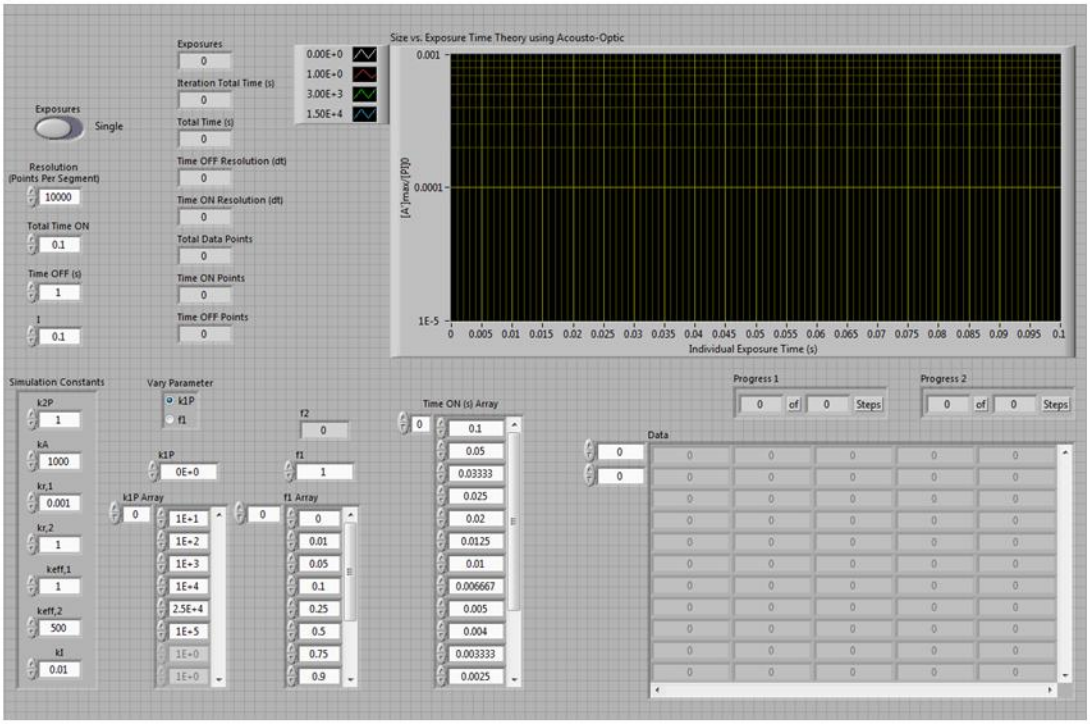

Block Diagram:

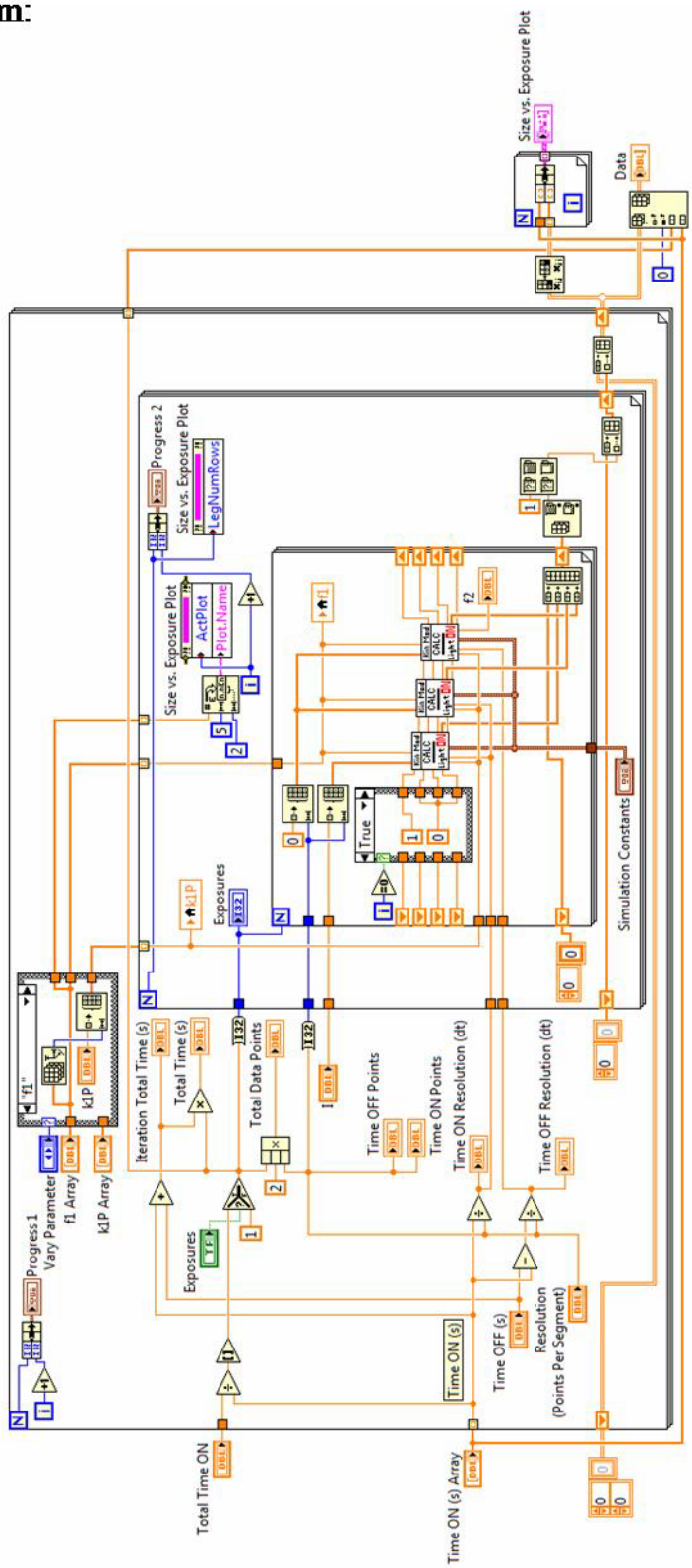

Name: I_Gaussian Beam_subVI.vi

Connector:

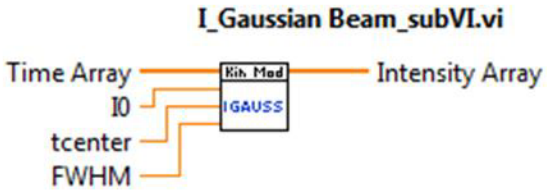

Embedded VIs: none

Front Panel:

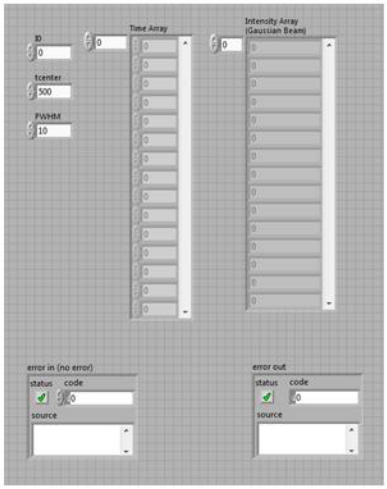

Block Diagram:

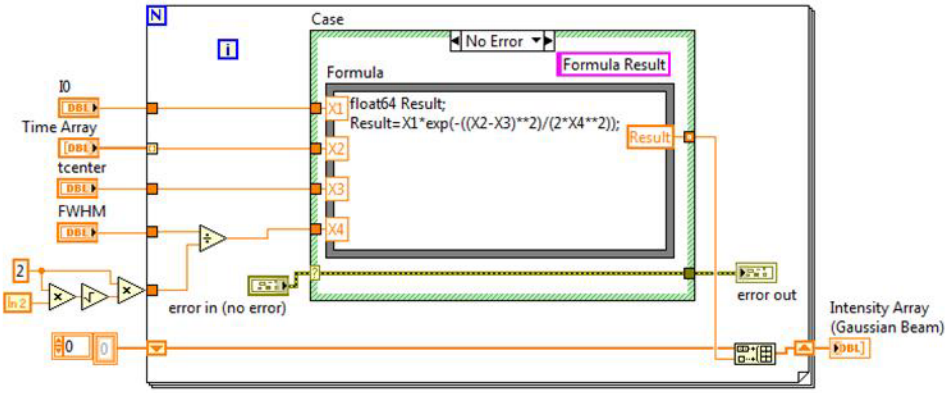

Name: Kinetic Modeling_Velocity Simulations.vi

Connector: none

Embedded VIs:

I_Gaussian Beam_subVI.vi

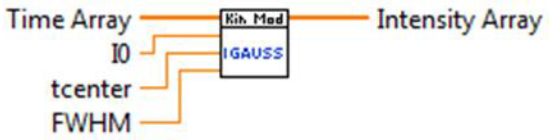

Lights ON Calculations_SubVI.vi

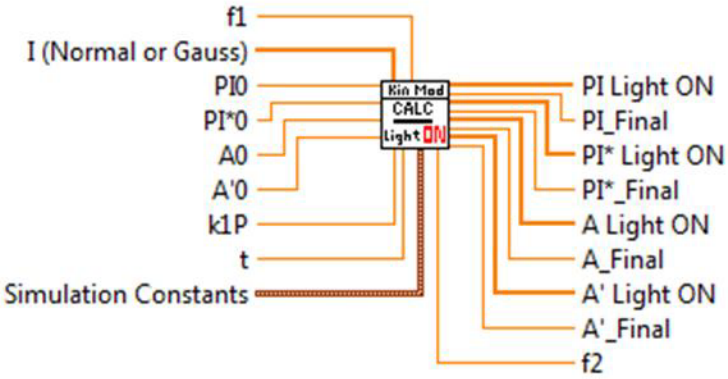

Front Panel:

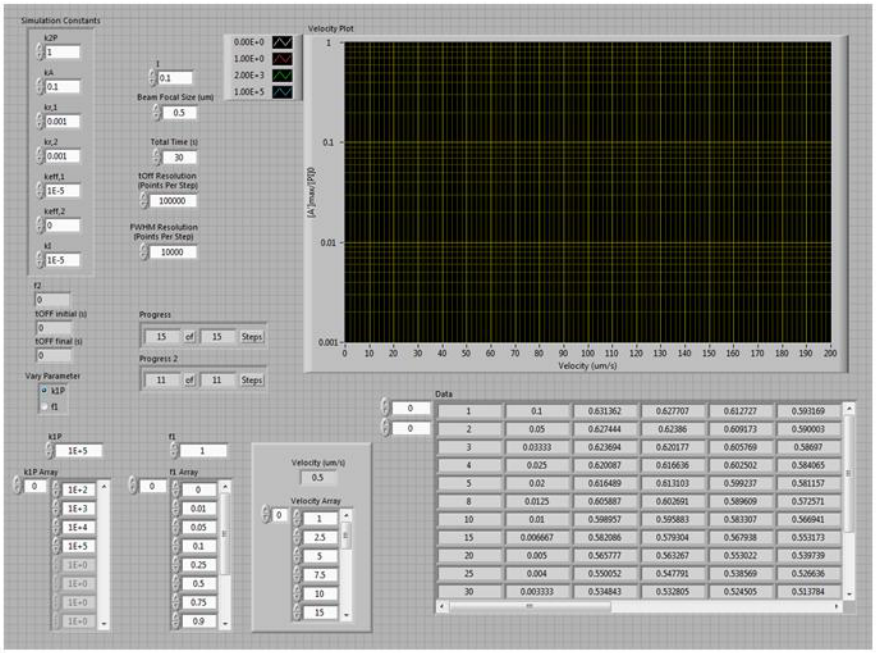

Block Diagram:

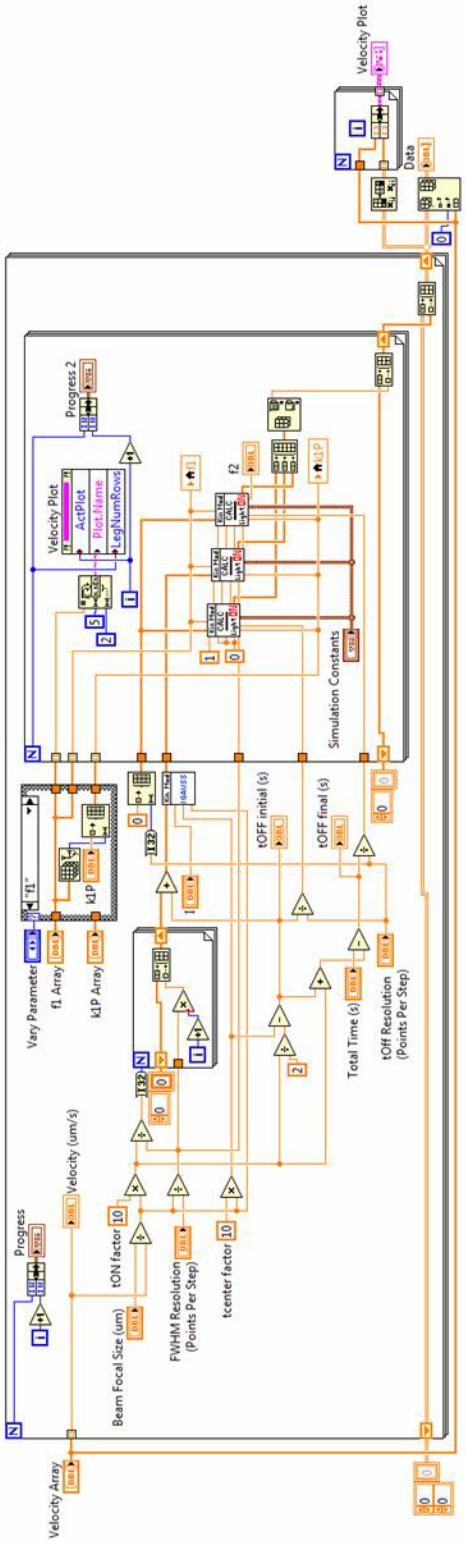

Name: Set X Acceleration.vi

Connector:

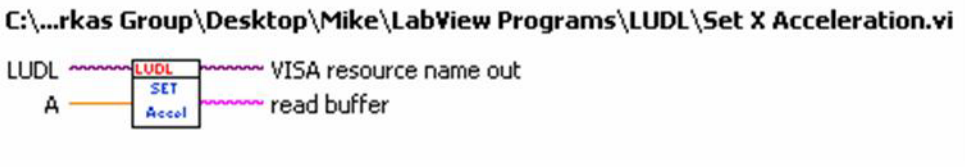

Embedded VIs:

Front Panel:

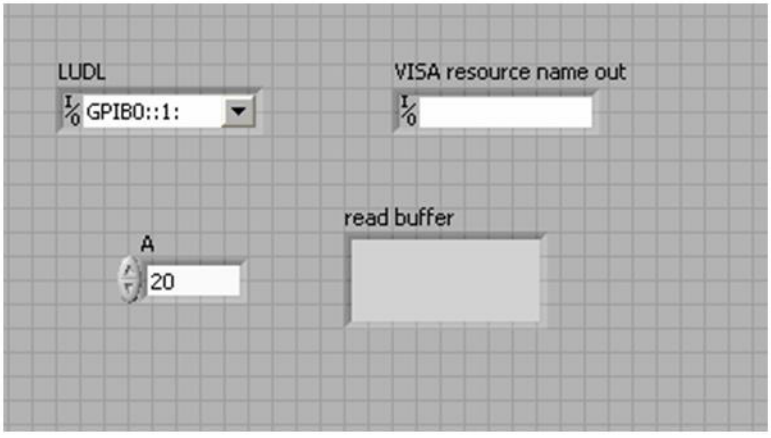

Block Diagram:

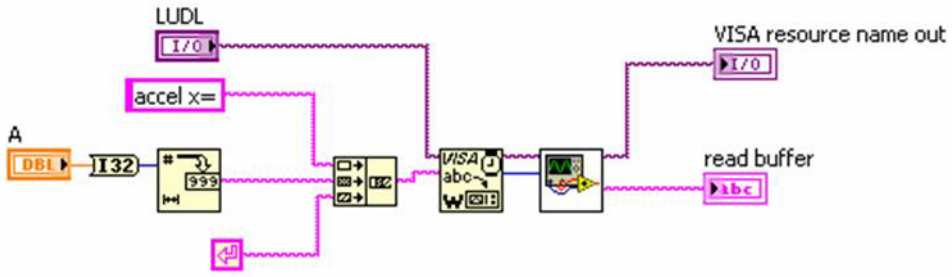

Name: AO Burst VI_MS.vi

Connector:

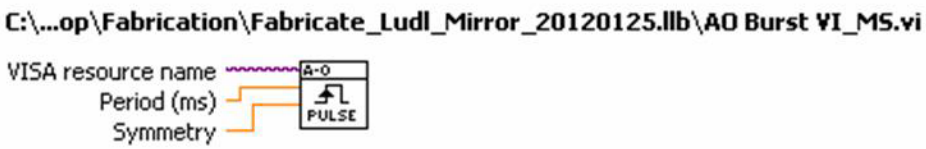

Embedded VIs: none (manufacturer drivers)

Front Panel:

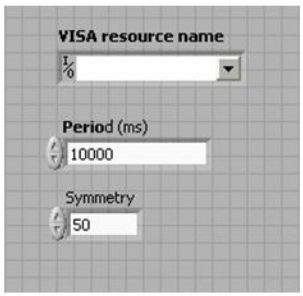

Block Diagram:

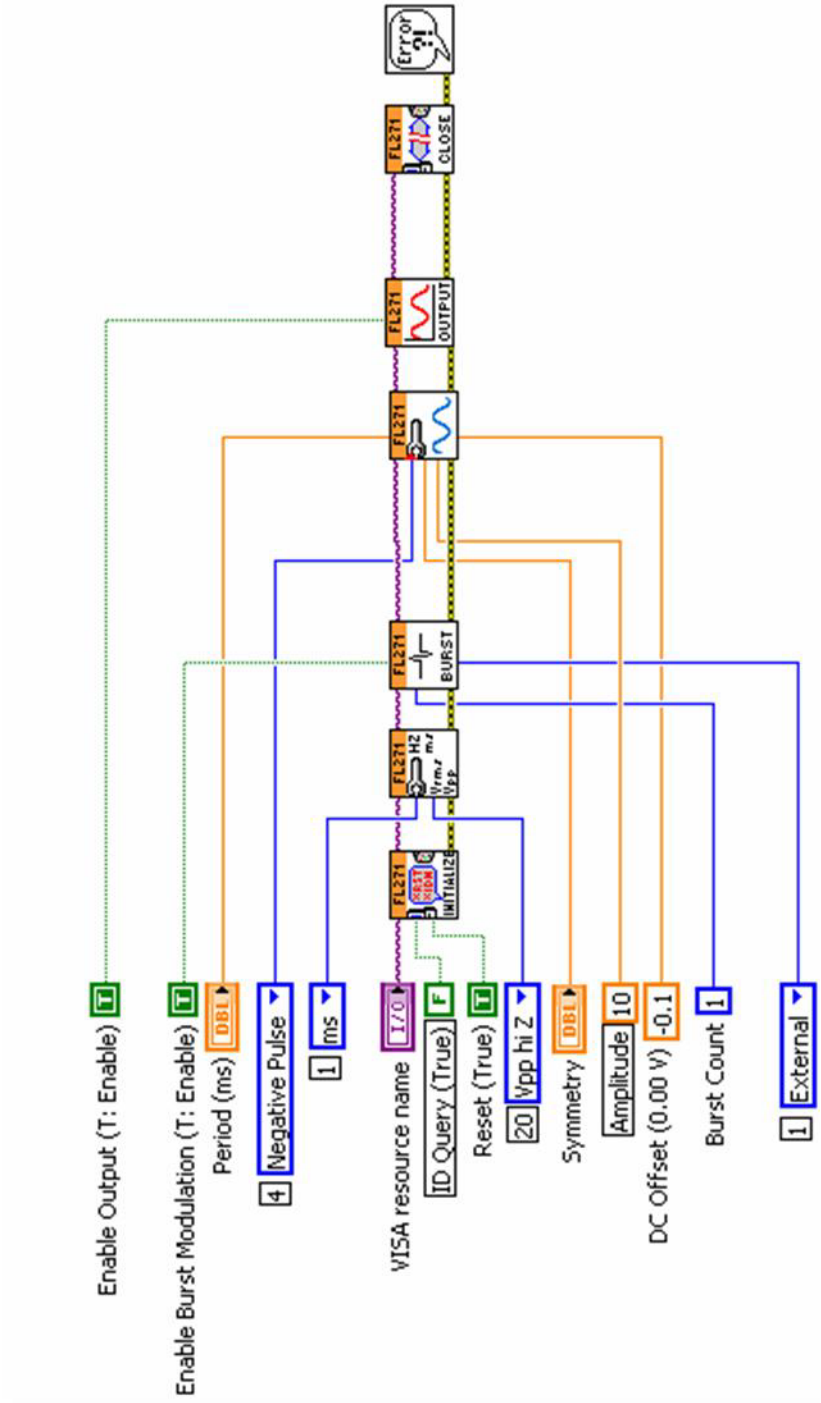

Name: Generate Trigger VI_MS.vi

Connector:

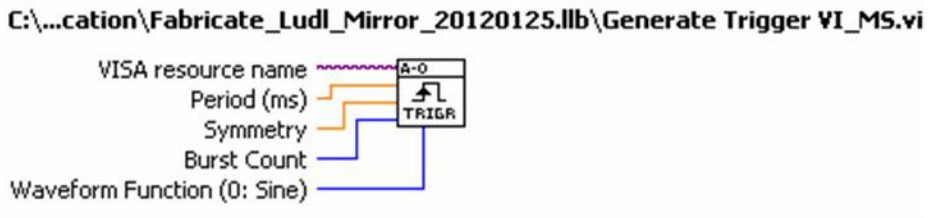

Embedded VIs: none (manufacturer drivers)

Front Panel:

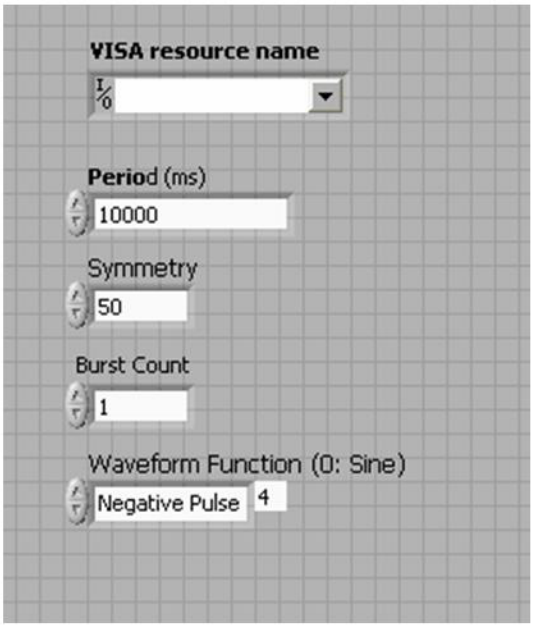

Block Diagram:

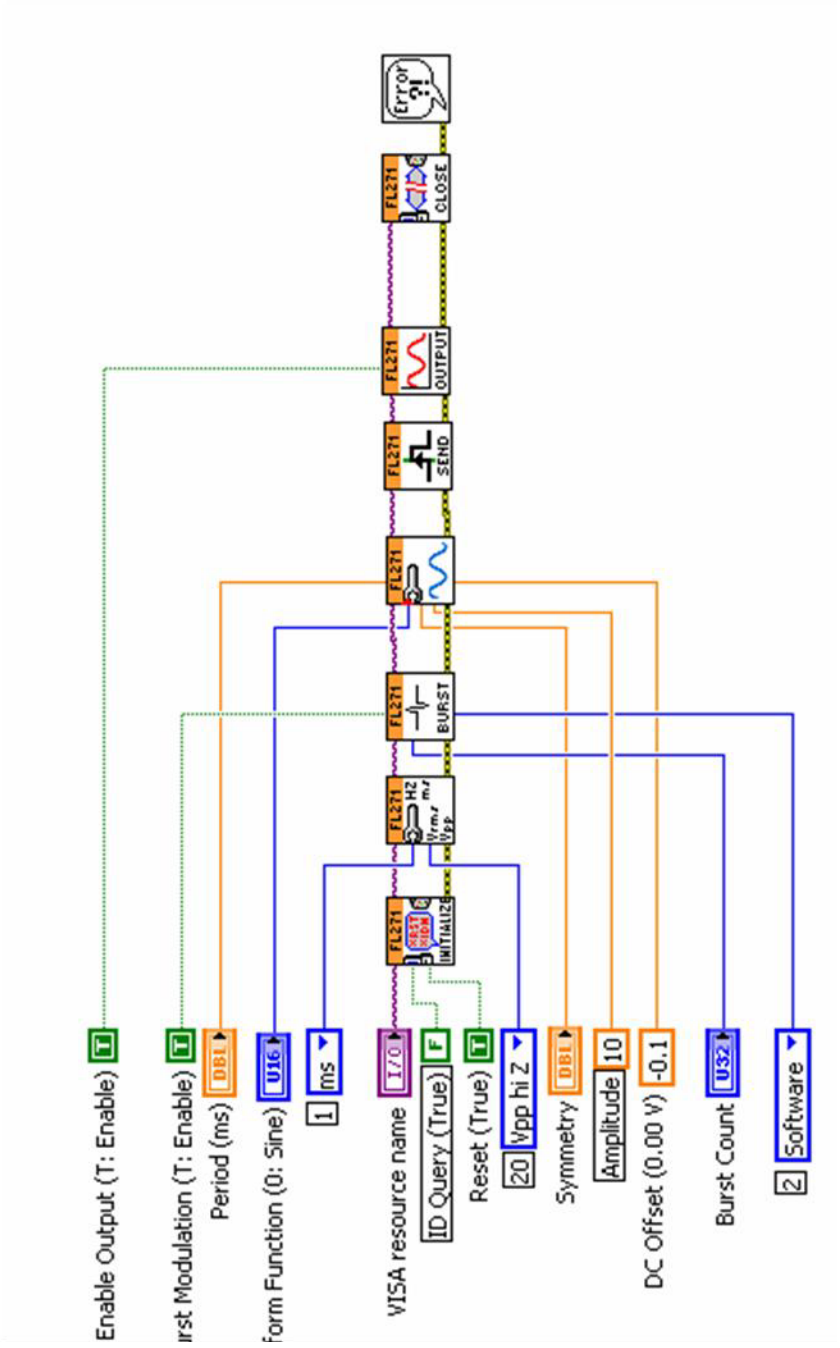

Name: AO Burst VI_MS_2AO.vi

Connector:

Embedded VIs: none (manufacturer drivers)

Front Panel:

Block Diagram:

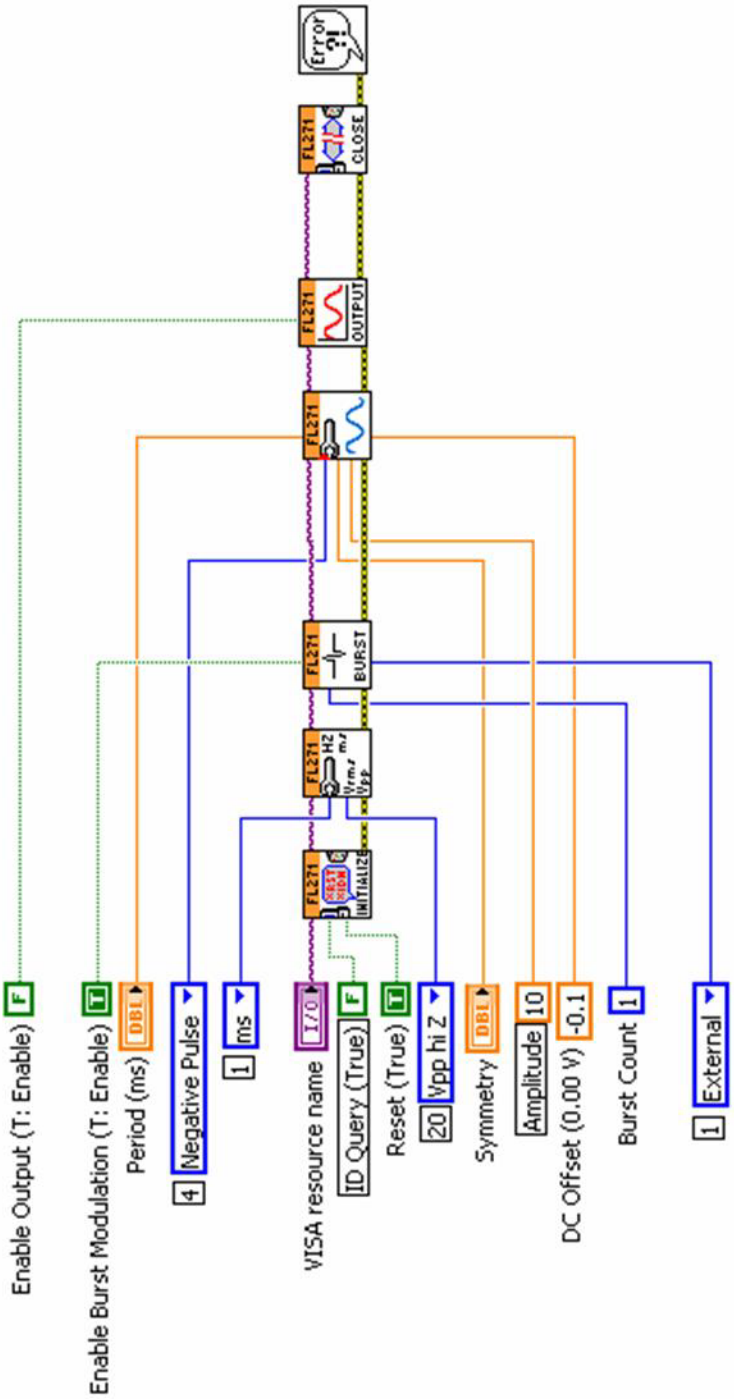

Name: Output OFF VI_MS.vi

Connector:

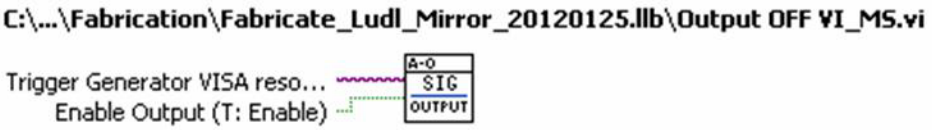

Embedded VIs: none (manufacturer drivers)

Front Panel:

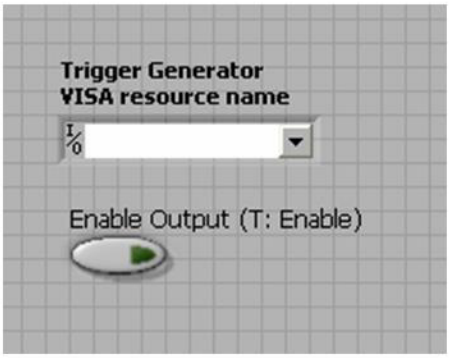

Block Diagram:

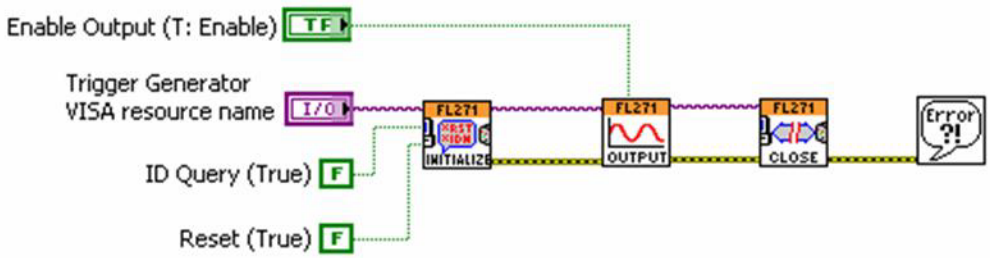

Name: File to commands Ludl with A-O Setup.vi

Embedded VIs:

C:\...op\Fabrication\Fabricate_Ludl_Mirror_20120125.llb\AO Burst VI_MS.vi

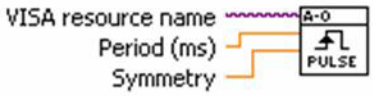

C:\...cation\Fabricate_Ludl_Mirror_20120125.llb\Generate Trigger VI_MS.vi

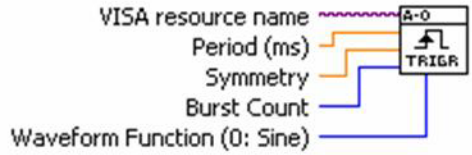

C:\...\Fabrication\Fabricate_Ludl_Mirror_20120125.llb\Output OFF VI_MS.vi

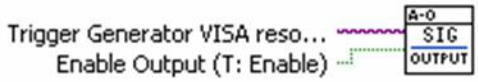

C:\...abrication\Fabricate_Ludl_Mirror_20120125.llb\AO Burst VI_MS_2AO.vi

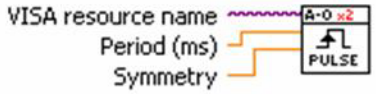

C:\...rkas Group\Desktop\Mike\LabView Programs\LUDL\Set X Acceleration.vi

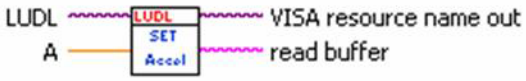

C:\...urkas Group\Desktop\Microscope\BackUp\Ludl.llb\Set Speed XY Visa.vi

C:\...s Group\Desktop\Microscope\BackUp\Ludl.llb\Relative Move XY Visa.vi

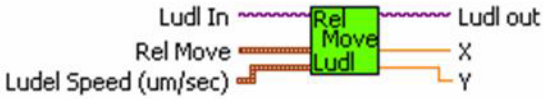

Front Panel:

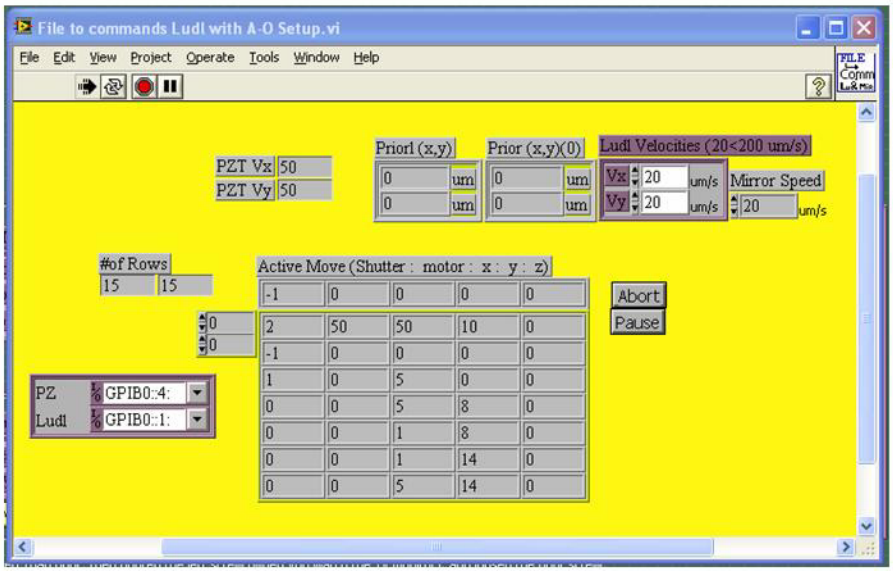
File to commands Ludl with A-O Setup.vi
File Edit View Project Operate Tools Window Help
PZT Vx 50
PZT Vy 50
Priorl (x,y)
Prior (x,y)(0)
Ludl Velocities (20<200 um/s)
Vx 20 um/s
Vy 20 um/s
Mirror Speed 20 um/s
#of Rows
15 15
Active Move (Shutter : motor : x : y : z)
Abort
Pause
PZ GPIB0::4:
Ludl GPIB0::1:

Block Diagram:

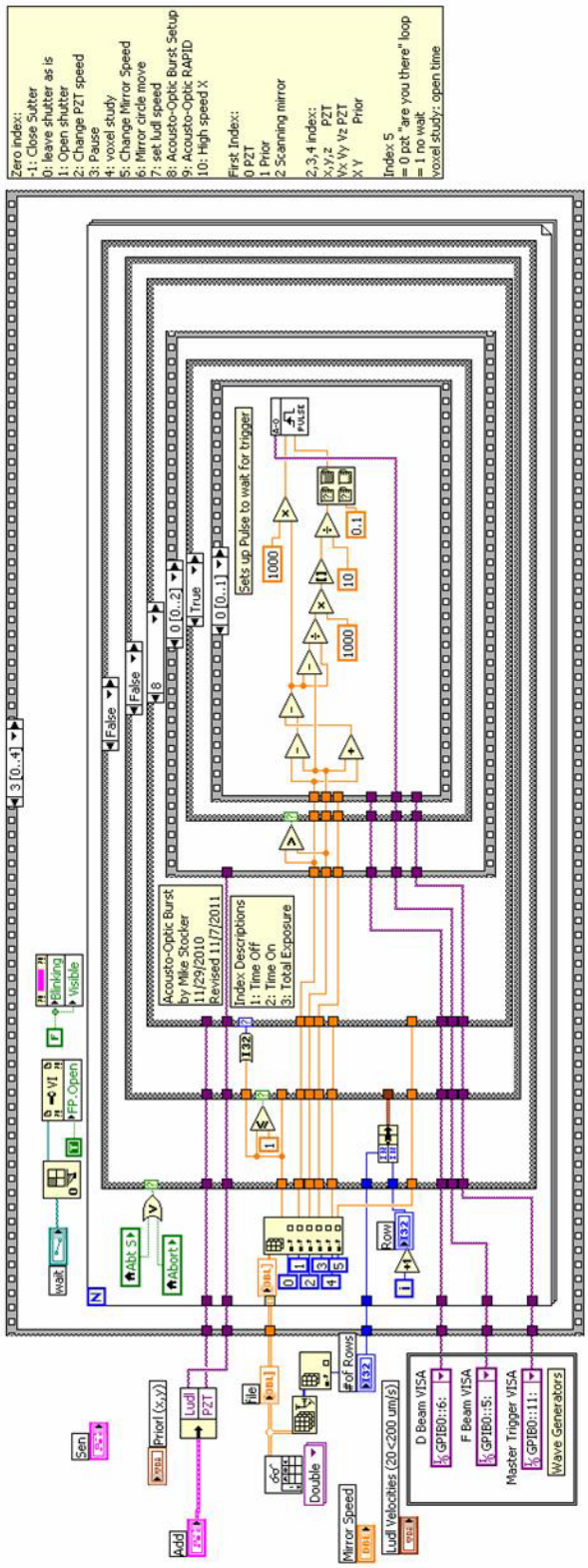

Block Diagram:

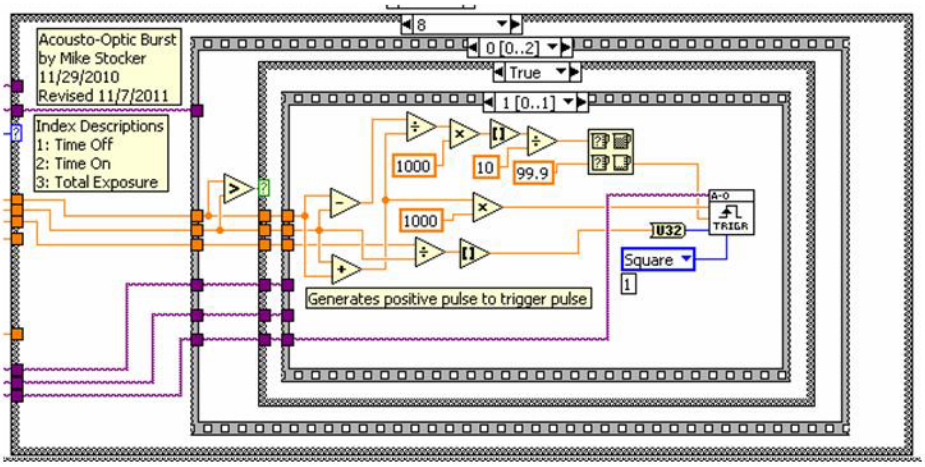

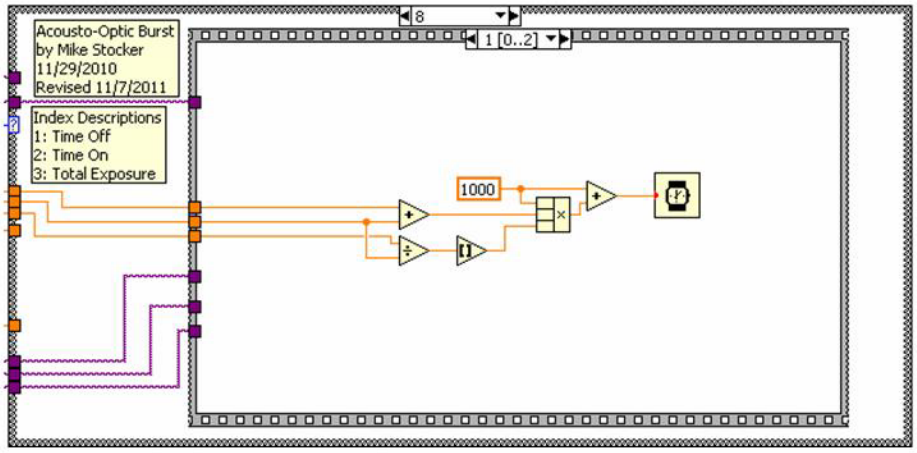

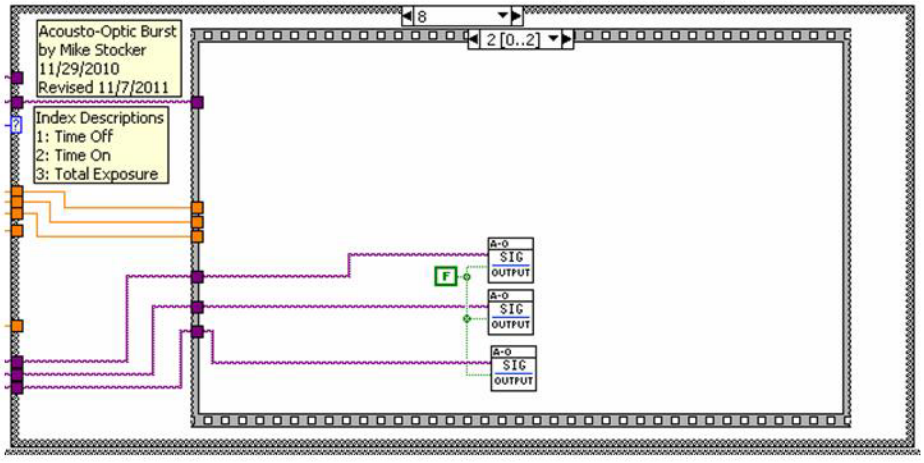

Block Diagram:

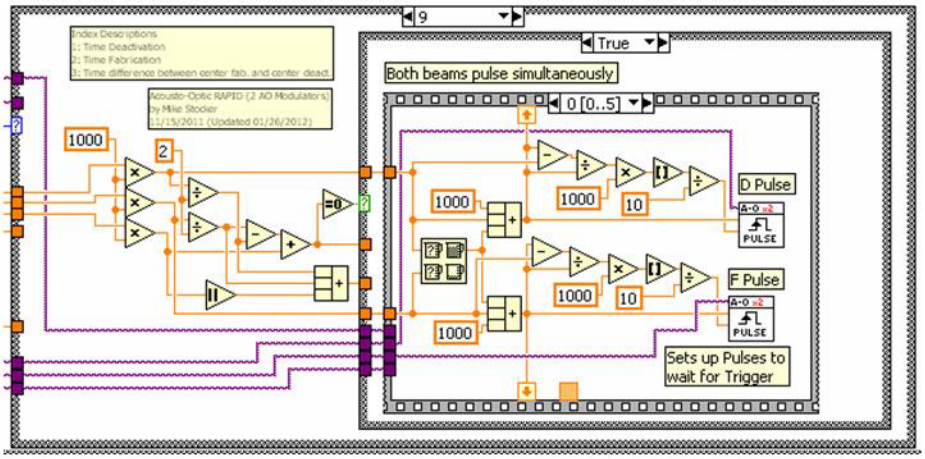

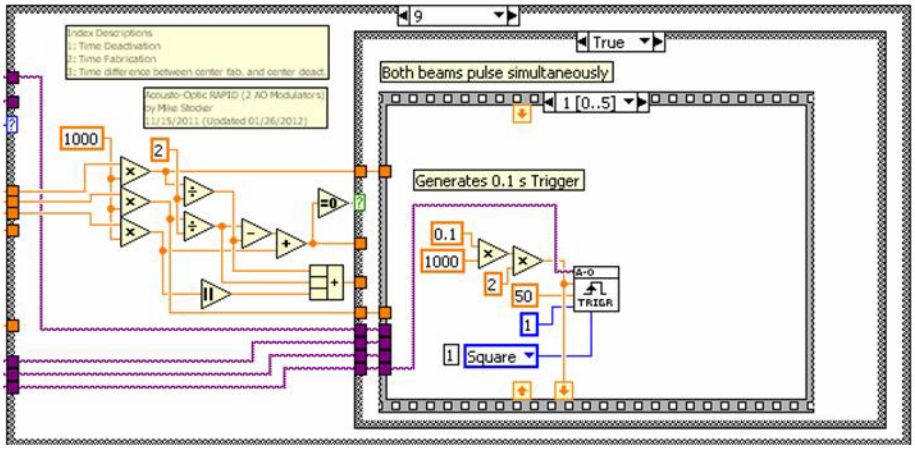

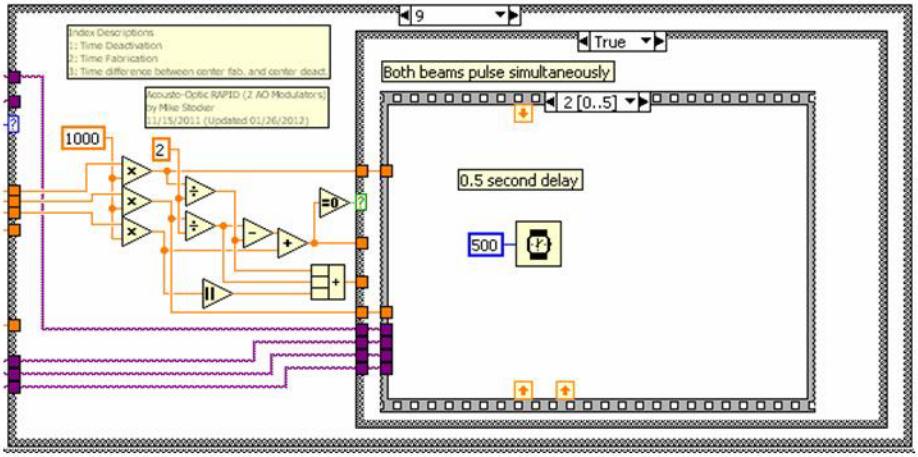

Block Diagram:

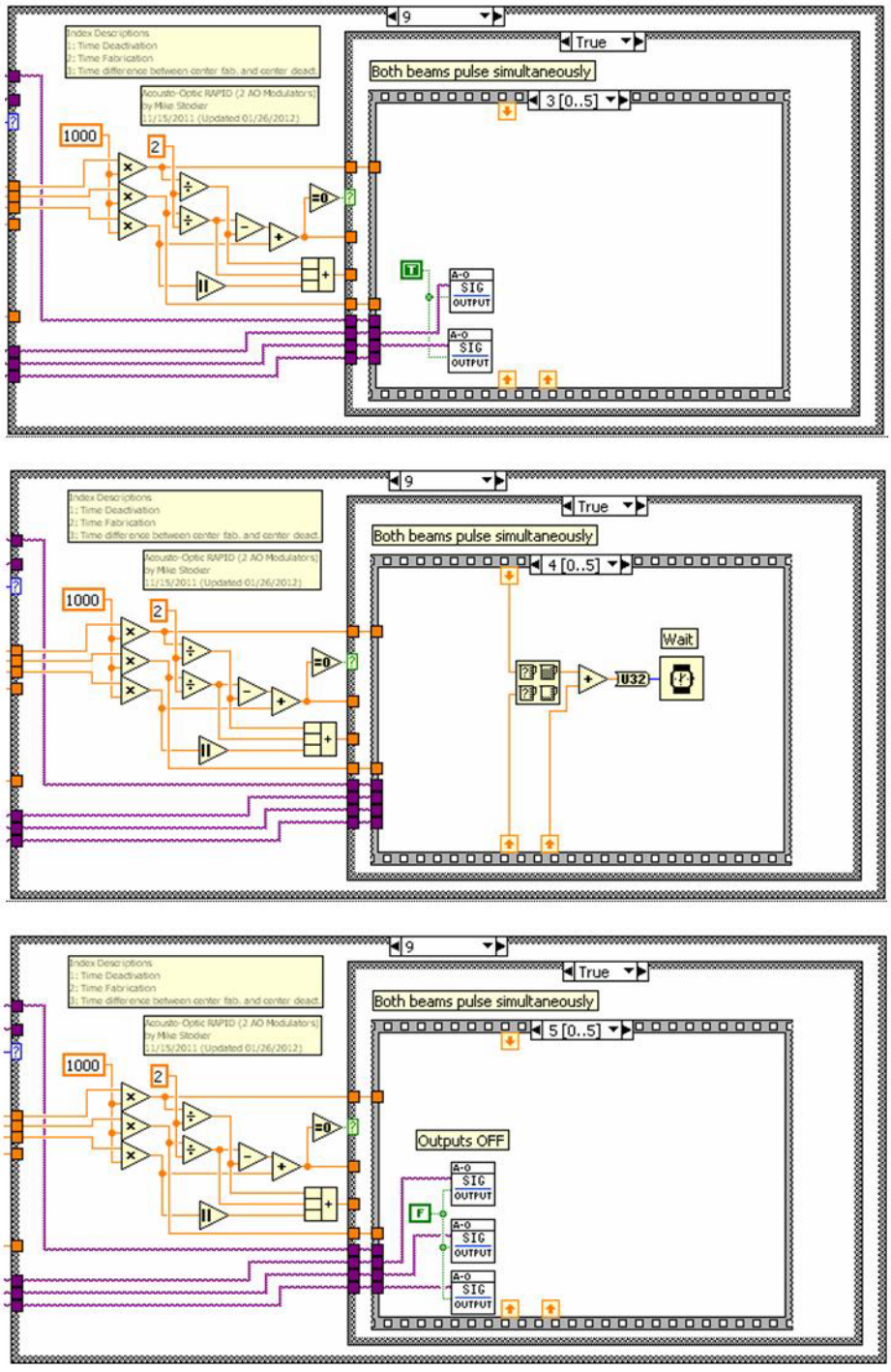

Block Diagram:

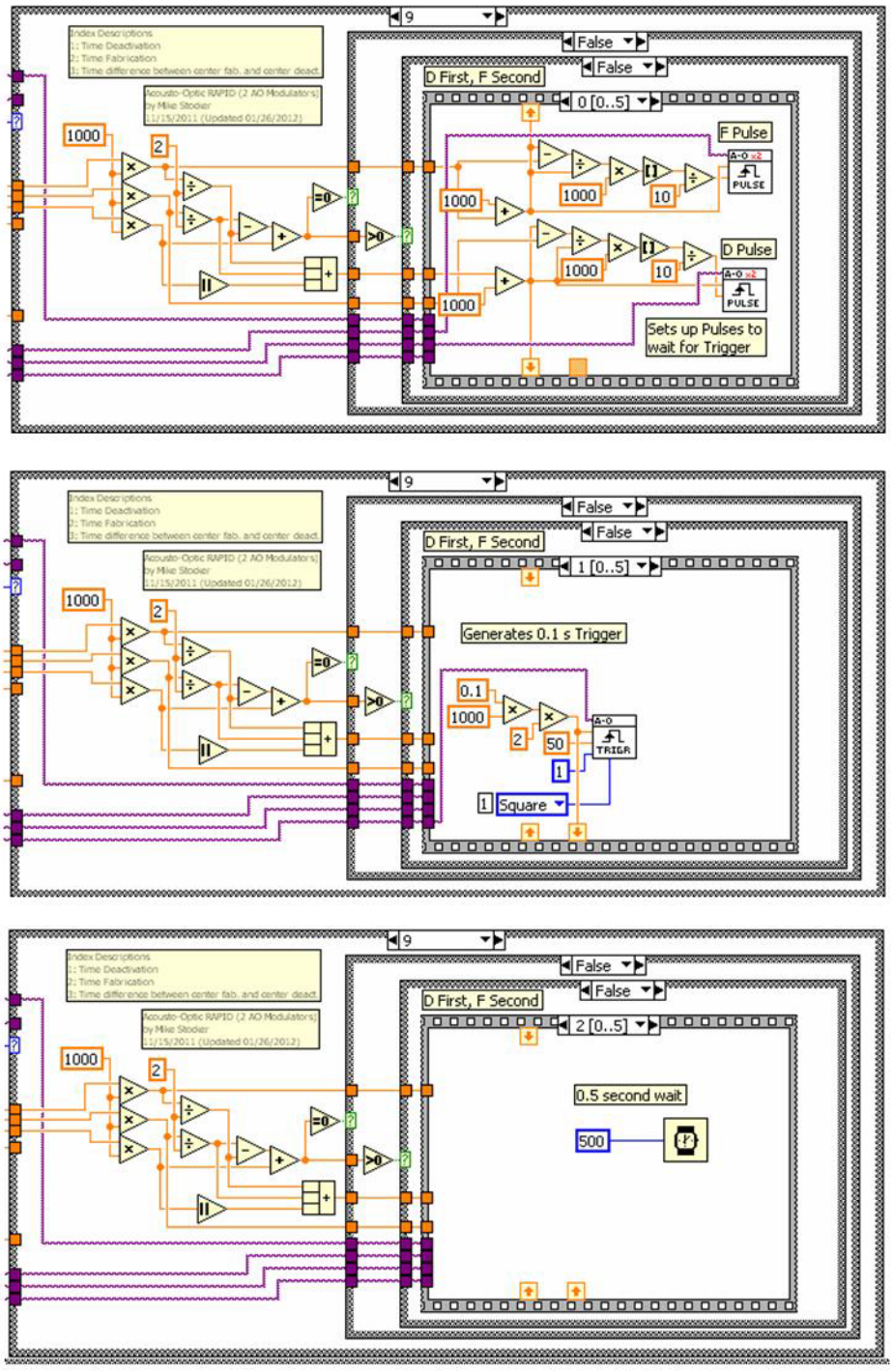

Block Diagram:

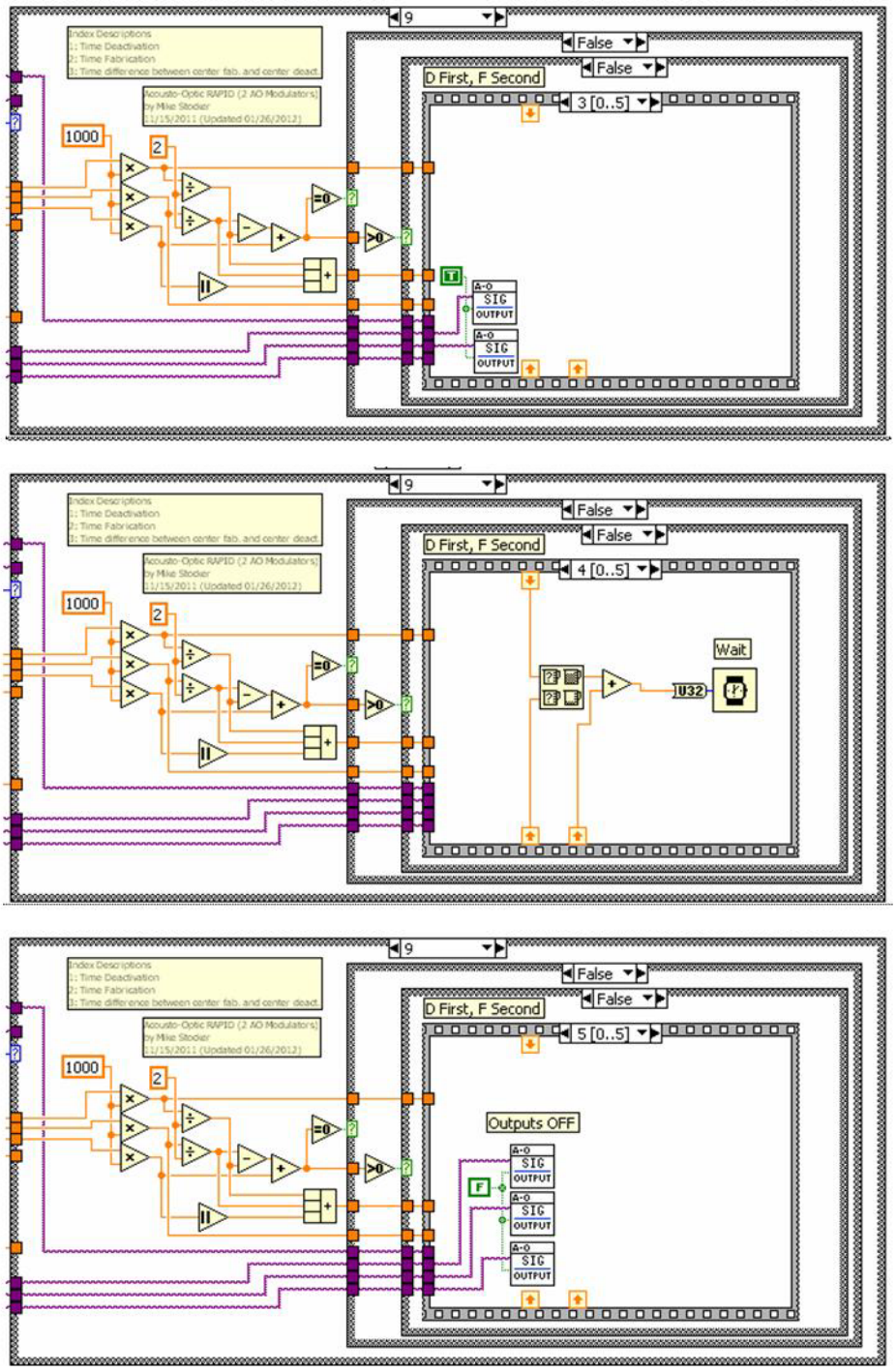

Block Diagram:

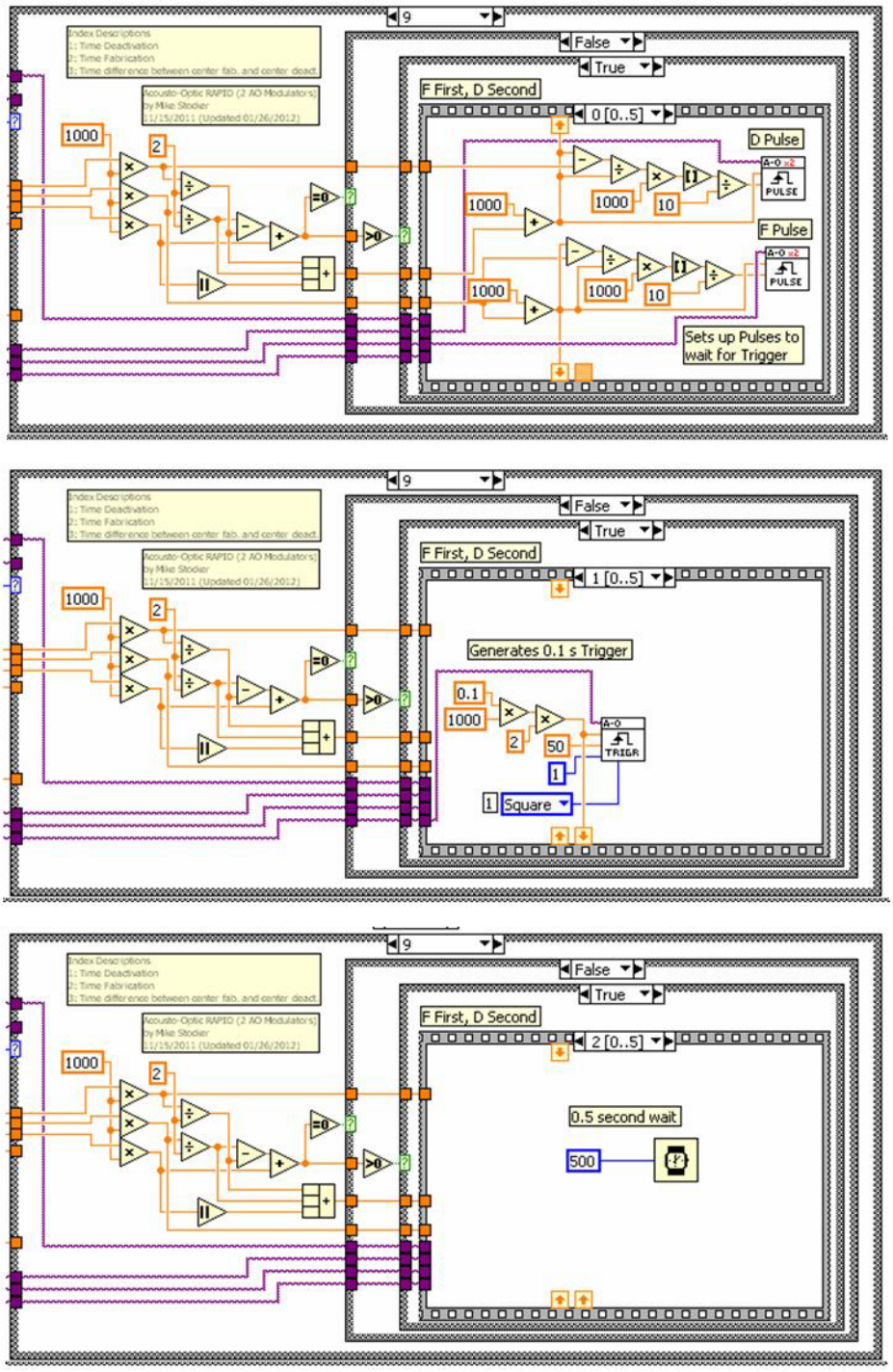

Block Diagram:

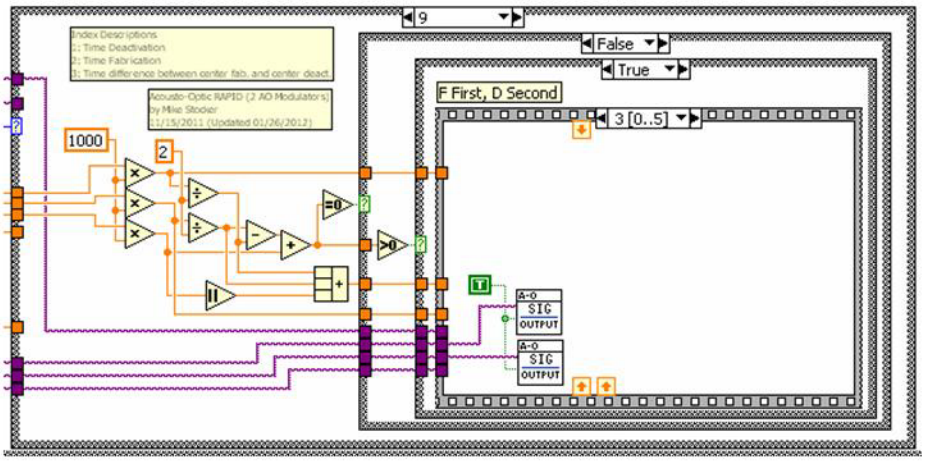

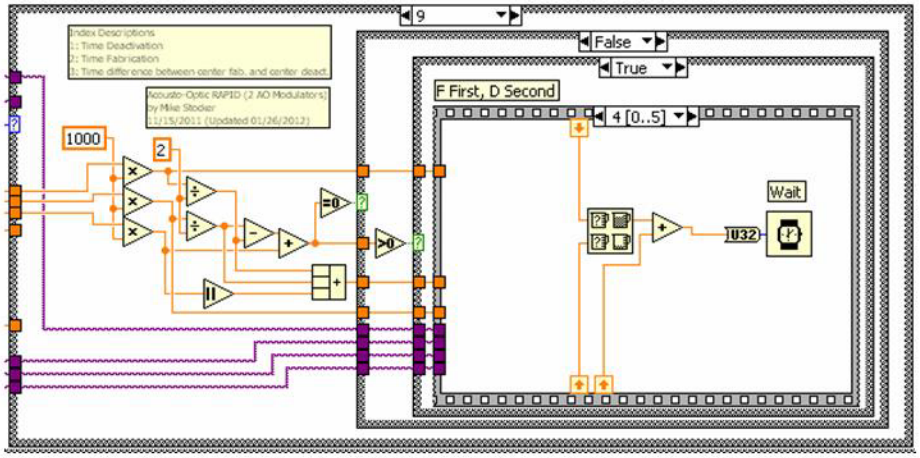

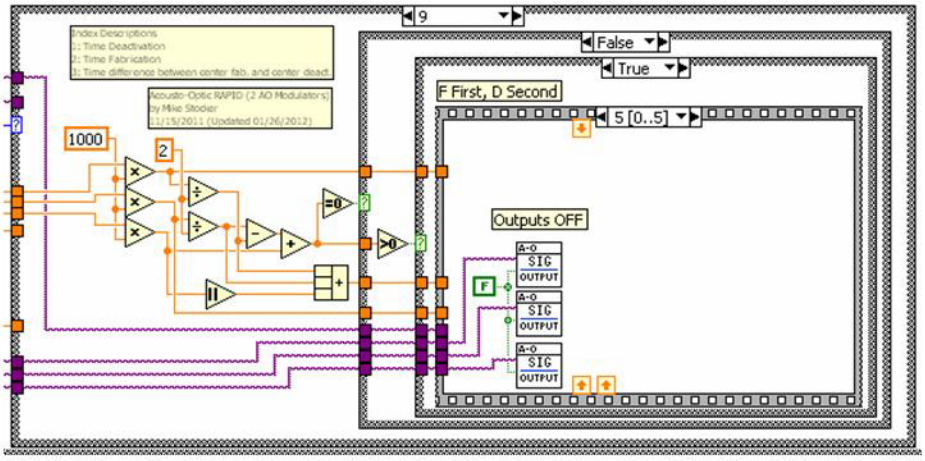

Block Diagram:

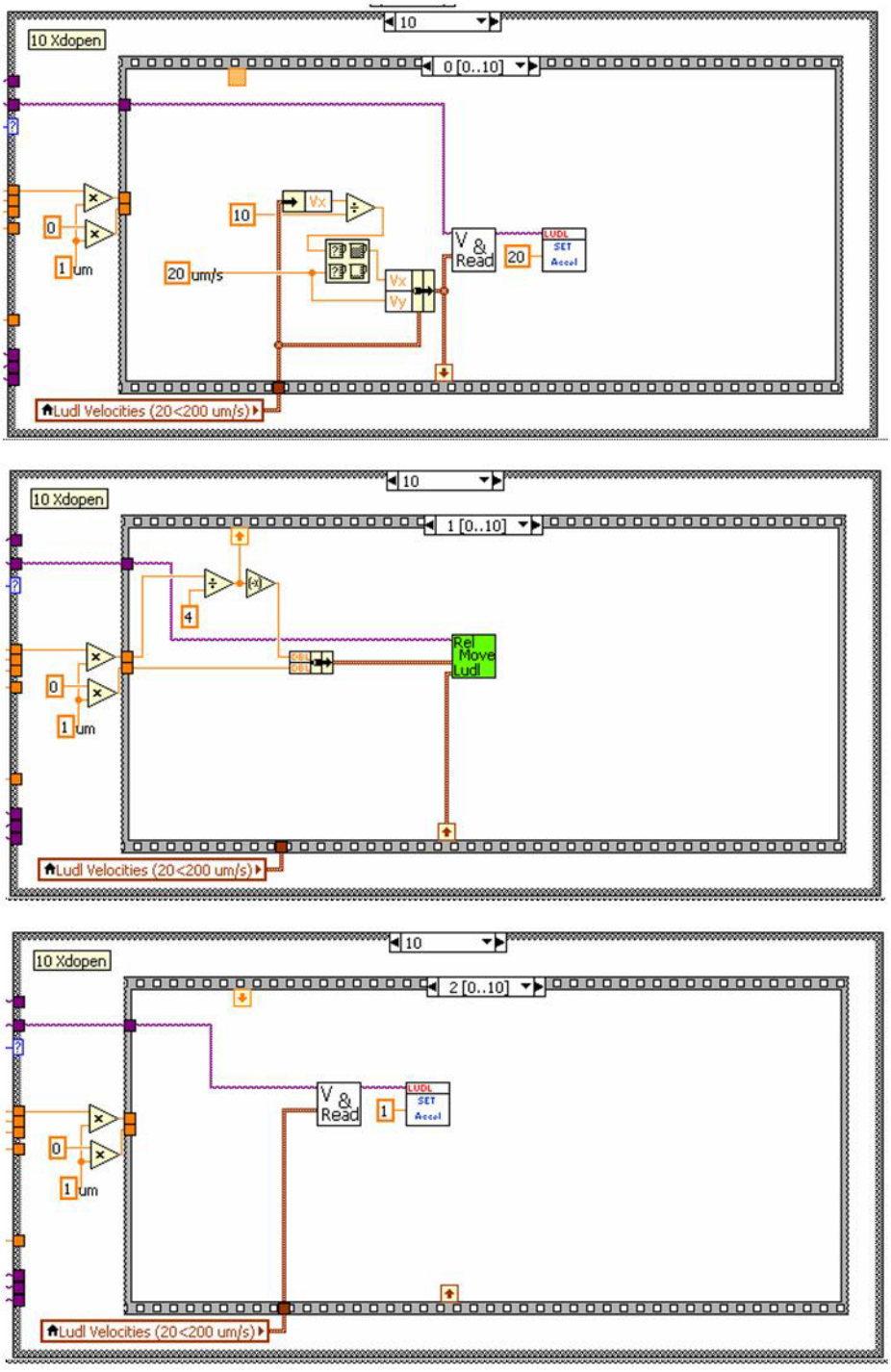

Block Diagram:

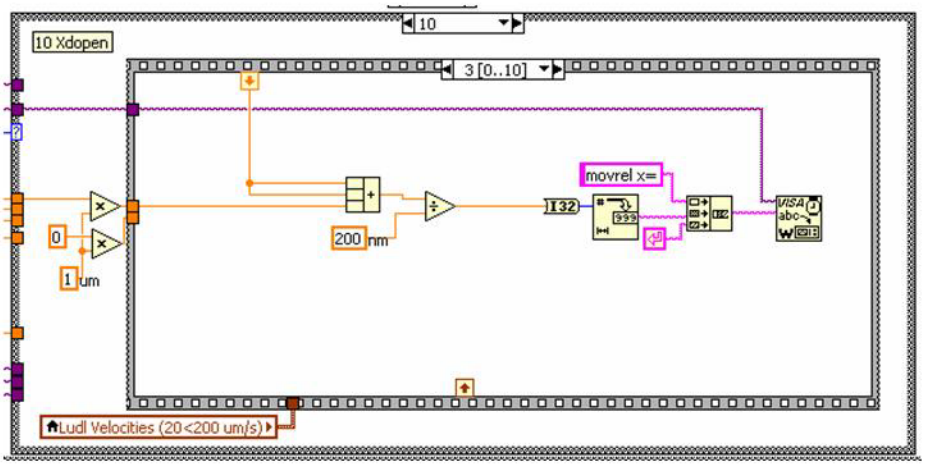

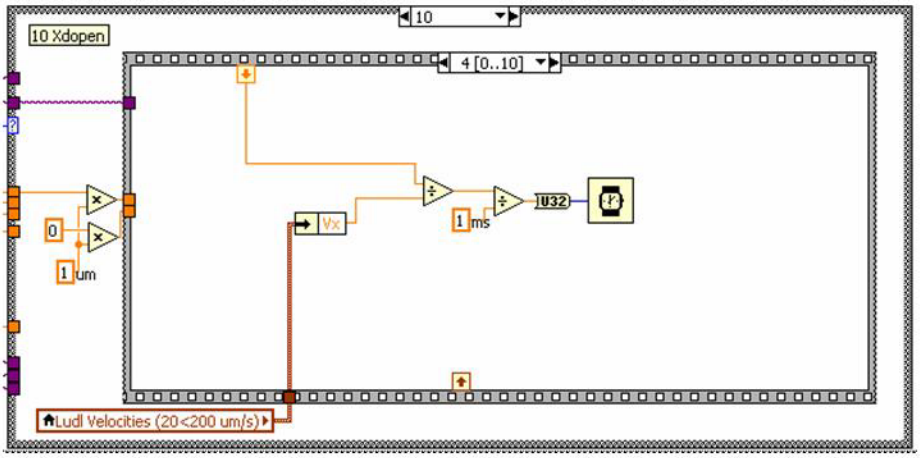

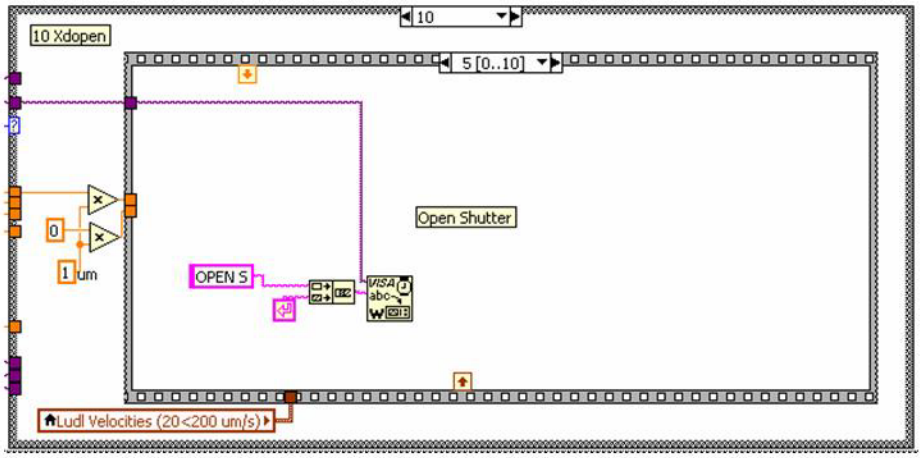

Block Diagram:

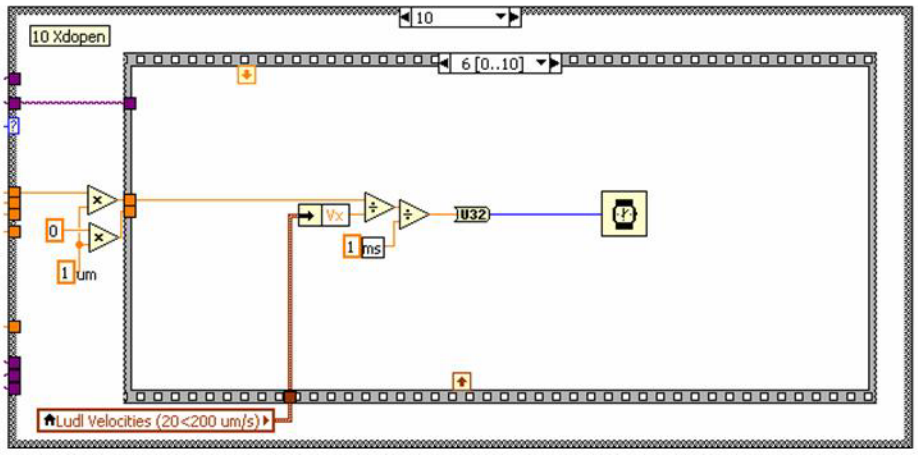

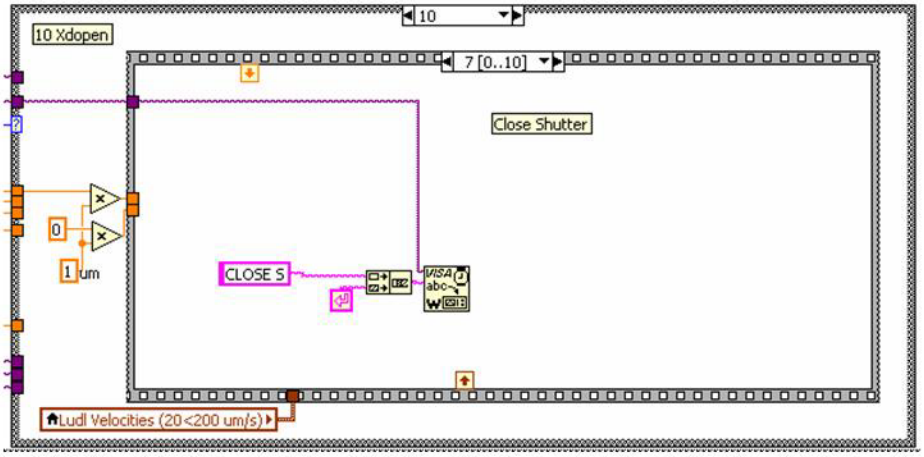

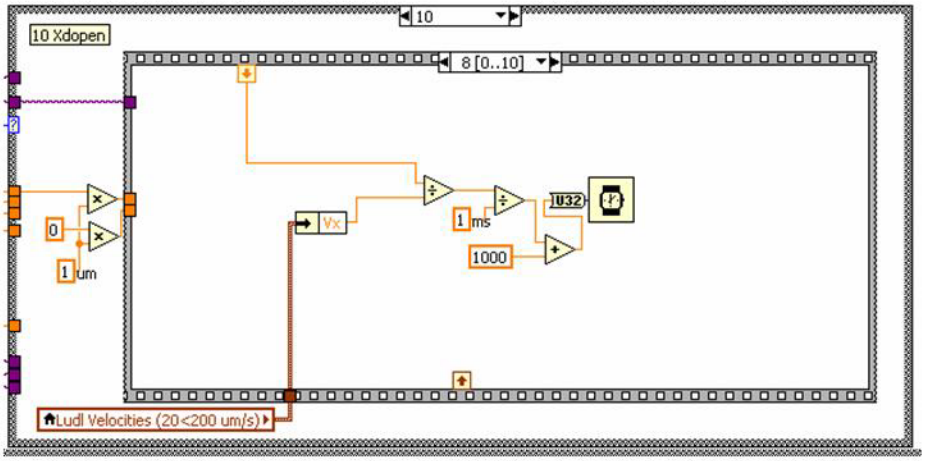

Block Diagram:

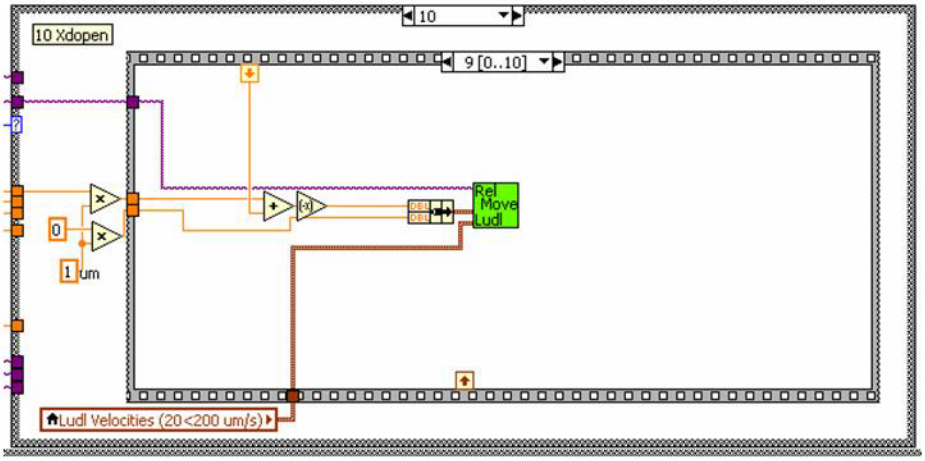

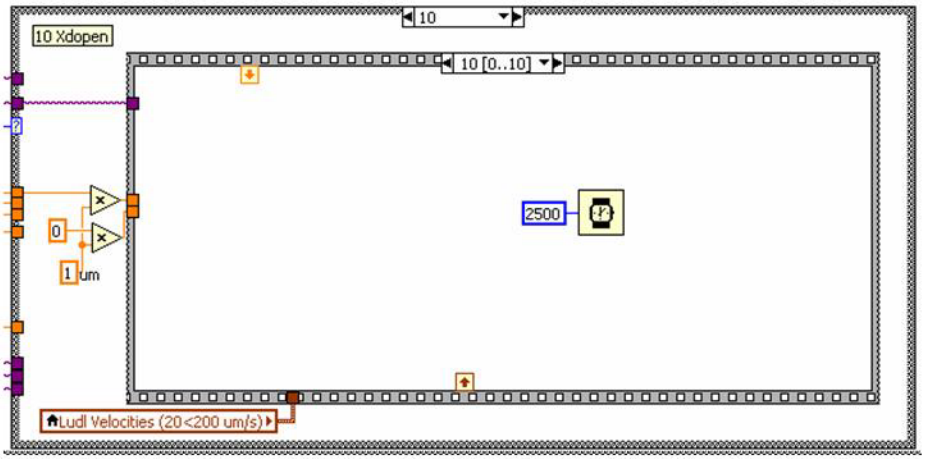

Name: Moving Mirrors Calculation_MS_subVI.vi

Connector:

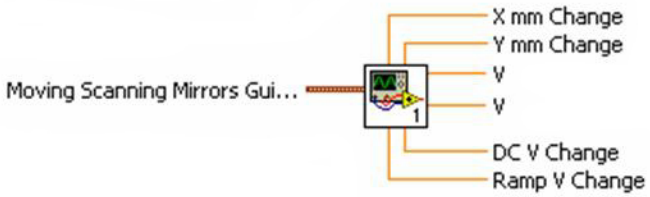

Embedded VIs: none

Front Panel:

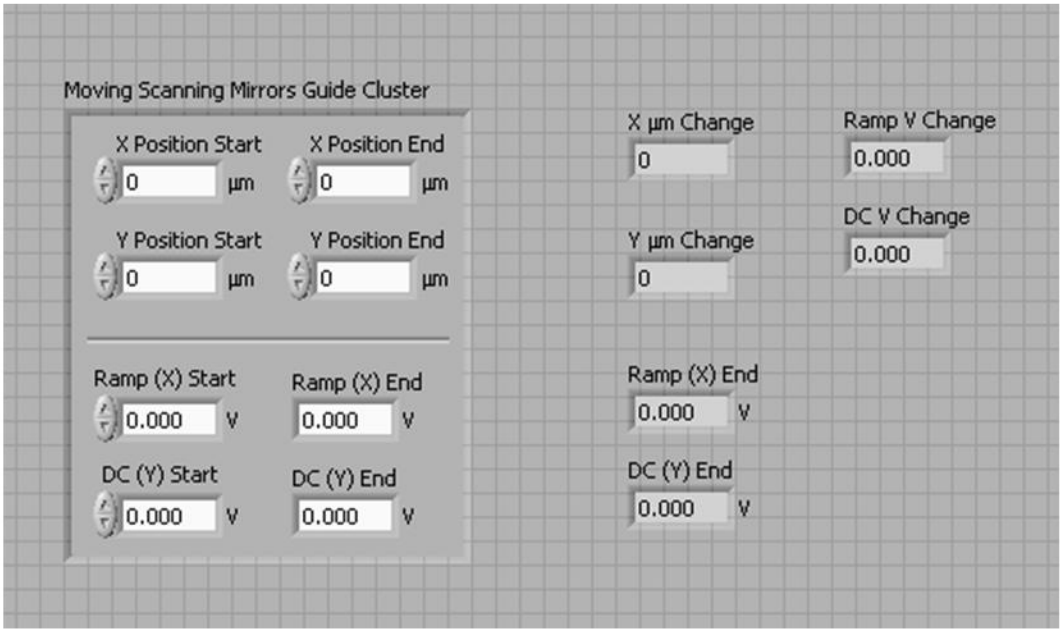

Block Diagram:

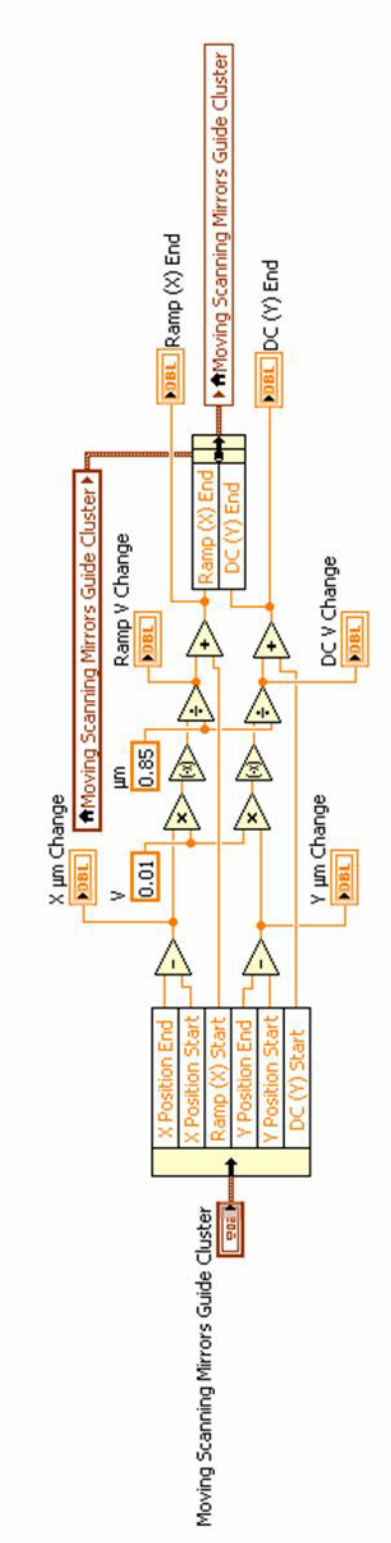

Name: PZT Scan_Only.vi

Connector:

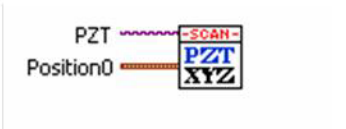

Embedded VIs:

C:\...ktop\Microscope\PZT VISA_MS_071111.llb\InI Servo Control Visa_MS.vi

C:\...\Desktop\Microscope\BackUp\PZT VISA.llb\Move Abs XYZ Visa & wait.vi

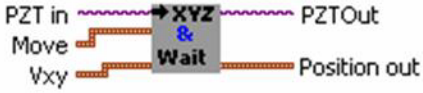

C:\...roup\Desktop\LabView\Drivers\PZT VISA.llb\Read Position xyz Visa.vi

C:\...sktop\Microscope\PZT VISA_MS_071111.llb\Set XYZ Velocity Visa_MS.vi

C:\...ettings\Fourkas Group\Desktop\Microscope\Microscope.llb\InI Vout.vi

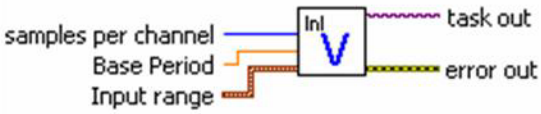

C:\...ings\Fourkas Group\Desktop\Microscope\Microscope.llb\InI Counter.vi

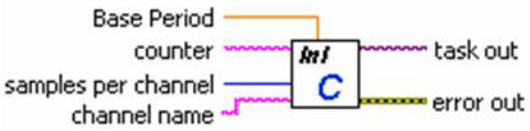

Embedded VIs:

C:\...d Settings\Fourkas Group\Desktop\Microscope\Microscope.llb\Run V.vi

C:\...ings\Fourkas Group\Desktop\Microscope\Microscope.llb\Run Counter.vi

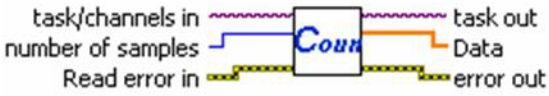

C:\...urkas Group\Desktop\Microscope\BackUp\PZT VISA.llb\Wait XYZ Visa.vi

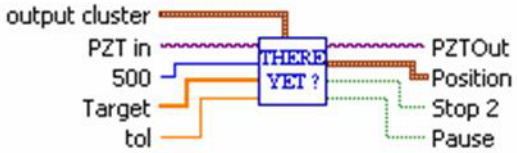

C:\...nd Settings\Fourkas Group\Desktop\Microscope\Microscope.llb\Stat.vi

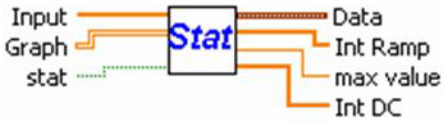

C:\...ope\Microscope_MS_012612.llb\Moving Mirrors Calculation_MS_subVI.vi

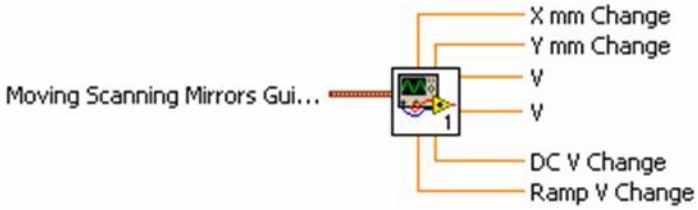

Front Panel:

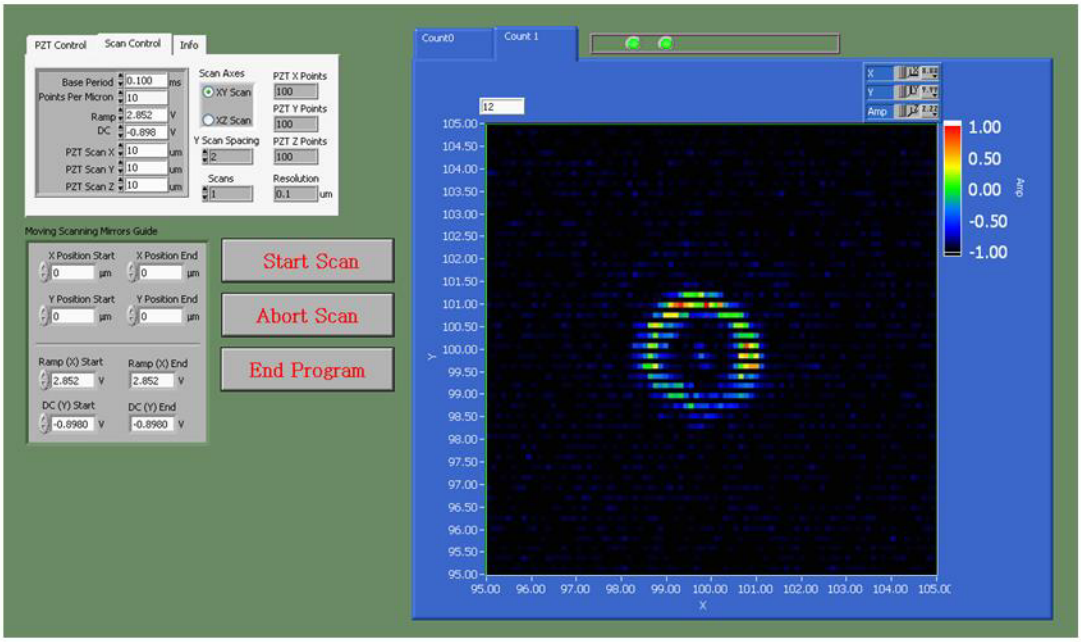
PZT Control
Scan Control
Info
Base Period
Points Per Micron
Ramp
DC
PZT Scan X
PZT Scan Y
PZT Scan Z
Scan Axes
XY Scan
XZ Scan
Y Scan Spacing
Scans
PZT X Points
PZT Y Points
PZT Z Points
Resolution
Moving Scanning Mirrors Guide
X Position Start
X Position End
Y Position Start
Y Position End
Ramp (X) Start
Ramp (X) End
DC (Y) Start
DC (Y) End
Start Scan
Abort Scan
End Program
Count0
Count 1
Amp
1.00
0.50
0.00
-0.50
-1.00

Block Diagram:

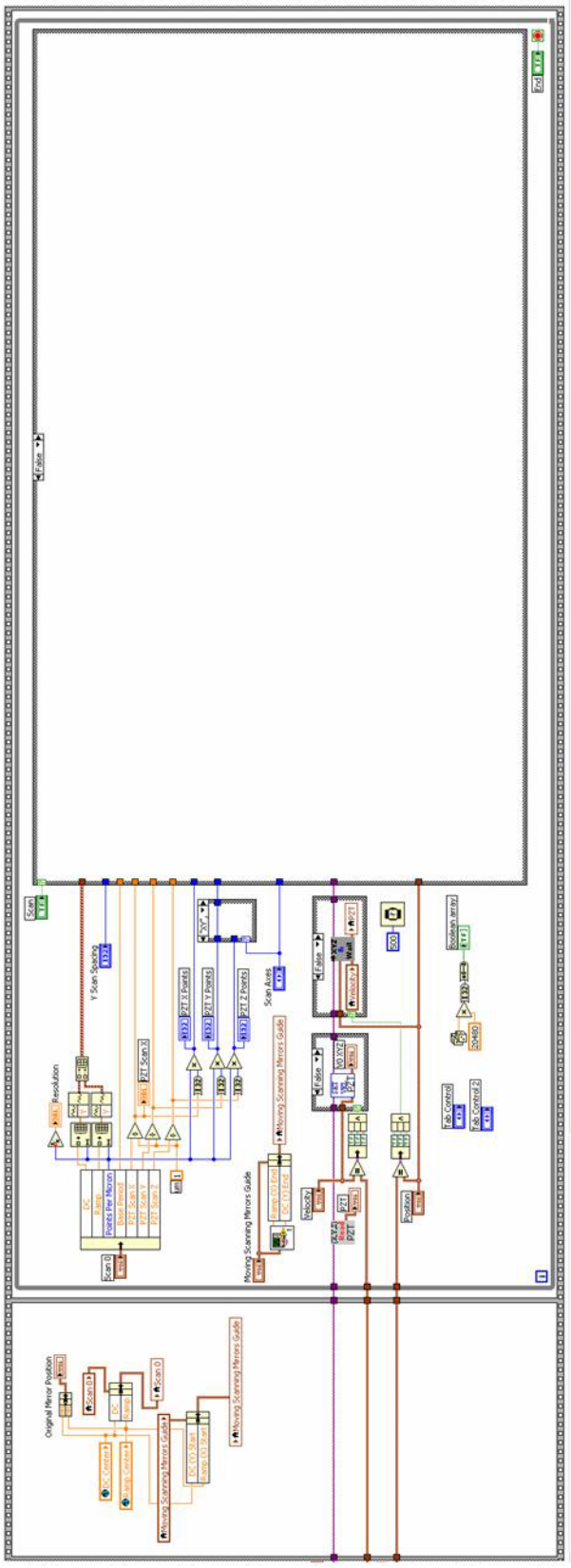

Block Diagram:

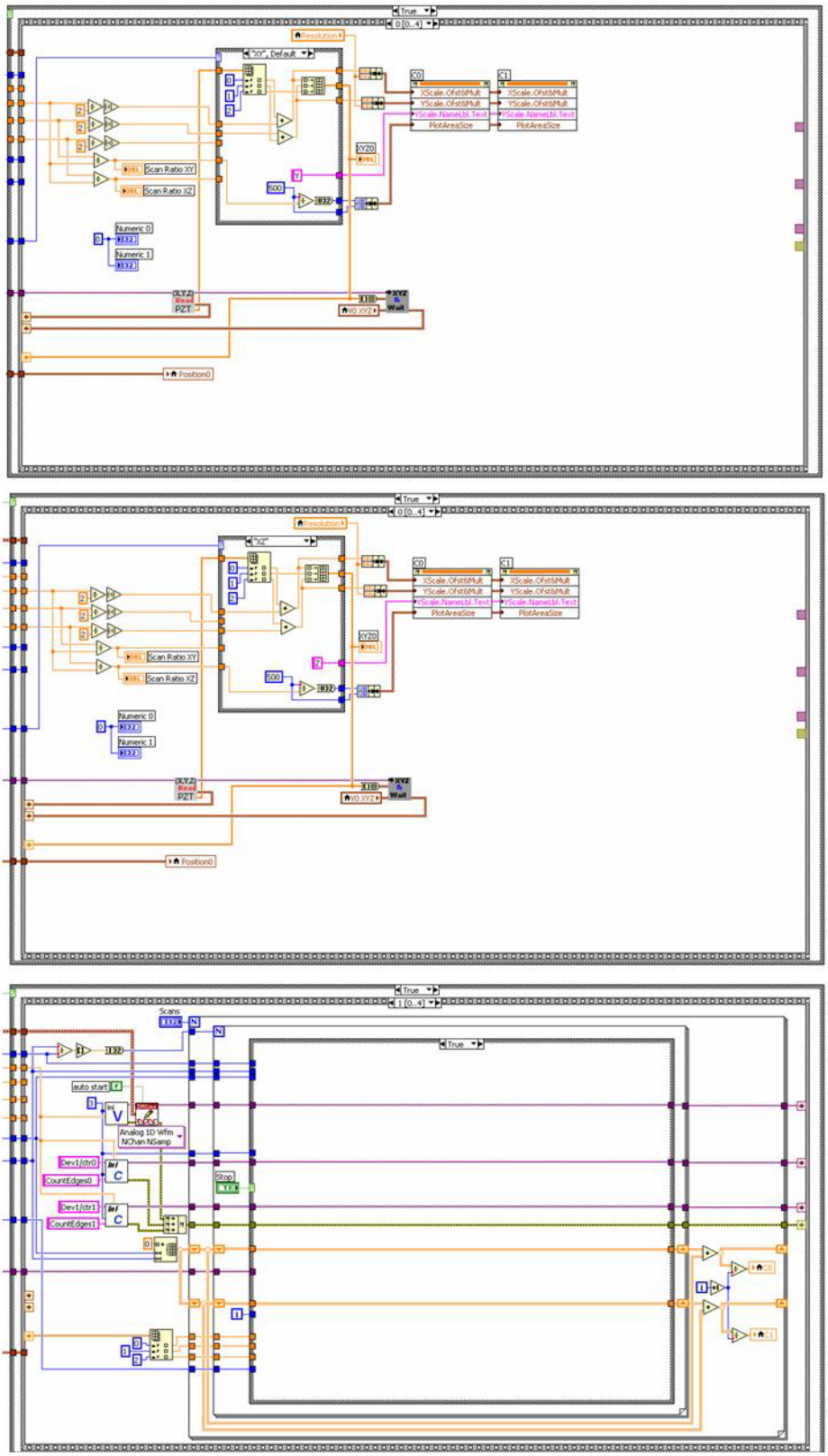

Block Diagram:

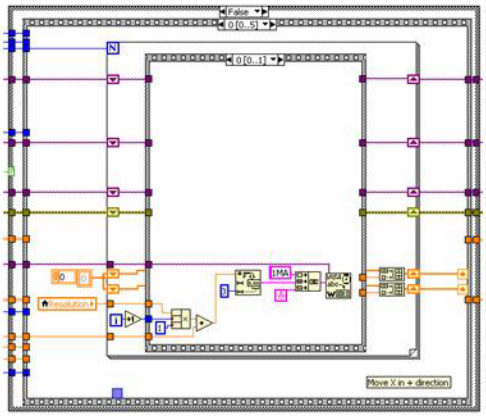

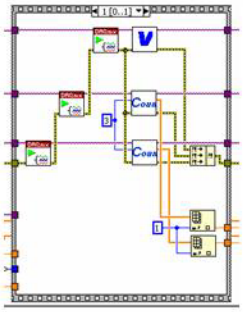

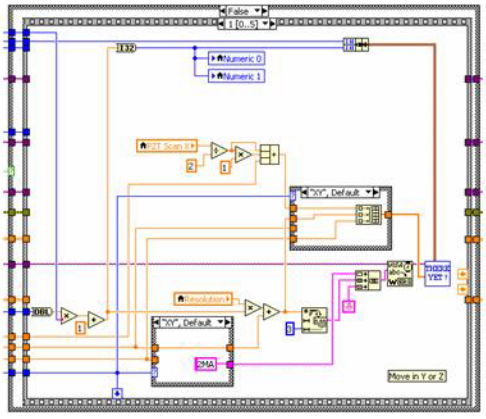

Block Diagram:

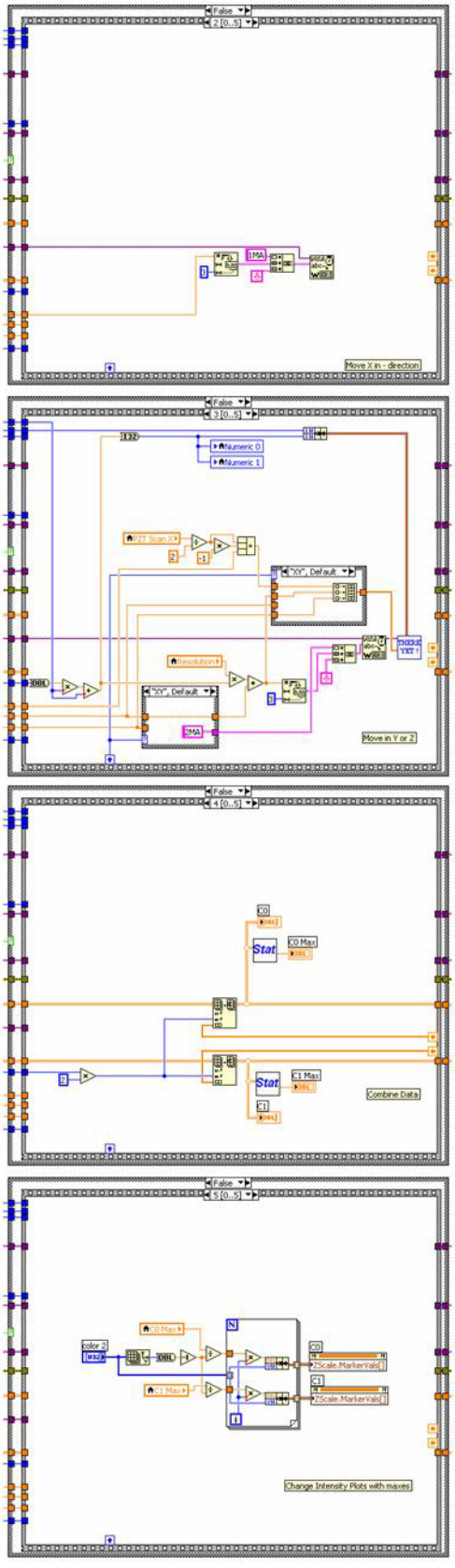

Block Diagram:

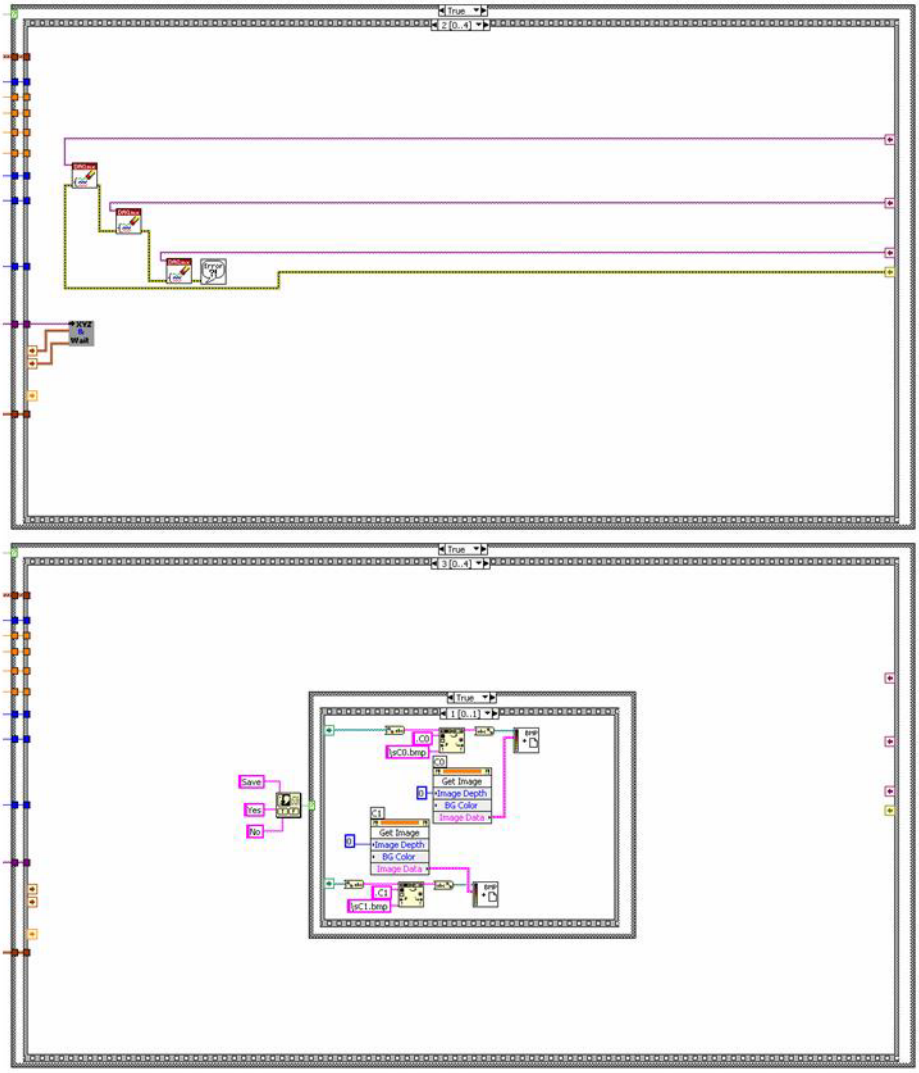

Appendix B: Longpass Filter Transmission Spectra

These filters are used under the microscope illumination source to prevent undesired photopolymerization.

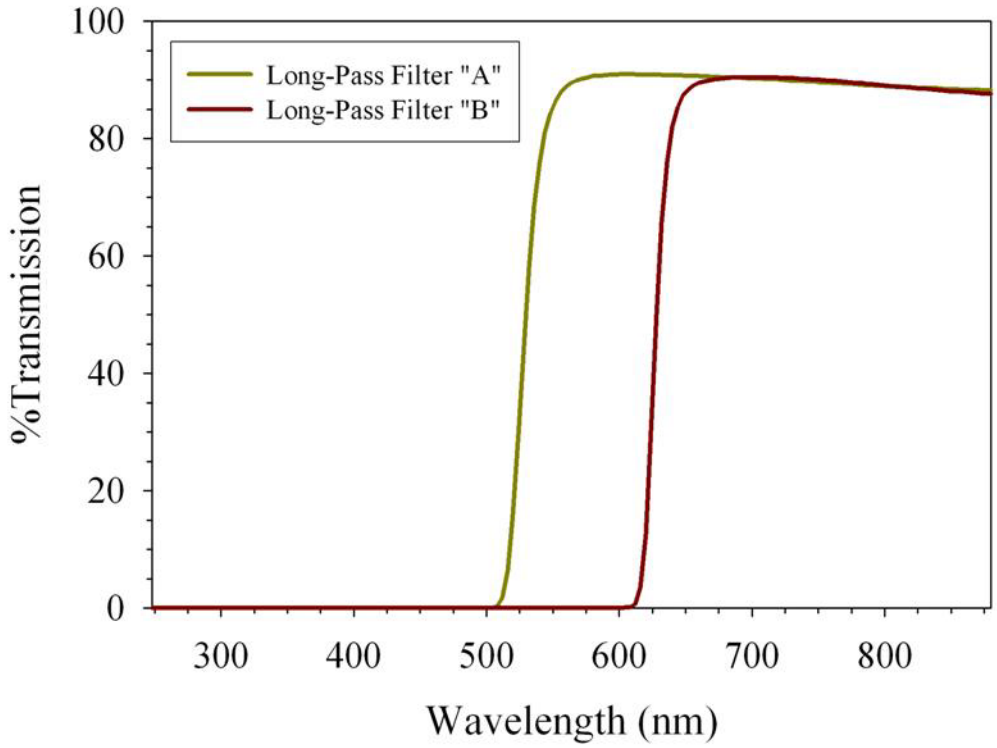

Appendix C: Complete Laser Table Setup

This diagram is an approximation of the optical systems on the laser table at the time of writing (5/2012).

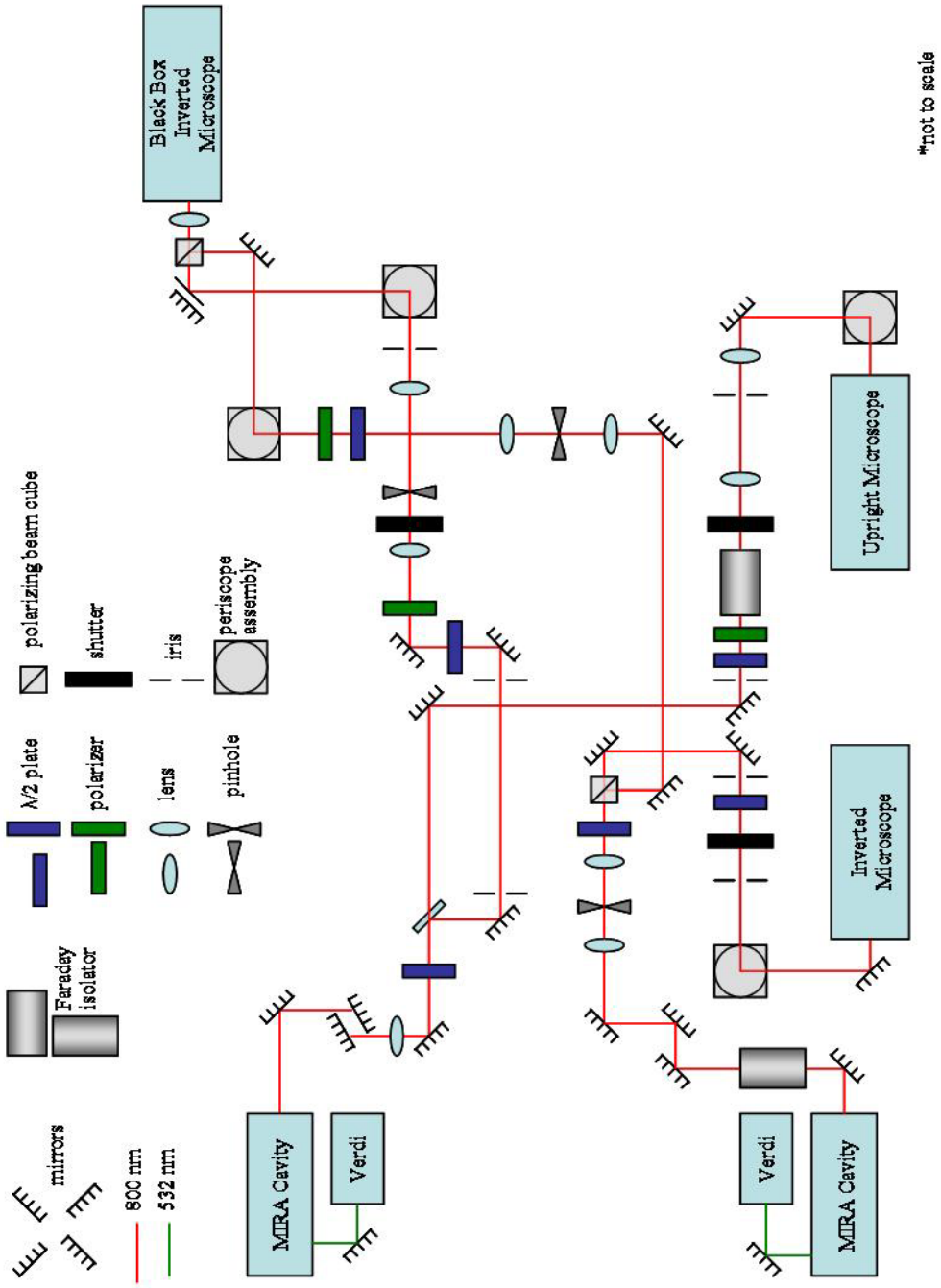

References:

(1) Andrew, T. L.; Tsai, H.-Y.; Menon, R., Confining Light to Deep Subwavelength Dimensions to Enable Optical Nanopatterning. *Science* **2009,** 324, (5929), 917-921.

(2) Baldacchini, T.; LaFratta, C. N.; Farrer, R. A.; Teich, M. C.; Saleh, B. E. A.; Naughton, M. J.; Fourkas, J. T., Acrylic-based resin with favorable properties for three-dimensional two-photon polymerization. *Journal of Applied Physics* **2004,** 95, (11), 6072-6076.

(3) Bangert, R.; Aichele, W.; Schollmeyer, E.; Weimann, B.; Herlinger, H., Photooxidation of Malachite Green and Crystal Violet. *Melliand Textilberichte International Textile Reports* **1977,** 58, (5), 399-404.

(4) Bayindir, Z.; Sun, Y.; Naughton, M. J.; LaFratta, C. N.; Baldacchini, T.; Fourkas, J. T.; Stewart, J.; Saleh, B. E. A.; Teich, M. C., Polymer microcantilevers fabricated via multiphoton absorption polymerization. *Applied Physics Letters* **2005,** 86, (6), 064105-3.

(5) Burkinshaw, S. M.; Griffiths, J.; Towns, A. D., Reversibly thermochromic systems based on pH-sensitive spirolactone-derived functional dyes. *Journal of Materials Chemistry* **1998,** 8, (12), 2677-2683.

(6) Campagnola, P. J.; Delguidice, D. M.; Epling, G. A.; Hoffacker, K. D.; Howell, A. R.; Pitts, J. D.; Goodman, S. L., 3-dimensional submicron polymerization of acrylamide by multiphoton excitation of xanthene dyes. *Macromolecules* **2000,** 33, (5), 1511-1513.

(7) Colley, C. S.; Grills, D. C.; Besley, N. A.; Jockusch, S.; Matousek, P.; Parker, A. W.; Towrie, M.; Turro, N. J.; Gill, P. M. W.; George, M. W., Probing the reactivity of photoinitiators for free radical polymerization: Time-resolved infrared spectroscopic study of benzoyl radicals. *Journal of the American Chemical Society* **2002,** 124, (50), 14952-14958.

(8) Connell, J. L. W., Aimee K.; Parsek, Matthew R.; Ellington, Andrew D.; Whiteley, Marvin; Shear, Jason B., Probing Prokaryotic Social Behaviors with Bacterial "Lobster Traps". *mBio* **2010,** 1, e00202-00210.

(9) Dawood, F. Q., Sijia; Li, Linjie; Lin, Emily; Fourkas, John T., Simultaneous Microscale Manipulation, Immobilization, and Fabrication in Aqueous Media. *Chemical Science* **2012,** in review.

(10) Diaspro, A.; Bianchini, P.; Vicidomini, G.; Faretta, M.; Ramoino, P.; Usai, C., Multi-photon excitation microscopy. *BioMedical Engineering OnLine* **2006,** 5, 36-1-14.

(11) Driscoll, M. K.; Fourkas, J. T.; Losert, W., Local and global measures of shape dynamics. *Physical Biology* **2011,** 8, (5), 055001-1-9.

(12) Driscoll, M. K.; Kopace, R.; Li, L.; McCann, C.; Watts, J.; Fourkas, J. T.; Losert, W., The adventures of Dicty, the Dictyostelium cell. *Chaos: An Interdisciplinary Journal of Nonlinear Science* **2009,** 19, (4), 041110-1.

(13) Driscoll, M. K.; McCann, C.; Kopace, R.; Homan, T.; Fourkas, J. T.; Parent, C.; Losert, W., Cell Shape Dynamics: From Waves to Migration. *PLoS Computional Biology* **2012,** 8, (3), e1002392.

(14) Duxbury, D. F., The Photochemistry and Photophysics of Triphenylmethane Dyes in Solid and Liquid-Media. *Chemical Reviews* **1993,** 93, (1), 381-433.

(15) Engelhardt, S.; Hoch, E.; Borchers, K.; Meyer, W.; Kruger, H.; Tovar, G. E. M.; Gillner, A., Fabrication of 2D protein microstructures and 3D polymerâ€“protein hybrid microstructures by two-photon polymerization. *Biofabrication* **2011,** 3, (2), 025003.

(16) Farrer, R. A.; LaFratta, C. N.; Li, L.; Praino, J.; Naughton, M. J.; Saleh, B. E. A.; Teich, M. C.; Fourkas, J. T., Selective Functionalization of 3-D Polymer Microstructures. *Journal of the American Chemical Society* **2006,** 128, (6), 1796-1797.

(17) Fischer, A. R.; Werner, P.; Goss, K. U., Photodegradation of malachite green and malachite green carbinol under irradiation with different wavelength ranges. *Chemosphere* **2011,** 82, (2), 210-214.

(18) Fischer, J.; von Freymann, G.; Wegener, M., The Materials Challenge in Diffraction-Unlimited Direct-Laser-Writing Optical Lithography. *Advanced Materials* **2010,** 22, (32), 3578-3582.

(19) Formanek, F.; Takeyasu, N.; Tanaka, T.; Chiyoda, K.; Ishikawa, A.; Kawata, S., Selective electroless plating to fabricate complex three-dimensional metallic micro/nanostructures. *Applied Physics Letters* **2006,** 88, (8).

(20) Formanek, F.; Takeyasu, N.; Tanaka, T.; Chiyoda, K.; Ishikawa, A.; Kawata, S., Three-dimensional fabrication of metallic nanostructures over large areas by two-photon polymerization. *Optics Express* **2006,** 14, (2), 800-809.

(21) Fourkas, J. T., Nanoscale Photolithography with Visible Light. *Journal of Physical Chemistry Letters* **2010,** 1, (8), 1221-1227.

(22) Gessner, T.; Mayer, U., Triarylmethane and Diarylmethane Dyes. In *Ullmann's Encyclopedia of Industrial Chemistry*, Wiley-VCH Verlag GmbH & Co. KGaA: 2000.

(23) Göppert-Mayer, M., Über Elementarakte mit zwei Quantensprüngen. *Annalen der Physik* **1931,** 401, (3), 273-294.

(24) Gurr, E., *Synthetic Dyes in Biology, Medicine and Chemistry*. Academic Press Inc.: New York, 1971; p 807.

(25) Hell, S. W., Improvement of Lateral Resolution in Far-Field Fluorescence Light-Microscopy by Using 2-Photon Excitation with Offset Beams. *Optics Communications* **1994,** 106, (1-3), 19-24.

(26) Hell, S. W., Far-field optical nanoscopy. *Science* **2007,** 316, (5828), 1153-1158.

(27) Hell, S. W., Microscopy and its focal switch. *Nature Methods* **2009,** 6, (1), 24-32.

(28) Hell, S. W.; Wichmann, J., Breaking the Diffraction Resolution Limit by Stimulated-Emission - Stimulated-Emission-Depletion Fluorescence Microscopy. *Optics Letters* **1994,** 19, (11), 780-782.

(29) Hill, R. T.; Lyon, J. L.; Allen, R.; Stevenson, K. J.; Shear, J. B., Microfabrication of three-dimensional bioelectronic architectures. *Journal of the American Chemical Society* **2005,** 127, (30), 10707-10711.

(30) Hirschfelder, J. O.; Curtiss, C. F.; Bird, R. B.; University of Wisconsin. Theoretical Chemistry, L., *Molecular theory of gases and liquids*. Wiley: 1954.

(31) Kaiser, W.; Garrett, C. G. B., Two-Photon Excitation in CaF_2:Eu^{2+}. *Physical Review Letters* **1961,** 7, (6), 229-231.

(32) Klar, T. A.; Jakobs, S.; Dyba, M.; Egner, A.; Hell, S. W., Fluorescence microscopy with diffraction resolution barrier broken by stimulated emission. *Proceedings of the National Academy of Sciences of the United States of America* **2000,** 97, (15), 8206-8210.

(33) Kuebler, S. M.; Braun, K. L.; Zhou, W. H.; Cammack, J. K.; Yu, T. Y.; Ober, C. K.; Marder, S. R.; Perry, J. W., Design and application of high-sensitivity two-photon initiators for three-dimensional microfabrication. *Journal of Photochemistry and Photobiology A - Chemistry* **2003,** 158, (2-3), 163-170.

(34) Kumi, G.; Yanez, C. O.; Belfield, K. D.; Fourkas, J. T., High-speed multiphoton absorption polymerization: fabrication of microfluidic channels with arbitrary cross-sections and high aspect ratios. *Lab on a Chip* **2010,** 10, (8), 1057-1060.

(35) LaFratta, C. N. Multiphoton Absorption Polymerization: Issues and Solutions. Ph.D. Dissertation, University of Maryland, College Park, MD, 2006.

(36) LaFratta, C. N.; Fourkas, J. T.; Baldacchini, T.; Farrer, R. A., Multiphoton fabrication. *Angewandte Chemie-International Edition* **2007,** 46, (33), 6238-6258.

(37) LaFratta, C. N.; Li, L.; Fourkas, J. T., Soft-lithographic replication of 3D microstructures with closed loops. *Proceedings of the National Academy of Sciences of the United States of America* **2006,** 103, (23), 8589-8594.

(38) Ledermann, A.; Wegener, M.; von Freymann, G., Rhombicuboctahedral Three-Dimensional Photonic Quasicrystals. *Advanced Materials* **2010,** 22, (21), 2363-2366.

(39) Lee, J. N.; Park, C.; Whitesides, G. M., Solvent Compatibility of Poly(dimethylsiloxane)-Based Microfluidic Devices. *Analytical Chemistry* **2003,** 75, (23), 6544-6554.

(40) Li, L.; Driscoll, M.; Kumi, G.; Hernandez, R.; Gaskell, K. J.; Losert, W.; Fourkas, J. T., Binary and Gray-Scale Patterning of Chemical Functionality on Polymer Films. *Journal of the American Chemical Society* **2008,** 130, (41), 13512-13513.

(41) Li, L.; Gattass, R. R.; Gershgoren, E.; Hwang, H.; Fourkas, J. T., Achieving lambda/20 Resolution by One-Color Initiation and Deactivation of Polymerization. *Science* **2009,** 324, (5929), 910-913.

(42) Li, L.; Gershgoren, E.; Kumi, G.; Chen, W. Y.; Ho, P. T.; Herman, W. N.; Fourkas, J. T., High-Performance Microring Resonators Fabricated with Multiphoton Absorption Polymerization. *Advanced Materials* **2008,** 20, (19), 3668-3671.

(43) Li, Y.; Qi, F. J.; Yang, H. H.; Gong, Q. Z.; Dong, X. M.; Duan, X., Nonuniform shrinkage and stretching of polymerized nanostructures fabricated by two-photon photopolymerization. *Nanotechnology* **2008,** 19, (5).

(44) Lillie, R. D.; Conn, H. J.; Biological Stain, C., *H. J. Conn's Biological stains: a handbook on the nature and uses of the dyes employed in the biological laboratory*. 9 ed.; Williams & Wilkins: Baltimore, 1977; p 692.

(45) Maruo, S.; Fourkas, J. T., Recent progress in multiphoton microfabrication. *Laser & Photonics Reviews* **2008,** 2, (1-2), 100-111.

(46) Maruo, S.; Ikuta, K., Submicron stereolithography for the production of freely movable mechanisms by using single-photon polymerization. *Sensors and Actuators, A: Physical* **2002,** 100, (1), 70-76.

(47) Nielson, R.; Koehr, B.; Shear, J. B., Microreplication and Design of Biological Architectures Using Dynamic-Mask Multiphoton Lithography. *Small* **2009,** 5, (1), 120-125.

(48) Odian, G. G., *Principles of polymerization*. Wiley: 1991.

(49) Pitts, J. D.; Campagnola, P. J.; Epling, G. A.; Goodman, S. L., Submicron multiphoton free-form fabrication of proteins and polymers: Studies of reaction efficiencies and applications in sustained release. *Macromolecules* **2000,** 33, (5), 1514-1523.

(50) Pitts, J. D.; Howell, A. R.; Taboada, R.; Banerjee, I.; Wang, J.; Goodman, S. L.; Campagnola, P. J., New photoactivators for multiphoton excited three-dimensional submicron cross-linking of proteins: Bovine serum albumin and type 1 collagen. *Photochemistry and Photobiology* **2002,** 76, (2), 135-144.

(51) Reisfeld, R.; Chernyak, V.; Jorgensen, C. K., Photophysical Behavior of Malachite Green in Solid and Liquid-Media. *Chimia* **1992,** 46, (4), 148-151.

(52) Rosenthal, I.; Peretz, P.; Muszkat, K. A., Thermochromic and Hyperchromic Effects in Rhodamine-B Solutions. *Journal of Physical Chemistry* **1979,** 83, (3), 350-353.

(53) Scott, T. F.; Kowalski, B. A.; Sullivan, A. C.; Bowman, C. N.; McLeod, R. R., Two-Color Single-Photon Photoinitiation and Photoinhibition for Subdiffraction Photolithography. *Science* **2009,** 324, (5929), 913-917.

(54) Senturia, S. D., *Microsystem Design*. Kluwer Academic Publishers: 2001.

(55) Soukoulis, C. M.; Wegener, M., Past achievements and future challenges in the development of three-dimensional photonic metamaterials. *Nature Photonics* **2011,** 5, (9), 523-530.

(56) Stocker, M. P.; Fourkas, J. T., Elucidating the kinetics and mechanism of RAPID lithography. *Proceedings of SPIE* **2012,** 8249, 824902-1-7.

(57) Stocker, M. P.; Li, L. J.; Gattass, R. R.; Fourkas, J. T., Multiphoton photoresists giving nanoscale resolution that is inversely dependent on exposure time. *Nature Chemistry* **2011,** 3, (3), 223-227.

(58) Sun, H.-B.; Kawata, S., Two-Photon Photopolymerization and 3D Lithographic Microfabrication. *Advances in Polymer Science* **2004,** 170, 169-273.

(59) Thiel, M.; Decker, M.; Deubel, M.; Wegener, M.; Linden, S.; von Freymann, G., Polarization stop bands in chiral polymeric three-dimensional photonic crystals. *Advanced Materials* **2007,** 19, (2), 207-210.

(60) Turunen, S.; Kapyla, E.; Terzaki, K.; Viitanen, J.; Fotakis, C.; Kellomaki, M.; Farsari, M., Pico- and femtosecond laser-induced crosslinking of protein microstructures: evaluation of processability and bioactivity. *Biofabrication* **2011,** 3, (4).

(61) von Freymann, G.; Ledermann, A.; Thiel, M.; Staude, I.; Essig, S.; Busch, K.; Wegener, M., Three-Dimensional Nanostructures for Photonics. *Advanced Functional Materials* **2010,** 20, (7), 1038-1052.

(62) Weiß, T.; Hildebrand, G.; Schade, R.; Liefeith, K., Two-Photon polymerization for microfabrication of three-dimensional scaffolds for tissue engineering application. *Engineering in Life Sciences* **2009,** 9, (5), 384-390.

(63) Weiß, T.; Schade, R.; Laube, T.; Berg, A.; Hildebrand, G.; Wyrwa, R.; Schnabelrauch, M.; Liefeith, K., Two-Photon Polymerization of Biocompatible Photopolymers for Microstructured 3D Biointerfaces. *Advanced Engineering Materials* **2011,** 13, (9), B264-B273.

(64) Yang, D.; Jhaveri, S. J.; Ober, C. K., Three-dimensional microfabrication by two-photon lithography. *MRS Bulletin* **2005,** 30, (12), 976-982.

(65) Zhou, W. H.; Kuebler, S. M.; Braun, K. L.; Yu, T. Y.; Cammack, J. K.; Ober, C. K.; Perry, J. W.; Marder, S. R., An efficient two-photon-generated photoacid applied to positive-tone 3D microfabrication. *Science* **2002,** 296, (5570), 1106-1109.